UiT
THE ARCTIC
UNIVERSITY
OF NORWAY

Department of Physics and Technology

Snow Stratigraphy Measurements With UWB Radar

—

Rolf Ole Rydeng Jenssen

FYS-3941 Master's Thesis in Applied Physics and Mathematics
December 2016

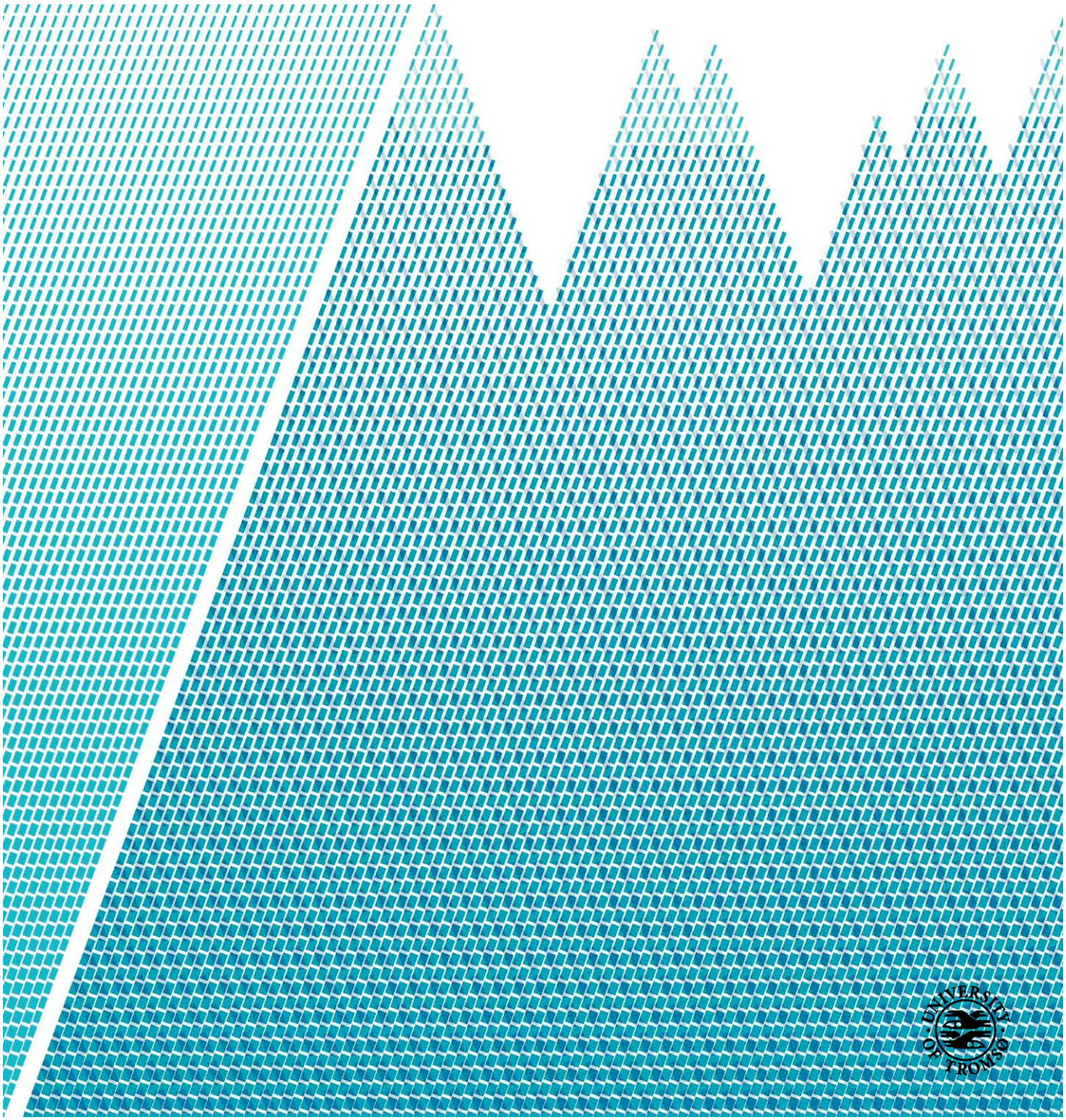

"...by their [standing electromagnetic short waves] use we may produce at will, from a sending station, an electrical effect in any particular region of the globe; [with which] we may determine the relative position or course of a moving object, such as a vessel at sea, the distance traversed by the same, or its speed."

- Nikola Tesla, in The Electrical Experimenter 5.4 (1917).
Commonly known as the first idea of radar.

Abstract

The focus of this thesis is to find and verify a non-invasive method to determine the layer distribution (stratigraphy) in snowpacks, which might aid avalanche risk assessment. Slab avalanches release due to failure and collapse in a weak snow layer. Determining the spatial distribution and depth of weak layers in avalanche starting zones is a high-risk task. Moreover, by manually digging snow pits, the occurrence of a weak layer can only be identified on a pit scale. We, therefore, propose a technical solution to this problem by mounting an ultra wideband radar system onto an unmanned aerial vehicle to obtain information about weak layers over a larger area and improve safety for avalanche professionals. During 2016, we have operated the radar system via a stationary platform 1 m above the snow, along 4.2 m long transects. For verification, we dug a full snowpit and used snow measurement probes (Avatech SP2 and Toikka SnowFork) to measure snow depth, liquid water content and density, as well as snow stratigraphy. Results show an average correlation between radar and *in situ* measurements of 0.97 and RMS error of 2.48 cm when extracting the most prominent transitions in the snow. The method developed in this thesis is tested on different types of snow. Additionally, the radar system is tested as payload on an unmanned aerial vehicle. Future work includes further development of the radar system and airborne measurements on snowpacks.

Acknowledgements

First and foremost, I would like to thank my supervisor, professor Svein Jacobsen. Your lectures in microwave engineering introduced me to a new realm in electronics that inspired me to pursue a sensor technology specialization. Your work on the UWiBaSS system is what made this project possible, and our interesting discussions throughout the work on this thesis have been very helpful.

To the Remote Sensing, Satellites and UAS group at Norut; thank you for helping me with the *in situ* measurements, octocopter flight testing and for the help with writing my first conference proceeding.

To The Norwegian Polar Institute; thank you for letting me borrow your snow fork sensor, which was a vital contribution to the *in situ* measurements.

To the mechanical shop at UiT; thank you for letting me borrow tools and other equipment to build the radar platform.

To my fellow students, office mates and cheese connoisseurs Thomas Johansen, Sara Björk and Torgeir Brenn; you made this final semester a lot less stressful than expected.

To my friends, family and especially Ina Lundberg; thank you for your support and patience during my work on this thesis.

Contents

List of Figures

List of Tables

Abbreviations

ADC analog-to-digital converter

CDF cumulative distribution function

CTBV continuous time binary valued

FFT fast Fourier transform

FMCW frequency modulated continuous wave

FWHM full width at half maximum

GPR ground penetrating radar

GPS global positioning system

HPBW half power beam width

IEEE Institute of Electrical and Electronics Engineers

MLBS maximum length binary sequence

PRBS pseudo random binary sequence

PDF probability density function

PEC perfect electrical conductor

PRF pulse repetition frequency

PRN pseudo random noise

RF radio frequency

RX receiving

SAR synthetic aperture radar

SCR signal to clutter ratio

SFCW stepped frequency continuous wave

SNR signal to noise ratio

SVD singular value decomposition

SWE snow water equivalent

T&H track & hold

TX transmitting

UAV unmanned aerial vehicle

UWB ultra wide band

UWiBaSS ultra wide band snow sensor

VCO voltage controlled oscillator

VSWR voltage standing wave ratio

Selected Symbols

The following list contains a selection of the most central constants and symbols used in this thesis.

Constants

ϵ_0	Absolute permittivity of free space (vacuum)	8.85×10^{-12} Fm^{-1}
μ_0	Absolute permeability of free space (vacuum)	$4\pi \times 10^{-7}$ Hm^{-1}
c	speed of light in vacuum	$299,792,458$ ms^{-1}

Symbols

ϵ	Absolute permittivity of medium	Fm^{-1}
ϵ_r	Relative permittivity of medium	
ϵ_r''	Imaginary part of relative permittivity	
ϵ_r'	Real part of relative permittivity	
λ	Wavelength	m
$\mathbf{E}$	Instantaneous electric field component of EM wave	Vm^{-1}
μ	Absolute magnetic permeability of medium	Hm^{-1}
μ_r	Relative permeability of medium	
ω	Angular frequency	rad/s
ρ_d	Density	g/cm^3
$\tan\delta$	Material loss tangent	
f	Frequency	Hz
j	Imaginary unit	$\sqrt{-1}$

Syntax

$*$	Convolution
$\mathbf{A}$	Matrix (bold upper-case)
$\mathbf{a}$	Vector (bold lower-case)

Chapter 1

Introduction

1.1 Avalanche Risk Assessment

Snow slab avalanches are responsible for approximately 90 % of avalanche-related fatalities [1], and typically involves dry snow slabs triggered by people [2]. Therefore, an improved method to determine the level of threat with this snow type is desired. Currently, avalanche professionals make mechanical measurements by manually digging snow pits and assess the layer distribution by hand hardness tests [3]. Manual measurements in avalanche starting zones can be dangerous and might cause deviations between each trained professional. Scientific methods exist where avalanche professionals make mechanical measurements at many different length scales, from micrometer scales [4] to studies on entire avalanche slopes [5], [6].

Most weak layers develop at the snow surface and get subsequently buried [7]. Different weather conditions during layer development result in a diverse set of densities and hardness through the snowpack. Buried porous layers can collapse and allow the layers above to slide, and thin layers can be hard to detect with hand hardness tests [4]. Normally the avalanche risk is determined to be on a scale of 1 to 4 where 1 is "low risk" and 4 is "very high risk" [8, 9]. Additionally, the destructive capabilities of an avalanche are determined on a scale from 1 to 5 [10].

1.2 UWB radar

The idea of radar is often considered introduced by Nikola Tesla in 1917. However, the first experiments with traveling electromagnetic waves and their reflection were already conducted in the late 19th century by Heinrich Hertz (1893) [11], showing that transverse free space electromagnetic waves (TEM waves) can travel over some distance as predicted by James Maxwell

and Michael Faraday [12]. In the first radar systems, targets were detected by transmitting a pulse of electromagnetic energy into the atmosphere and receiving the reflected signals. To achieve higher resolution, radars were designed to transmit shorter pulses, thus making the transmitted spectrum broader. Transmitting short pulses implies high energy peaks over a short time. Later on, radar waveforms were designed to be longer in time and have a spread out frequency bandwidth as a function of time, thus enabling both high range resolution without high energy peaks. If the bandwidth is large compared to the center frequency of the transmitted signal, it is called an Ultra Wide Band (UWB) signal [13]. The Federal Communications Commission (FCC) currently define UWB as an antenna transmission for which the emitted signal bandwidth exceeds 500 MHz or is greater than 20% of the transmitted signal center frequency. In recent years, the use of UWB signals in radar has increased after the FCC allocated part of the spectrum below 10 GHz for unlicensed use.

1.3 Aim of Study

The aim of this thesis is to find and verify a non-invasive method to determine the layer distribution (stratigraphy) in snow, which might aid the prediction of avalanche risk.

The key solution proposed in this thesis is to utilize ultra wide band (UWB) radar systems to measure snow stratigraphy that can be later analyzed by avalanche professionals. To verify the ability to find snow stratigraphy with UWB radar systems, a measurement platform was constructed to facilitate for stable above ground measurements.

The radar proposed in this report can be mounted under an unmanned aerial vehicle (UAV) to enable autonomous scanning of large areas. This will also yield a considerably better resolution of avalanche risk mapping, and might "steer" skiers to safer regions of the mountain. There are several other applications for non-invasive snow measurements. For instance, it might be used to predict water resources stored in snow covered mountains [14], or aid in the search for buried people [15].

All radar measurements are correlated against *in situ* measurements with several traditional measurement tools and high-performance scientific instruments. An important aspect of this thesis is to use "traditional" methods of snow pit characterization and compare these to the radar measurements to see if it is possible to determine and identify the same snow stratigraphy. Dielectric and mechanical properties in snow are related in an unknown and complicated way [16]. However, Geldsetzer and Jamieson [17] did show that

there is a relationship between snow density and crystal hardness, which in turn is related to the dielectric and mechanical properties respectively. Thus, we might be able to distinguish the same structures with the UWB radar as with *in situ* measurements.

1.4 Related Work

The scientific study of snow stratigraphy began in the 18th century, however, tools to perform quick and objective measurements have not been available until recent years. In Pielmeier and Schneebeli [18], a review of the development of snow stratigraphy research is conducted. Here, they point out that the recent advances in stratigraphy measurements provide evidence that challenges the traditional assumption of a snowpack consisting of discrete, homogeneous layers.

Many previous studies have shown correlations between snowpit and radar measurements. However, in comparison with other media, little work has been done on UWB radar stratigraphy measurements on snow. Early work by Gubler and Hiller [19] and Holmgren et al. [20] show that surface and ground layers are easily detected. Ellerbrugh and Boyne [21] investigated the amplitude of the scattered radiation as a function of depth in the snow-pack and if it can be correlated with such physical characteristics as density, hardness, stratigraphy, and moisture content to estimate snow water equivalent (SWE) of the snowpack. Previous studies using impulse radar ([22, 23]) show that this method is sensitive to the layering in the snow and that the snow water equivalent could, to some degree, be estimated. Several studies using frequency modulated continuous wave (FMCW) radar ([16, 24, 25, 26]) show that the most prominent structures in the snowpack are also detectable with radar using ground based measurement platforms. In Marshall, Schneebeli, and Koh [16] a correlation between measured transition depths with radar and *in situ* instruments was found to be 0.92 with RMS error of 1.6 cm. A gated stepped frequency continuous wave (SFCW) radar is presented in Øyan et al. [27] and is tested on glacial ice and permafrost in Svalbard. In Yankielun, Rosenthal, and Davis [14], Gogineni et al. [28], Kwok et al. [29] and Panzer et al. [30] FMCW radars are used to measure snow and ice thickness from aircraft. The effects of snowpack parameters at X- and KU- band are described in Arslan et al. [31] where a correlation between SWE and back-scattering coefficients were investigated. In Eder et al. [32] and Singh et al. [33] ground penetrating radar (GPR) is used for crevasse detection below snow and snow depth measurements. In Azadegan et al. [34] an analytical formulation for the scattering of a rough dielectric

boundary (e.g. ground layer) is presented.

The preliminary results from this thesis have been presented in a conference proceeding for the International Snow Science Workshop in Breckenridge, Colorado. In this proceeding, Jenssen et al. [35] briefly presented the measurement method and preliminary results.

1.5 Structure of Thesis

This thesis is divided into four parts:

Part 1 contains the background theory needed for the methods used in this thesis. Chapter 2 presents fundamental antenna theory. The basic equations presented here form the basis for the theory and considerations to come. Chapter 3 presents UWB radar theory, where combined with chapter 2, the central theorems used when designing and operating radar systems are presented. Chapter 4 presents methods to improve radar responses where the methods are divided into two types: A-scan and B-scan processing. Here we look at data representation, deconvolution, edge detection, migration, adaptive filtering and much more. Some parts of the presented theory are especially important regarding snow measurements. Therefore, some sections will have short case studies where we look at how the previously presented theory works in snow.

In **part 2**, we present the radar systems and *in situ* measurement tools. In chapter 5 we go through the two radar systems used during the measurement campaign and discuss advantages and disadvantages with both the radar sensors and antennas. Additionally, we will take a look at the physical layout of the measurement scenario and how the measurement platform was constructed. Chapter 6 presents several methods to measure different snow-parameters and some instruments are compared to explain why certain *in situ* tools were chosen.

In **part 3**, the results from the measurement campaign are presented. Chapter 7 and Chapter 8 use a selected measurement as a case study to show the effects of each processing step through A-scan and B-scan processing respectively. Chapter 9 present the correlation between the radar measurements and the *in situ* measurements. Chapter 10 present additional results from testing the radar systems on different snow types and a UAV flight test, as well as a comparative study of two different radar systems.

In **part 4** we draw conclusions based on the results and discuss possible improvements to both hardware and software. Suggestions to future work are also presented along with already planned measurement campaigns.

Part I

Background Theory

Chapter 2

Antenna Theory

The central theory in this thesis is based on the propagation of electromagnetic waves in a medium and their reflection [11]. Arguably, the most important part of any radar system is the antenna. The Institute of Electrical and Electronics Engineers (IEEE) definition for antennas defines the antenna as: "That part of a transmitting or receiving system which is designed to radiate or to receive electromagnetic waves." [36]. Such a medium is a central part of any radar system. In other words, the role of the radar antenna is to couple the free-space and guided-wave propagation of electromagnetic waves.

A directional antenna concentrates the radiated energy into a shaped directive beam that illuminates the target in the desired direction. The reflecting energy is then collected by the receiving antenna, which could be the same antenna, and sent to the radar receiving system. A typical UWB system utilizes two antennas; one for transmitting and one for receiving. This is due to the simplicity of implementing two antenna ports instead of using a directive coupling on a single port. The reciprocal behavior of antennas means that these two antennas are best matched when they are identical. Some of the most applied parameters to characterize antennas are; Gain, Directivity, Half Power Beam Width (HPBW) and Voltage Standing Wave Ratio (VSWR) (see below for definitions).

2.1 Radiation Pattern

The radiation pattern is the spatial distribution that characterizes the electromagnetic field generated by the antenna. Normally, it is a plot of the amplitude or power pattern of the antenna.

In Figure 2.1 we can see the horizontal radiation pattern of a general directional antenna. This particular antenna is to some degree bidirectional as it has a significant lobe 180° from the main lobe. An omnidirectional

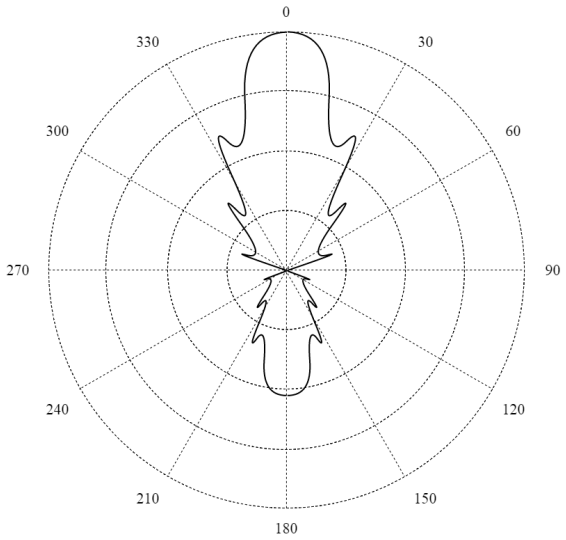

Figure 2.1: Example horizontal radiation pattern vs angle of a directional antenna.

antenna has about the same amplitude in all directions in at least one plane.

Assuming the antenna is stationary or is moving relatively slowly compared to the acquisition time of the radar system, we can imagine at each sampled data point a collection of several returning pulses from different objects. These reflected pulses become part of a weighted sum where each returning pulse receive a weight based on their direction of arrival. This is inherent in a radar system and is caused by the antenna radiation pattern.

2.2 Directivity

Directivity is defined as: "The ratio of the radiation intensity in a given direction from the antenna to the radiation intensity averaged over all directions. The average radiation intensity is equal to the total power radiated by the antenna divided by 4π. If the direction is not specified, the direction of maximum radiation intensity is implied." [36]. Directivity is a measure of how 'directional' an antennas radiation pattern is. Directivity is a function of angle, commonly expressed as:

$$D(\theta, \phi) = \frac{4\pi U(\theta, \phi)}{P_{rad}} \quad [\text{dBi}] \ , \tag{2.1}$$

where $U(\theta, \phi)$ is the radiation intensity, which is the power density per unit solid angle and P_{rad} is the total radiated power. Antenna gain and directivity

are in reference to the radiation intensity of an isotropic source [36]. Hence, it is on the unit form dBi (i stands for isotropic). Directivity is a function of angle, but normally when a directivity is specified for an antenna it is the peak directivity that is given.

2.3 Efficiency

The efficiency of an antenna is a ratio of the power delivered to the antenna (P_{IN}) relative to the power radiated from the antenna (P_{rad}). That is, a high-efficiency antenna radiates most of the power present at the antenna input terminals. If most of the power is absorbed within the antenna it is considered a low-efficiency antenna. Being a ratio, antenna efficiency is a number between 0 and 1, often quoted in terms of percentage (e.g. 0.5 is 50 %):

$$e = \frac{P_{rad}}{P_{IN}} \ . \tag{2.2}$$

This measure takes into account reflection, conduction and dielectric efficiency of the antenna. These terms are difficult to measure individually, though numerical computation can be used to identify the different loss factors. If the reflection coefficient Γ is known the reflection efficiency e_r can be calculated as:

$$e_r = (1 - |\Gamma|^2) \ , \tag{2.3}$$

which is related to return loss (see VSVR).

2.4 Absolute Gain

The ability of an antenna to concentrate energy in a narrow angular region (a directive beam) is described in terms of antenna gain [36]. Antenna gain is described as a ratio of the radiation intensity in a given direction, related to the total input power radiated by an isotropic antenna.

$$G = 4\pi \frac{U(\theta, \phi)}{P_{IN}} \quad [\text{dBi}] \ . \tag{2.4}$$

Absolute gain is more commonly quoted than directivity because it takes into account the efficiency of the antenna.

Antenna Gain can be related to directivity and antenna efficiency by:

$$G = eD \ . \tag{2.5}$$

Partial gain is defined as the absolute gain related to a given polarization [36].

2.5 Voltage Standing Wave Ratio (VSWR)

Since measures such as directivity do not account for any dissipative losses in the antenna, voltage standing wave ratio (VSWR) is also needed to best characterize antennas. VSWR is in direct relation to the performance of the antenna as it is a measure of how well matched the antenna is to the transmission line or transceiver system. Power reflected by an antenna on a transmission line interferes with the forward traveling power, and this creates a standing voltage wave. The ratio between the maximum and minimum standing wave is the VSWR. Which in return depends on the reflection coefficient Γ at the input terminals of the antenna [37].

$$VSWR = \frac{V_{max}}{V_{min}} = \frac{1 + |\Gamma|}{1 - |\Gamma|} \ . \tag{2.6}$$

The reflection coefficient is defined as [37]:

$$\Gamma = \frac{Z_{in} - Z_0}{Z_{in} + Z_0} \ , \tag{2.7}$$

where Z_0 is the characteristic impedance of transmission line and Z_{in} is the input impedance of the antenna. This impedance is not frequency independent and will change over a band of frequencies, which is important to take into account when working with UWB systems as antenna design considerations can alter the rate of change in impedance through frequency bands.

In other words, VSWR describes the impedance matching of a radar system. Bandwidth is described as: "The range of frequencies within which the performance of the antenna, with respect to some characteristic, conforms to a specified standard." [36]. The impedance matching over frequencies and therefore VSWR is closely related to bandwidth.

VSWR can also be related to antenna mismatch loss (return loss) by:

$$L_m = -20 \log |\Gamma| \ . \tag{2.8}$$

This will be used later when all losses related to the radar system are calculated.

2.6 Half Power Beamwidth

The half power beam width (HPBW) is defined by the IEEE as: "In a plane containing the direction of the maximum of a beam, the angle between the two directions in which the radiation intensity is one-half value of the beam" [36]. The half power beamwidth is a description of the width of the main beam of the antenna radiation pattern. In other words, the angular separation in which the maximum magnitude of the power radiation pattern decrease by 50% (-3 dB).

This is an adequate measure to distinguish different types of antennas in terms of directivity. Since HPBW is an indicator of the directivity of the antenna, it is also a measure of the transversal resolution of the antenna system.

2.7 Polarization

Polarization is defined by IEEE as: "In a specified direction from an antenna and at a point in its far field, the polarization of the (locally) plane wave which is used to represent the radiated wave at that point." [36]. The electric field is perpendicular to the direction of propagation, and it is the direction of this electric field that is the polarization of the electromagnetic wave. The polarization is the figure that the electric field traces out while propagating.

Chapter 3

Ultra Wideband Radar Theory

Ultra Wideband Radar systems have high range resolution due to the large bandwidth in use. Nonetheless, many of the same principals from conventional radar theory also apply for UWB radar systems. In this chapter, we will take a look at the most central principals for radar systems that send signals into different media. Most of the subjects presented are collected from GPR theory, as many of the same principals apply for ground and snow penetration.

3.1 The Radar Equation

The radar equation is the most fundamental equation describing radar systems. The received power is defined as [13]:

$$P_r = \frac{P_t G_t A_r \sigma F^4}{(4\pi)^2 R_t^2 R_r^2} \ , \tag{3.1}$$

where each parameter is defined in table 3.1. In the most common case, where the transmitting and receiving antenna is in the same position; $R_t = R_r = R$ and we get:

$$P_r = \frac{P_t G_t A_r \sigma F^4}{(4\pi)^2 R^4} \ . \tag{3.2}$$

If we have the same gain for the receiving and transmitting antenna ($G_t = G_r = G$) and use that $A_r = \frac{G_r \lambda^2}{4\pi}$, we get:

$$P_r = \frac{P_t G^2 \lambda^2 \sigma F^4}{(4\pi)^3 R^4} \ . \tag{3.3}$$

It is common to express the radar equation in terms of range, which reformulates the radar equation to:

$$R = \sqrt[4]{\frac{P_t G^2 \lambda^2 \sigma F^4}{(4\pi)^3 P_r}} \ . \tag{3.4}$$

The pattern propagation factor F includes several losses that influence the system considerably. This includes:

- Internal attenuation factors of the radar system on the transmitting and receiving paths.
- Fluctuation losses during reflection from the target.
- Atmospheric losses during propagation of the electromagnetic waves to and from the target. Different loss factors for multiple-medium paths must also be considered.

Path loss is described in more detail in section 3.4.

Table 3.1: Radar equation designators

Designator	**Description**
P_r	Received Power
P_t	Transmitted Power
G_t	Gain of transmitting antenna
$A_r = \frac{G_r \lambda^2}{4\pi}$	Effective aperture of receiving antenna
G_r and λ	Gain of receiving antenna and transmitted wavelength
σ	Radar cross section, or scattering coefficient, of the target
F	Pattern propagation factor (total loss factor)
R_t	Distance from the transmitter to the target (range)
R_r	Distance from the target to the receiver (range)

An important effect of these equations is the relationship between the received power and the range. The received power decreases as the fourth power of the range, which means that increasingly distant targets become significantly harder to detect. This effect is known as spreading loss (L_s) and is defined as [38]:

$$L_s = -10 \log_{10} \frac{G^2 \lambda^2 \sigma}{(4\pi)^3 R^4} \ . \tag{3.5}$$

The maximum measuring distance of a radar is not orientated only at the value determined by the radar equation, but also on the duration of the receiving time. We cannot send out another pulse until a time window has passed, in which we expect to see a return pulse. This property is called unambiguity range and is defined in section 5.2 for m:sequence radar systems and in section 5.4 for pulse radar systems.

3.2 Velocity of Propagation

If the propagation velocity of a wave through a medium can be measured, or derived, then absolute measurement of depth or thickness of the medium can be made. For homogeneous and isotropic materials, the relative propagation velocity v_p can be calculated by [38]:

$$v_p = \frac{c}{\sqrt{\epsilon_r}} \quad [\mathrm{ms}^{-1}] \ , \tag{3.6}$$

and the distance to a given target (often denoted as depth) becomes:

$$d = v_p \frac{t}{2} \quad [\mathrm{m}] \ , \tag{3.7}$$

where ϵ_r is the relative permittivity of the medium, c is the speed of light in vacuum and t is the two-way travel time from the radar to the target. In most practical trial situations the relative permittivity will be unknown and must be measured *in situ*.

As shown in Daniels [38], the velocity of propagation is also slowed by an increase of loss tangent $\tan\delta$, as well as relative permittivity. However, $\tan\delta$ must be significantly greater than 1 for any significant slowing to occur. In the case of snow, $\tan\delta$ is in the range $0.2 \cdot 10^{-4} - 0.5 \cdot 10^{-4}$ and can therefore, be ignored.

3.3 Monostatic and Bistatic Antenna Configuration

Monostatic and Bistatic is a way of describing radar antenna configuration and also defines how transmission can be performed. In the case of monostatic operation, the transmitting and receiving antenna are the same. This implies that transmission and receiving have to be performed in separate cycles. The bistatic configuration uses a separate transmitting and receiving antenna which in turn gives the possibility to transmit and receive at the same time. Additionally, the spacing and relative angles of the receiving and transmitting antenna can be configured in many different ways depending on the measurement scenario. Due to the reciprocal behavior of antennas, the best match for transmitting and receiving antennas is when they are identical.

3.4 Limiting Factors for the Radar Response

Noise

Noise, in this case, is referred to random variations from the components that form the radar transmitter, receiver, and antenna. Noise will create unwanted disturbance in the received signal and adequate measures must be taken to reduce noise in the design of systems as well as filtering during the processing of received signals. The radiated signal amplitude decreases rapidly during propagation (see equation (3.3)), and subsequently noise from internal components contributes to the reduction of radar range.

Crosstalk

Crosstalk is caused by an undesired capacitive coupling or even propagation at a larger distance between the transmitting and receiving antenna. This implies that some of the transmitted pulse is collected by the receiving antenna directly from the source. This unwanted effect can to a high degree be canceled by subtracting a free space reference from the radar response data. See section 4.2 for a detailed description of crosstalk removal.

Doppler Effect

If there is motion in either the target or the radar a frequency shift can be introduced due to the change in wavelengths between the target and the radar. This can be desirable if the system is to detect velocity or moving objects, but in a system that is to obtain high-resolution information from a stationary target, this can be problematic if the radar is moving. However, this will not create any significant problems if the radar is moving relatively slow compared to the transmitted frequency.

The difference in frequency between the transmitted (f_t) and received (f_r) signal is called the Doppler frequency $f_d = f_t - f_r$ [39]. If the velocity of the radar (or object) v is much less than the pulse velocity of the radio wave, which is often close to the vacuum speed of light c ($v \ll c$), the following expression can be written for the Doppler frequency:

$$f_d \approx 2v\frac{f_t}{c}\cos\alpha \ , \tag{3.8}$$

where α is the angle between the propagating wave and the target. The maximum Doppler frequency is reached when $\alpha = 0$. In radar scanning situations (B-scan, presented in section 4.1), maximum Doppler would represent the periphery of radar aperture.

Equation (3.8) shows that the velocity of the radar (or object) must decrease if the transmitted frequency increase, to avoid unwanted Doppler effects.

Case Study: Doppler Effects

We can consider the antenna with the largest HPBW used in this thesis to rule out Doppler effects. The Archimedean spiral antenna have an HPBW of 70°. If we consider the HPBW as the angle of maximum Doppler, note that the radar moved at approximately 0.01 m/s and choose the highest frequency from the radar bandwidth we get:

$$f_d \approx 2(0.01 \text{ m/s})\frac{6 \text{ GHz}}{c}\cos(90° - 70°) \approx 0.37 \text{ Hz} . \tag{3.9}$$

From this result, we can conclude that the Doppler effect will have no significant contribution on the measurements when considering that within the bandwidth of 5.05 GHz we will get a Doppler frequency ranging from 0.056 Hz to 0.37 Hz.

Clutter

There might be objects close to the target that is not of interest to the radar operator. Still, these objects will give a response collected by the receiving antenna. If the target is non-stationary and the clutter is stationary (or 'Vice Versa') this can be reduced with Doppler processing. Additionally, there might be objects between the target and the antenna, or close to the path of radiation that might cause unwanted clutter in the radar image. Some objects cause ringing resonance effects when detected. This can be utilized to remove all contributions responsible for the ringing effect.

Interference

In a UWB radar system, a very broad range of frequency components are collected by the receiving antenna. These might include other competing signals than what are radiated by the transmitter. Wireless communication, global positioning system (GPS) signals and atmospheric noise all contribute to the interference of the system. In addition, we have internal interference generated within the receiver and clutter from non-interesting objects (described above). The ability of the radar system to overcome these unwanted signals defines its signal to clutter ratio (SCR).

Path Loss

Snow stratigraphy imaging requires a wave penetrating the snow surface and the internal layers of the snow until reaching the ground and returning back through the layers. The transmitted signal is attenuated in all media depending on the permittivity as well as the scattering in the air-snow interface and between interfaces in the snow.

The detected signal undergoes several losses in its propagation path from the transmitter to the receiver. The total propagation loss for a particular distance can be written as [38]:

$$L_T = L_e + L_m + L_{t1} + L_{t2} + L_s + L_a + L_{sc} \ , \tag{3.10}$$

where each loss is described in table 3.2:

Table 3.2: Path loss equation designators

Designator	**Description. All designators are in dB**
L_e	Antenna efficiency loss
L_m	Antenna mismatch loss (return loss)
L_{t1}	Transmission loss from air to material
L_{t2}	Retransmission loss from material to air
L_s	Antenna spreading losses
L_a	Attenuation loss in material
L_{sc}	Target scattering loss

Antenna efficiency and mismatch loss are described in the antenna theory section. In [38] it is shown that the transmission loss and retransmission loss is effectively the same. The antenna spreading loss is related to the inverse fourth power of the distance to a point reflector; previously defined in equation (3.5) as:

$$L_s = -10 \log_{10} \frac{G^2 \lambda^2 \sigma}{(4\pi)^3 R^4} \ . \tag{3.11}$$

The loss due to the reflection at the air-snow interface can be regarded as equal for transmission and retransmission ($L_{t1} = L_{t2}$) and depends on the angle of the electric field relative to the incident plane. If the electric field is parallel to the incident plane (i.e. the snow) the loss can be calculated as [40]:

$$L_{t1} = 20 \log_{10} \left(\frac{2\sqrt{\epsilon_r - sin^2\theta_i}}{\epsilon_r \cos\theta_i + \sqrt{\epsilon_r - sin^2\theta_i}} \right) \ , \tag{3.12}$$

where θ_i is the incident angle and ϵ_r is the relative permittivity of the snow. In Daniels [38] the transmission loss is defined in terms of impedance. Additionally, any dielectric boundary (e.g. internal snow layers) can be described in terms of reflectivity R [26]:

$$R = \left(\frac{\sqrt{\epsilon_{r1}^{'}} - \sqrt{\epsilon_{r2}^{'}}}{\sqrt{\epsilon_{r1}^{'}} + \sqrt{\epsilon_{r2}^{'}}} \right)^2 , \tag{3.13}$$

where $\epsilon_{r1}^{'}$ and $\epsilon_{r2}^{'}$ are the real components of the relative permittivity of the medium at each side of a layer boundary.

The attenuation loss (L_a) inside each (relatively homogeneous) layer of snow is related to the thickness of the layer h and the attenuation constant α.

$$L_a = 20 \log_{10}(\exp(-\alpha h)) , \tag{3.14}$$

where the attenuation constant α is given by [38]:

$$\alpha = \omega \sqrt{\frac{\mu \epsilon^{'}}{2} \left(\sqrt{1 + \tan^2 \delta} - 1 \right)} , \tag{3.15}$$

with the magnetic permeability $\mu = \mu_0 \mu_r$ and the real part of the permittivity $\epsilon^{'} = \epsilon_0 \epsilon_r^{'}$ is defined based on its relative value and the free space value.

Since $c = \frac{1}{\sqrt{\mu_0 \epsilon_0}}$ equation (3.15) can be rewritten as:

$$\alpha = \frac{\omega}{c} \sqrt{\mu_r \epsilon_r^{'}} \sqrt{\frac{1}{2} \left(\sqrt{1 + \tan^2 \delta} - 1 \right)} , \tag{3.16}$$

where ω is the angular frequency. The relative permeability μ_r is 1 for non-magnetic materials [38], hence it is often not taken in to account in the expression. The loss tangent of the medium, $\tan \delta$ is given by [38]:

$$\tan \delta = \frac{\sigma}{\omega \epsilon} , \tag{3.17}$$

where σ is the conductivity and ϵ is the absolute permittivity of the medium (i.e. snow or any dielectric material).

From equation (3.16) we can see that the loss in the snow depends on the permittivity, the loss tangent, and the frequency. In practice, this means that some frequencies will not be able to penetrate a certain medium. This can be exploited in many ways. For instance, radar systems supposed to detect objects under clothes use a frequency that penetrates the clothing but not the human body [40]. An UWB radar system, therefore, has different attenuation constants across its bandwidth and only part of the bandwidth will penetrate a given medium.

The target scattering loss is given by [38]:

$$L_{sc} = 20 \log \left(1 - \frac{Z_1 - Z_2}{Z_1 + Z_2} \right) + 20 \log \sigma \ , \tag{3.18}$$

where σ is the radar cross section for a given target. Z_1 and Z_2 are the characteristic impedances of the two materials in the interface. In the case of snow, a radar cross section is hard to quantify as the target is a relatively large plane. We will instead consider a spherical target to give some impression of the losses related to scattering.

$$\sigma = \pi a^2 \ , \tag{3.19}$$

where a is the radius of the sphere target. In our example, the radius is set to $a = 0.5$ m. The characteristic impedance of snow is found in section 3.4.1.

3.4.1 Case Study: Loss Factors in Snow

Snow can be regarded as a complex material when it comes to electrical characterization. To estimate snow-parameters, we need to use models which are made based on physical experiments. The characteristic impedance of a material can be expressed as [38]:

$$Z_m = \left(\sqrt{\frac{\mu_0 \mu_r}{\epsilon_0 \epsilon_r}} \right) \frac{1}{(1 + \tan^2 \delta)^{\frac{1}{4}}} \left(\cos \frac{\delta}{2} + j \sin \frac{\delta}{2} \right) \ . \tag{3.20}$$

The loss tangent $\tan \delta$ for snow can be modeled as [41]:

$$\tan \delta = 1.59 \cdot 10^6 \left(\frac{0.52 \rho_d + 0.62 \rho_d^2}{1 + 1.7 \rho_d + 0.7 \rho_d^2} \right) (f^{-1} + 1.23 \sqrt{f} \cdot 10^{-14}) e^{0.036T} \ , \tag{3.21}$$

where ρ_d is the density of dry snow, f is the frequency and T is the temperature in degrees Celsius (i.e. in Kelvin: $\mathrm{C} = \mathrm{K} - 273.15$). The *in situ* density measurements of snow have been measured throughout the snowpack. For this calculation we use the average measured density of the dry snowpack from 11.03.16 ($\rho_d = 0.256$ g/cm^3). This yields a characteristic impedance of $Z_m = 319.3\ \Omega$ which is close to the impedance of air $Z_a = 377\ \Omega$.

We can now perform calculations regarding the losses in the radar system. The return loss and efficiency loss are only approximates taken from Daniels [38]. To find the spreading loss a gain figure was also collected from Wahab, Saputera, and Wahyu [42]. Additionally, to estimate the radar cross section; a spherical target with radius 0.5 m was used. The attenuation loss was found

Table 3.3: Loss summary for 1 GHz

Loss Type	Value
L_e	-4 dB
L_m	-1.5 dB
L_{t1}	-0.76 dB
L_{t2}	-0.76 dB
L_s	-32.3 dB
L_a	-1.38 dB
L_{sc}	-2.84 dB
Total loss	-43.54 dB

assuming a homogeneous snowpack of 1 m, and the attenuation constant was found through measurements with the Snow Fork [43].

In table 3.3 it is evident that the largest contributor to the loss in this measurement scenario is the spreading loss. This is due to the inherent properties of propagating waves explained in the radar equation (see section 3.1).

Penetration Depth in Snow

Now after investigating the loss factors in snow, we can consider what penetration depths we can achieve with microwaves. In Stiles and Ulaby [44] and Mätzler et al. [45] the penetration depth for dry and wet snow is computed. Figure 3.1 show the penetration depth for dry and wet snow according to the microwave emission model for layered snowpacks (MEMLS) [45].

Figure 3.1 shows that liquid water content in snow significantly reduces penetration depth. This will also become apparent in section 10.5 where we look at radar scans of wet snow.

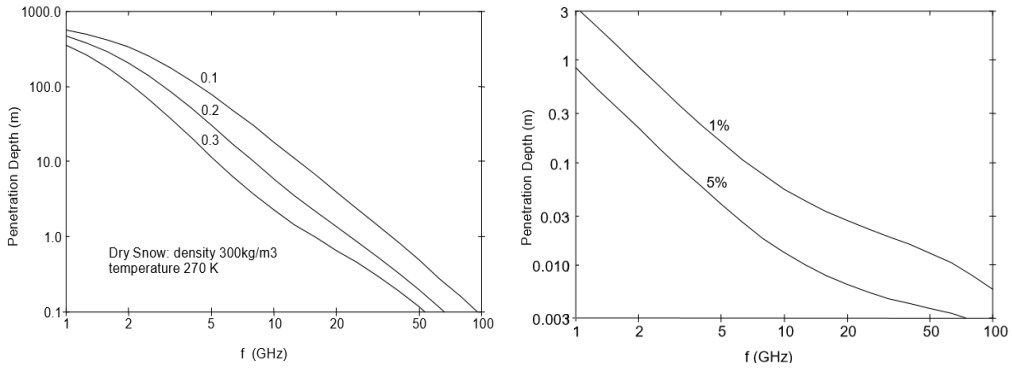

(a) (b)

Figure 3.1: Penetration depth in dry (a) and wet (b) snow versus frequency. Reproduced from [45]. For dry snow, three different crystal sizes are considered (0.1 mm, 0.2 mm and 0.3 mm). For wet snow, two different amounts of liquid water content are considered (W = 1% and W = 5% of a unit volume).

3.5 Basic Model of Bistatic Radar System

Given the limiting factors of the radar system, we can model the process with all significant effects taken into account. The electric field generated by the transmitting (TX) antenna is called $\mathbf{E}_{rad}$ and can be modeled by [40]:

$$\mathbf{E}_{rad}(r,\theta,\varphi,t) = \frac{1}{2\pi rc}\mathbf{h}_{TX}(\theta,\varphi,t) * \frac{\sqrt{Z_0}}{\sqrt{Z_c}}\frac{dV_{TX}(t)}{dt} \ , \tag{3.22}$$

where r, θ, φ are spatial coordinates, t is time, c is the speed of light in vacuum and $\mathbf{h}_{TX}$ is the transfer function of the transmitting antenna. Additionally, Z_0 and Z_c are the impedances of free space and the feed cable respectively. Finally, $V_{TX}(t)$ is the voltage applied to the antenna as a function of time and $*$ represents the time convolution between the transfer function and the applied voltage.

We can, based on equation (3.22), model the received voltage from the receiving (RX) antenna V_{RX} as:

$$V_{RX}(t) = \frac{\sqrt{Z_c}}{\sqrt{Z_0}}\mathbf{h}_{RX}(\theta,\varphi,t) * \mathbf{E}_{meas}(t) \ , \tag{3.23}$$

where $\mathbf{h}_{RX}$ is the transfer function of the RX antenna and $\mathbf{E}_{meas}(t)$ is the incident field.

When the antenna receives a propagating field, all spatial components are integrated to one signal. This is why $V_{RX}(t)$ and $V_{TX}(t)$ are scalars.

Now lets look at the process that transforms $\mathbf{E}_{rad}$ into $\mathbf{E}_{meas}$. This depends on the different travel paths (e.g. crosstalk and path via target) and can be denoted temporarily as the impulse response $\mathbf{X}(r, \theta, \varphi, t)$. Equation (3.23) becomes:

$$V_{RX}(t) = \frac{\sqrt{Z_c}}{\sqrt{Z_0}} \mathbf{h}_{RX}(\theta, \varphi, t) * \mathbf{X}(r, \theta, \varphi, t) * \mathbf{E}_{rad}(r, \theta, \varphi, t) \ . \tag{3.24}$$

Factoring out $\frac{1}{r}$ from $\mathbf{E}_{rad}$ give us the possibility to combine all antenna terms into one term $\mathbf{h}_A$:

$$V_{RX}(t) = \frac{1}{r} \mathbf{h}_A(\theta, \varphi, t) * \mathbf{X}(r, \theta, \varphi, t) \ . \tag{3.25}$$

Now, we can separate equation (3.25) into two distinct travel paths. That is, crosstalk and the other paths via the target area. We denote the impulse response of the direct path between the antennas as $\mathbf{C}_A$ and $\mathbf{T}_R$ as the impulse response of the other (non-direct) paths between the antennas.

$$V_{RX}(t) = \frac{1}{D_{TXRX}} \mathbf{h}_A(\theta, \varphi, t) * \mathbf{C}_A + \frac{1}{r} \mathbf{h}_A(\theta, \varphi, t) * \mathbf{T}_R \ , \tag{3.26}$$

where D_{TXRX} is the direct distance between TX and RX. The first term can be measured by pointing the antenna to the sky or an absorber. This term does not contain any interesting information and can be easily subtracted from any future measurement with the same configuration. The second term can contain information about the target and is, therefore, the most interesting part of the returned signal. This term contains the impulse response of the target $\mathbf{h}_T$ and clutter $\mathbf{h}_C$.

$$\mathbf{T}_R = \mathbf{h}_T + \mathbf{h}_C \ . \tag{3.27}$$

In equation (3.27) the target $\mathbf{h}_T$ can, for instance, be the transitions between densities in the snow and the clutter $\mathbf{h}_C$ is anything that adds incorrect or irrelevant information to the signal. This includes multiple reflections between layers, non-constant permittivity in the medium or high permittivity objects in the far field of the antenna that give a large relative reflection. A final term n is added to describe the inherent noise in the measurement system itself. Now we can model the received signal as:

$$V_{RX}(t) = \frac{1}{D_{TXRX}} \mathbf{h}_A(\theta, \varphi, t) * \mathbf{C}_A + \frac{1}{r} \mathbf{h}_A(\theta, \varphi, t) * (\mathbf{h}_T + \mathbf{h}_C) + n \ . \tag{3.28}$$

The received voltage $V_{RX}(t)$ is measured as a summation of all terms in equation (3.28). This is the main source of error in the radar system. However, there are several methods of coping with such errors, as described in chapter 4.

Chapter 4

Methods of Improving Radar Response

Methods of improving the radar signal are almost countless and some methods might be a lot more intuitive than others. The processing methods are divided into two specific parts. First, we cover the processing of the raw radar pulses recorded by the sensor (A-scan processing). After putting the pulses together to form an image we go through some methods to process the constructed two-dimensional (2D) data (B-scan processing).

4.1 Data Representation

In most bistatic radar measurements, 3 types of data representation are used. A-scan, B-scan and C-scan [38], [46], [47]. The A-scan is obtained during the acquisition of only one impulse response. This implies that the resulting data is only one vector containing the returned pulse.

A single A-scan provides a low amount of information. Therefore, we can combine many A-scans by moving the radar along a specified transect. This allows us to put several A-scans together and form a 2D image called a B-scan. A B-scan is normally visualized with the scanning direction horizontally and time (or depth) vertically. It can also be represented as a three-dimensional (3D) image giving the third dimension to the recorded amplitude.

Moving the radar across a grid (i.e. plane), obtaining an A-scan at each known grid point will create a C-scan giving a 3D image. This data is more difficult to visualize since it contains 4 dimensions when considering amplitude.

Regarding Colormaps

When presenting the radar image some consideration regarding color-maps should be taken. Color-map settings can drastically change the image and should therefore be chosen based on scientific studies in the same sense as other methods used to change the image. According to Borland and Taylor [48] it is important to choose color-maps that are perceptually uniform and do not range through all colors in the visual spectrum. A Python library containing perceptually uniform color-maps based on color perception research have been implemented in Matlab and used in this thesis[1]. The chosen colormap can be seen in e.g. Figure 4.4. Note that the color is arbitrary selected, as it is the distribution of intensity in the colormap that gives a perceptually uniform colormap.

In the proceeding steps, the data processing will be divided into two phases, namely A-scan and B-scan processing. A-scan processing involves the processing performed on the data vectors before forming a matrix (i.e. image).

4.2 A-scan Processing

These methods are usually the first processing techniques used in radar post-processing and do not require any tuning parameter or initialization for different measurement scenarios. The main task of the A-scan processing is to represent the measured target as truthful as possible, without any image processing or data mining.

4.2.1 Zero Time Estimation

Time zero is the time instant where the actual radar signal starts. Due to the cable length to the antennas from the radar, it will appear as if the antennas are situated the distance of the cable from where the signal started. Finding time zero means to rotate all received impulse responses so that the first data point corresponds to the spatial position of the TX antenna. This can be done by looking at the crosstalk and position that at time zero. If the antennas are spaced a significant distance apart one might want to factor in the travel time of the crosstalk. Assuming the antennas are situated in air, this can be calculated by:

$$t_{TXRX} = \frac{D_{TXRX}}{c_{air}} \ , \tag{4.1}$$

[1]Colormap scripts found at `http://bids.github.io/colormap/`

where c_{air} is the speed of light in air, t_{TXRX} is the travel time from TX to RX and D_{TXRX} is the distance between the antennas.

4.2.2 Reference Subtraction

When performing radar measurements, a reference response should be taken for calibration purposes. This can be done by pointing the radar antennas towards the sky to only collect crosstalk and atmospheric noise. If we assume that these contributions are stationary within the acquisition period; we can simply subtract the reference from the measurement. A good reference measurement can be difficult to obtain. When moving the radar system, the mechanical stress on the antenna mount might slightly move the antennas.

4.2.3 Block Averaging

Since the pulse repetition frequency (PRF) of a radar system can have sub-second periods, the number of pulses at each point might be very high, given the object (or the radar system itself) does not move very fast compared to the sampling frequency. In that case block averaging can improve the result a great deal. Since the desired response can be assumed constant over a set number of samples, some of the noise contributions that change within the block will be removed. For a matrix $\mathbf{R}_{RX}$ containing N received radar traces (A-scans), the block averaged matrix $\mathbf{R}_{BA}$ becomes:

$$\mathbf{R}_{BA}[m] = \frac{1}{B} \sum_{n=1+(m-1)B}^{mB} \mathbf{R}_{RX}[n] \quad m = 1, 2, ..., \frac{N}{B} \ , \tag{4.2}$$

where B is the size of the block (i.e. how many pulses we want to average) and the indices m and n represent each A-scan often stored as column vectors in the matrices. This form of averaging is used assuming the radar is in constant continuous motion. A modification to equation (4.2) could be made where we include overlapping blocks which in some cases improve the quality of the image.

4.2.4 Phase Modeling and Dispersion Correction

The phase response of a UWB radar might be non-linear across its bandwidth due to dispersion through the antenna [49]. Phase correction is possible by creating a model of the phase response to linearize the response. It is desirable to approximate an ideal radar as much as possible (i.e. low noise, linear phase, low attenuation and high resolution). In Hertel and Smith [49]

it is shown that the far zone electric field from a spiral antenna excited by a differentiated Gaussian pulse is a chirp. This happens because the frequency components of the pulse is transmitted at different distances from the central feed point. The proposed correction function $c(t)$ is an un-chirp signal, i.e. lower frequencies come before the higher frequencies. The Fourier transform of the correction function, $C(\omega)$ is described as:

$$C(\omega) = \frac{A}{|H(\omega)|} e^{j\Psi(\omega)} \ , \tag{4.3}$$

where $H(\omega)$ is the antenna system function, $\Psi(\omega)$ is the phase of the system function and A is an amplitude scaling constant. This function can be interpreted as a de-convolution function for the part of the system that causes the non-linear phase. The implementation of this correction function involves analysis of the measured phase of the incoming signal, where we fit a function to best describe the phase response. A good method to fit a non-linear phase response is with the non-linear least squares curve fitting, and modeling the curve as [50]:

$$\Psi_M(\omega) = a + b\omega + \frac{c}{\omega} \ , \tag{4.4}$$

where ω is the angular frequency. Here, we have linear and non-linear terms separated. If the model is a good fit the correction can be performed by simply subtracting the non-linear term $\frac{c}{\omega}$ from the measured phase.

4.2.5 Envelope Rectification with Hilbert Transform

The received back-scattered signal from a transmitted Gaussian pulse will in an ideal scenario be the first derivative of the Gaussian pulse and therefore have both positive and negative components [38]. To estimate the actual peak of the back-scattered pulse we can rectify the pulse and detect the envelope of the two peaks with the Hilbert transform [51] (see Figure 4.1).

The Hilbert transform is a method of calculating the analytic signal (i.e. no negative frequency components) from a data sequence x and is defined as [52]:

$$x_h[t] = H[x(t)] = p.v. \int_{-\infty}^{\infty} \frac{x(t-\tau)}{\pi\tau} d\tau \ , \tag{4.5}$$

where $p.v.$ denotes the Cauchy principal value of the integral that assigns values to otherwise undefined integrals [52]. Computing the discrete-time analytic signal via fast Fourier transform (FFT) is covered in Lawrence Marple [53] and is beyond the scope of this thesis.

The envelope of the received waveform is extracted using the magnitude of the analytic function constructed via the Hilbert transform. The magnitude is often displayed in terms of power. However, depending on the scale one wants to analyze the data, we can take the root of the envelope magnitude to display the pulse in terms of voltage.

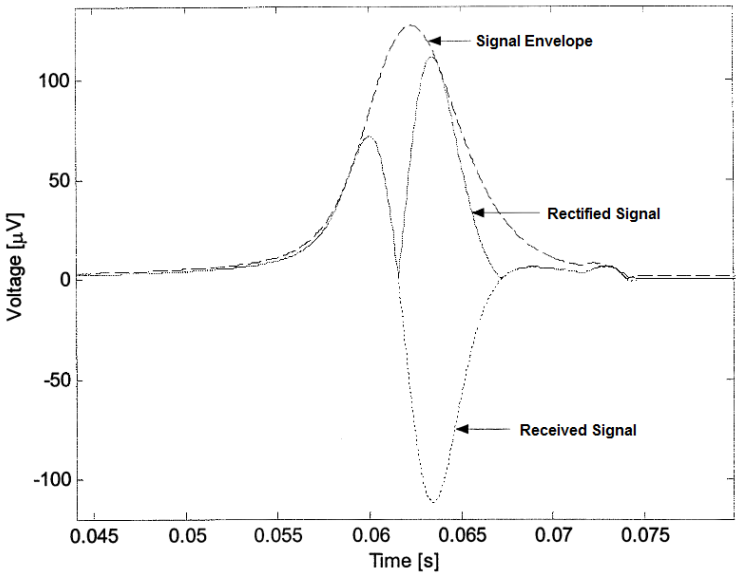

Figure 4.1: Example image. Signal envelope (dashed line) is displayed over the waveform, along with the rectified version (solid line) of the waveform. Reproduced from [51].

If the radar system suffers from low dynamics it can improve detail visibility to analyze the pulse in terms of voltage instead of power. However, it will also increase the visibility of noise. This is simply a scaling problem, but should nonetheless be addressed as it can drastically change the radar image.

4.2.6 Case Study: Relative Pulse Velocity in Snow

The electrical characteristics of snow are dynamic (in both space and time) and change as the snow alternately melts and freezes. It is useful to distinguish between dry and wet snow, where wet snow contains free liquid water.

The pulse velocity (i.e. speed) of a radio-wave is related to the medium it is propagating through by [37]:

$$v_p = \frac{c}{\sqrt{\mu_r \epsilon_r}} \ , \tag{4.6}$$

where ϵ_r and μ_r is the relative permittivity and permeability respectively. Relative permeability is regarded as one (i.e. ≈ 1) for non-magnetic materials and tiny fluctuations can be regarded as negligible in this case [38]. The imaginary part of the relative permittivity is also negligible for dry snow as the presented model in Tiuri et al. [41] is only dependent on liquid water content (see equation (4.10)). Our pulse propagation velocity equation becomes simply:

$$v_p = \frac{c}{\sqrt{\epsilon_r^{'}}} \ . \tag{4.7}$$

The relative permittivity of dry snow is linearly proportional to the density of the snow [54]. Additionally, the real part of the relative permittivity of snow is generally independent of temperature and frequency in the microwave region [54].

Using the Toikka Snow fork; we can measure the density and liquid water content of the snow. The measurements were performed in 5 cm increments down the snowpack, where at each increment the measurement was taken three times, and then averaged. For dry snow with a density less than 0.5 g/cm^3 the relative permittivity is related to the density by [41]:

$$\epsilon_r^{'} = 1 - 1.91\rho_d \ , \tag{4.8}$$

where ρ_d is the density of dry snow in g/cm^3. We have now obtained information about the relative pulse velocity through the snowpack. This will give us an even more accurate representation of our radar data. In Figure 9.2 the relative pulse velocity is plotted alongside the stratigraphy. Intuitively we can describe the implementation of relative pulse velocity as a stretching and compressing of the radar image vertically.

As we can see from equations 4.7 and 4.8, the pulse velocity is implicitly dependent on the density of snow. However, the liquid water content in snow also influences the relative permittivity (and thus the pulse velocity) significantly [41]. Even a small amount of liquid water can change the properties of dry snow. This effect needs to be considered when there is a measurable amount of liquid water in the snow. The extended model for relative permittivity is found to be [41]:

$$\epsilon_r^{'} = 1 + 1.7\rho_d + 0.7\rho_d^2 + 8.7W + 70W^2 \ . \tag{4.9}$$

In the case of wet snow, the water content also contributes to the imaginary part of the permittivity:

$$\epsilon_r^{''} = 0.9W + 7.5W^2 \ , \tag{4.10}$$

where W is the liquid water content per unit volume. Equation (4.9) and (4.10) are obtained for wet snow at 1 GHz.

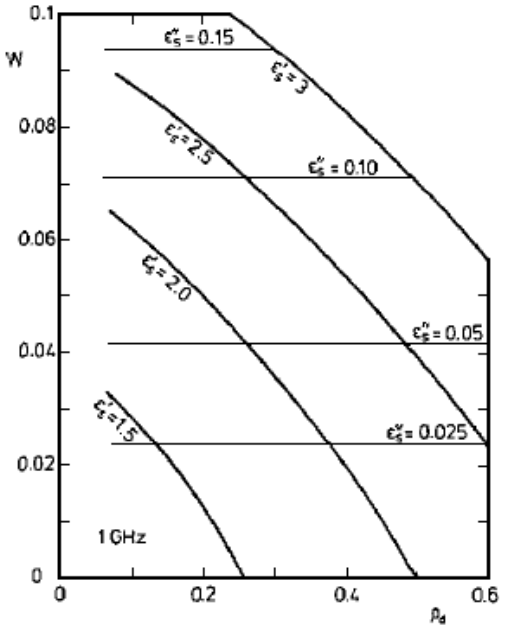

Figure 4.2: Dependence between liquid water content W , dry snow density ρ_d and relative permittivity $\epsilon_r = \epsilon_r^{'} - j\epsilon_r^{''}$ (denoted as ϵ_s in the figure). Evaluated at 1 GHz. Reproduced from [41]

As Figure 4.2 shows; the liquid water content of snow greatly increases the relative permittivity $\epsilon_r = \epsilon_r^{'} - j\epsilon_r^{''}$ (both the real and imaginary part). This in practice results in more scattering and attenuation through the snow as shown in section 10.5 (Figure 10.9). Relative permittivity is also commonly known as the relative dielectric constant.

The actual density of wet snow ρ_s is denoted as [41]:

$$\rho_s = \rho_d + W \ , \tag{4.11}$$

since the density of water is $\rho_W \approx 1$ g/cm^3.

4.3 B-scan Processing Methods

This section presents some of the methods used to process the data received from the A-scan processing stage (e.g. Zero Time Estimation, Crosstalk

Removing, and Phase Correction). Assume that the collected pulses have been put together forming a 2D image (i.e. B-scan).

4.3.1 Histogram Equalization

If all 1D radar pulses are combined to create a 2D image, some methods of image processing might improve the result. The histogram of an image is a graphical representation of the intensity distribution in an image. Consider a gray-scale image where the intensities r is in the range $[0, L-1]$. A low contrast image might have only pixel values within a short range of the total intensity range (e.g. $[\frac{L-1}{4}, \frac{L-1}{2}]$). Histogram equalization is a method of contrast adjustment where you widen the distribution of intensities [55]. The operation is done by effectively spreading out the most frequent intensity values. This often greatly improves small contrast differences in the image and in our case might extract important information about the snowpack. Histogram equalization is defined as an intensity transformation given by [55]:

$$s = T(r) = (L-1)\int_0^r p_r(w)dw \ , \tag{4.12}$$

where s are the transformed intensities, r are the intensities in the image to be transformed, $p_r(r)$ is the probability density function (PDF) of the intensities r and w is a dummy variable for integration. The right hand side of equation (4.12) is known as the cumulative distribution function (CDF) of the random variable r.

When implementing equation (4.12), we use the transformation on its discrete form:

$$s_k = T(r_k) = \frac{(L-1)}{MN}\sum_{j=0}^{k} n_j \ , \tag{4.13}$$

where MN is the total number of pixels in the image, $\sum_{j=0}^{k} n_j$ is the number of pixels with intensity r_k and L is the number of possible intensity levels in the image.

If we know the desired shape we want the pixel intensity distribution to have, then histogram specification can be used. This method is similar to histogram equalization, but here we attempt to force a defined shape on the intensity distribution. This might be useful if we want to group intensities together.

4.3.2 Sobel Mask

A Sobel mask in image processing is a technique that takes advantage of the second derivative of pixel intensities. Sudden changes (i.e. an edge) in the image will be amplified [55]. The method can be modified to only detect horizontal or vertical lines, which might be beneficial if one is looking to detect specific shapes in an image.

The operator uses two 3-by-3 kernels which are convolved with the original image to calculate approximations of the derivatives. One for detecting horizontal lines and one for vertical lines.

$$\mathbf{G}_x = \begin{bmatrix} -1 & 0 & 1 \\ -2 & 0 & 2 \\ -1 & 0 & 1 \end{bmatrix} * \mathbf{A} \ , \tag{4.14}$$

$$\mathbf{G_y} = \begin{bmatrix} -1 & -2 & -1 \\ 0 & 0 & 0 \\ 1 & 2 & 1 \end{bmatrix} * \mathbf{A} \ , \tag{4.15}$$

where $\mathbf{A}$ is the image matrix. $\mathbf{G_x}$ and $\mathbf{G_y}$ are the horizontal and vertical derivative approximations, respectively.

The Sobel image is then calculated by finding the gradient magnitude.

$$\mathbf{G} = \sqrt{\mathbf{G}_x^2 + \mathbf{G}_y^2} \ . \tag{4.16}$$

A final sharpened image might be produced by adding the original image and the Sobel image to give a combination of the two.

$$\mathbf{B} = \mathbf{A} + k\mathbf{G}, \tag{4.17}$$

where k is a tuning factor (typically between 0 and 1) to set how much the Sobel sharpening should affect the image.

4.3.3 Canny Edge Detection

A much more accurate edge detection algorithm compared to the Sobel mask is the Canny edge detector. The optimal 1D step edge detector is the first derivative of a Gaussian. The Canny method generalizes this detector for 2D while acknowledging that the direction of the normal to the edge is unknown. This involves applying the 1D edge detector in all directions, which is approximated by smoothing the image with a circular 2D Gaussian function, computing the gradient of the result and using the gradient magnitude and direction to estimate edge strength and direction at every pixel.

Let $f(x, y)$ denote the image and $g(x, y)$ denote the Gaussian function [55]:

$$g(x, y) = e^{-\frac{x^2+y^2}{2\sigma^2}} \ . \tag{4.18}$$

The smoothed image $f_s(x, y)$ becomes the convolution between $g(x, y)$ and $f(x, y)$:

$$f_s(x, y) = g(x, y) * f(x, y) \ . \tag{4.19}$$

If we denote $g_x = \frac{\partial f_s}{\partial x}$ and $g_y = \frac{\partial f_s}{\partial y}$, we can express the gradient magnitude and direction (i.e. angle) as:

$$M(x, y) = \sqrt{g_x^2 + g_y^2} \ , \tag{4.20}$$

and

$$\alpha(x, y) = \tan^{-1}\left[\frac{g_y}{g_x}\right] \ . \tag{4.21}$$

We now find the direction line d_k that is closest to $\alpha(x, y)$ for each pixel (closely related to the operations presented in section 4.3.5). If the value of $M(x, y)$ is less than at least one of its two neighbors along the line d_k let the suppressed image $g_N(x, y) = 0$ otherwise set $g_N(x, y) = M(x, y)$. This is called the non-maxima suppressed image. The final operation is to threshold the suppressed image using hysteresis thresholding which applies two thresholds: a low threshold and a high threshold. We create two separate images based on the low and the high thresholds. The low threshold image contains all the non-zero values from the high threshold image since the low image is formed with a lower threshold. We subtract the high threshold image from the low threshold image and what remains is two images high and low containing the strong and weak edge pixels of the image respectively. To put long edges together we can use e.g. 8-connectivity to set the weak edge pixels in the strong group if they are connected. Canny's edge detection approach is summarized with the following basic steps [55]:

- Smooth the input image with a Gaussian filter
- Compute the gradient magnitude and angle images
- Apply nonmaxima suppression to the gradient magnitude image
- Use double thresholding and connectivity analysis to detect and link edges

4.3.4 Wiener Adaptive Filter

The Wiener filter is used to produce an estimate of a desired random process by filtering an observed noisy process, assuming that noise and image are uncorrelated. The Wiener filter minimizes the mean square error between the estimated random process and the desired process [55]. The filtering algorithm uses a neighborhood of N-by-M pixels [56].

First, we estimate the mean and variance around each pixel based on the predefined neighborhood.

$$\mu = \frac{1}{NM} \sum_{n_1,n_2 \in \eta} a(n_1, n_2) \ , \tag{4.22}$$

$$\sigma = \frac{1}{NM} \sum_{n_1,n_2 \in \eta} a^2(n_1, n_2) - \mu^2 \ , \tag{4.23}$$

where a is the image, μ is the local mean, σ is the local variance and η is the N-by-M neighborhood. Then we create a pixel-wise Wiener filter based on these estimates.

$$w(n_1, n_2) = \mu + \frac{\sigma^2 - v^2}{\sigma^2}(a(n_1, n_2) - \mu) \ , \tag{4.24}$$

where v is the noise variance. The noise variance v can be estimated by taking the average of all local variance estimates if we do not have any information about the noise.

This filtering method is excellent at removing Gaussian noise without blurring the image to the extent an i.e. mean filter might. In this project, the Wiener filter will be used to some extent to improve the overall impression of the image and make differences more visible.

4.3.5 Hough Transformation

The Hough transform is a method of feature detection used for detecting lines, but also shapes (e.g. ellipses, circles). It utilizes the fact that any line relative to a specified origin can be expressed as [55]:

$$\rho = x \cos\theta + y \sin\theta \ , \tag{4.25}$$

where ρ is the distance from the specified origin to the closest point on the line and θ is the relative angle of the distance r to the origin. Each line segment in the image can, therefore, be associated with a pair of variables (ρ, θ). The (ρ, θ) plane is referred to as the Hough space. The computational attractiveness of the Hough transform arises from sub-dividing the (ρ, θ) parameter

into so-called accumulator cells [55]. This involves dividing the Hough space into cells where $-90° \leq \theta \leq 90°$ and $-D \leq \rho \leq D$. Here, D is the maximum distance between opposite corners in an image. Initially, these cells are set to zero. Then, after binary edge detection (e.g. Canny edge detection and binary thresholding) to separate background pixels from the objects, we let a non-background pixel (x_k, y_k) contribute with its corresponding ρ and θ values. This is done by setting θ equal to all of the values on the θ-axis and solving for ρ using the equation $\rho = x_k \cos\theta + y_k \sin\theta$. The calculated ρ values are rounded to the nearest cells along the ρ axis. Now we have a plot of the pixels in the Hough space.

To detect prominent lines we need to look for intersections of plots in the Hough space. This is done by examining the counts of the accumulator cells for high pixel concentrations. For high concentrations, we examine the continuity between pixels in a chosen cell. This involves computing the distance between disconnected pixels corresponding to the same accumulator cell. The gaps between the pixels are bridged if the length of the gap is below a specified threshold. Additionally, if we are only searching for lines of a specified angle one can examine a specified segment of the θ axis containing the angles in the region of interest.

Let us consider a case where we have three white pixels on an otherwise black image (see Figure 4.3a). Note that the intensity in Figure 4.3a is inverted for visibility purposes. For each white pixel, we plot a number of lines through the pixel at different angles. We then draw a line from a defined origin to each line with a perpendicular intersection and measure the length and angle of that line (i.e. for each line from the origin to the point of perpendicular intersection, we collect a length and angle relative to the origin). This length and angle become our ρ and θ.

As seen in Figure 4.3a, each pixel gets a set of angles θ and a set of distances ρ, where the ρ line is perpendicular to each angle line through the pixel. If we plot all the angles θ and distances ρ we get a Hough space as seen in Figure 4.3b.

The plot intersections in the Hough space indicates prominent lines that can be quantified. In this example, we have three pixels on a line that is $-45°$ and passes through the origin. This can be seen in the Hough space by looking at the point of intersection between the three plots. To separate strong and weak lines, a threshold can be applied to the Hough space before extracting the line information.

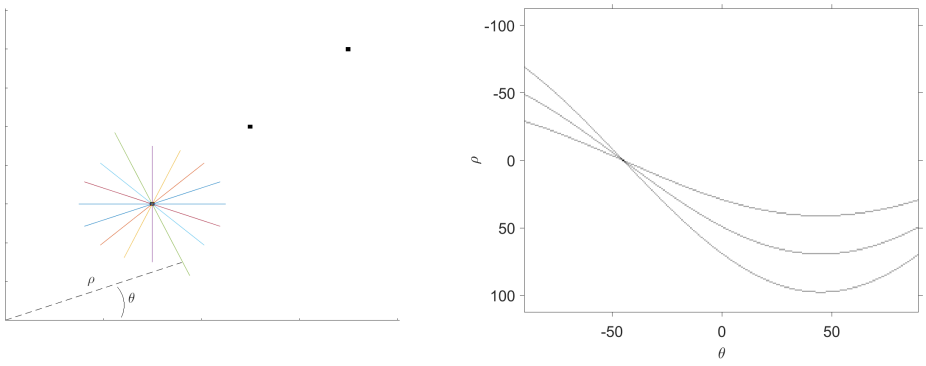

(a) (b)

Figure 4.3: Hough example image consisting of three white pixels on an otherwise black image, with visualization of angle and position of each pixel (a) and the resulting Hough space (b). Intensity inverted for visibility.

4.3.6 Eigen Image Filtering by SVD

Some radar images have problems with ringing. If the image is severely contaminated by ringing noise, the noise can be regarded as a component which is the most consistent when correlated with the contaminated image. Thus we can remove the noise component using the eigen image filtering technique. Let $\mathbf{R}$ be the radar data matrix with N vertical samples and M traces (i.e. $M \times N$ image). The singular value decomposition (SVD) of $\mathbf{R}$ is given by [57]:

$$\mathbf{R} = \mathbf{U}\mathbf{S}\mathbf{V}^T \ , \tag{4.26}$$

where $\mathbf{U}$ and $\mathbf{V}$ are orthogonal matrices of $M \times M$ and $N \times N$ respectively and $\mathbf{S}$ is an $M \times N$ diagonal matrix containing the singular values s_i of matrix $\mathbf{R}$. Matrices $\mathbf{U}$ and $\mathbf{V}$ are composed of column vectors $\mathbf{u}_i$ and $\mathbf{v}_i$. The multiplication of $\mathbf{u}_i$ and $\mathbf{v}_i$ creates an $M \times N$ matrix $\mathbf{E}_i$ which can be regarded as an image containing one of the components in the image. By choosing which components to keep we can remove unwanted noise or other features in the image. The first components of the image are regarded as the most correlated and the last parts are the least correlated. Thus we can choose to use the most correlated parts and remove the uncorrelated parts. Alternatively, we can create band-pass eigen images by rejecting highly correlated as well as highly uncorrelated parts of the image (e.g. $p = 2$ and $q = 10$).

$$\mathbf{R}_{filtered} = \sum_{i=p}^{q} s_i \mathbf{E}_i \ . \tag{4.27}$$

SVD of images can also be used as an image compression method by only storing a some $\mathbf{u}_i$, $\mathbf{v}_i$ and s_i and performing the inverse operation afterwards to regenerate the image [58].

4.4 Migration Techniques

In the field of ground penetrating radar, migration techniques have been extensively used for several decades. The method is closely related to synthetic aperture radar (SAR) and involves moving the radar over a target and summing the contributions from all reflection traces.

By moving the antenna system along a selected transect above the ground surface a two-dimensional reflection profile (i.e. radargram or B-scan) is obtained. For each recorded location of the antenna system (defined by the acquisition time for each pulse), a trace is achieved where the amplitude and the delay time of the recorded echoes are drawn. This reflection profile gives a somewhat blurred image of the targets due to the scattering of the electromagnetic waves in the medium [47].

Consider the case where we have a point scatterer (an object small in terms of the shortest radiated wavelength) situated in a homogeneous medium. The contribution from each trace will result in a hyperbolic response through the scan. If the measured time to the point reflector is t, then the distance to the point reflector is given by $z = \frac{vt}{2}$.

At any position along the x-axis the distance z to the point reflector and back is given by [38]:

$$z_i = 2\sqrt{(x_i - x_0)^2 + z_0^2} \ . \tag{4.28}$$

Thus the two way travel time for any position becomes:

$$\tau = \frac{2}{v}\sqrt{(x - x_o)^2 - z^2} \ . \tag{4.29}$$

These equations show that the measured wavefront appears as a hyperbolic curve as shown in Figure 4.4.

The shape of the hyperbola depends on the electromagnetic properties of the medium (can be several sub-media) that is investigated, the configuration of the antennas (mono-static or bi-static) as described in section 3.3 and the depth of the scatterer. Migration techniques aim at compensating for such a spreading by re-focalizing each segment of the hyperbola to its apex [47].

In Soldovieri and Solimene [47] and Margrave [59], different techniques for de-cluttering and focusing the reflection profile are presented. In short, one can categorize most methods as either migration algorithms or inverse filtering algorithms. We will focus on migration algorithms and especially the summation diffraction beamforming method as it is the most straightforward method to implement a test before moving on to more advanced methods. Later we will look at the theory behind F-K migration which is a much faster method utilizing the spatial 2D Fourier transform for faster computation. To fully understand how F-K migration works one must first investigate the more fundamental methods of migration in the spatial domain. Here Summation Diffraction forms a basis for the presented theories.

4.4.1 Summation Diffraction

The Summation Diffraction (also known as Delay and Sum in ultrasound processing) beam-forming algorithm is a simple and robust method to migrate the scattered response of a target together. However, compared to Fourier domain methods (e.g. F-K migration as explained later) Summation Diffraction is computationally expensive. We will continue with the example of a point scatterer situated in an otherwise empty domain.

The point scatterer is located at the coordinate vector $\mathbf{r_{sc}} = (x_{sc}, z_{sc})$ and have $\mathbf{r_o} = (x_0, 0)$ as the coordinates of the positions where the scattered field is recorded as shown in Figure 4.4. In our example we have a homogeneous medium with no dielectric transitions and $x_0 \in [-X_M, X_M]$, where the synthetic measurement aperture $\Sigma = [-X_M, X_M]$ represents the transect we move the radar across. The direction of motion used here is normally described as the azimuthal direction.

.

If the transmitted signal (ideally a delta impulse) is denoted as s_T, the back-scattered field is given by [47]:

$$s_R(\mathbf{r}_0, t) = s_T\left(t - 2\frac{|\mathbf{r}_0 - \mathbf{r}_{sc}|}{v}\right) . \tag{4.30}$$

For a point scatterer we perform the following operation for all pixels in the image ([47, 60, 61, 62]): For each pixel a diffraction hyperbola is constructed in the two-dimensional reflection profile. The reconstruction at each pixel is then obtained by summing all the traces that the synthetic hyperbola intersects in the image. In computational terms; for each z pixel depth we calculate the two-way travel time to all x pixels from all radar positions and time shift the traces by their corresponding calculated time.

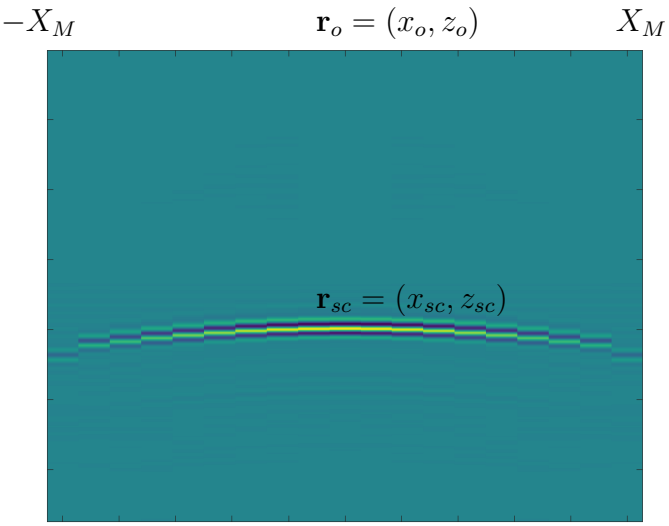

Figure 4.4: Radar response of a point-object. Generated from synthetic data.

Then we sum all pulses at the region (depth) of interest. This results in an alignment of the pulses at the apex of the hyperbola.

The operation can be described for each pixel (x, z) by the double integral [47]:

$$R(x,z) = \int_{\Sigma}\int_{T} s_R(\mathbf{r}_0, t)\delta\left(t - \frac{2}{v}\sqrt{(x-x_o)^2 - z^2}\right) dx_o dt \ , \tag{4.31}$$

where Σ is the measurement aperture, is T the acquisition time of each measurement and $R(x, z)$ is the migrated data. This is known as the Summation Diffraction method.

To demonstrate the effects of summation diffraction we use a synthetic dataset to test the method. The dataset simulates a bistatic setup of two Vivaldi antennas scanning a small sphere target 80 cm from the antennas. The antennas are spaced 40 cm apart and move in 5 cm increments between each scan. This allows us to calculate the total pulse travel distance from the transmitting antenna to each pixel in the radar image and back to the receiving antenna. Each pulse can be time-shifted according to the calculated distance for each pixel.

For the bistatic antenna setup equation (4.28) becomes:

$$z_i = \sqrt{\left(x_i - x_0 - \frac{D}{2}\right)^2 + z_0^2} + \sqrt{\left(x_i - x_0 + \frac{D}{2}\right)^2 + z_0^2} \ , \tag{4.32}$$

where D is the distance between the transmitting and receiving antenna.

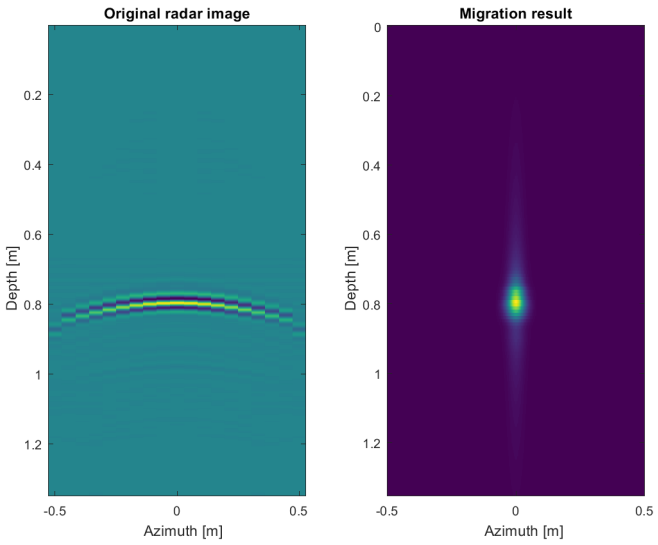

Figure 4.5: Migration result compared to original signal.

As we can see in Figure 4.5, adding contributions across the transect of the radar scan can improve the response significantly. However, from the radar equation, we know that the signal to noise ratio (SNR) will fall by $\frac{1}{z_i^4}$, which means that an increasing distance to the target (i.e. contributions to the summation far away from the target) also decreases SNR. Also, as the angle of radiation on antennas start to approach the side of the main lobe the phase center of the antenna will move to a different location [61] within the antenna structure. This will inevitably clutter the image.

Being aware of these consequences, we can still attempt to give the received pulses a weight based on their location in the image. This enables the pulses at the far sides of the image to contribute more to the summation giving more focusing of the target.

This particular weighting gives all received pulses the same amplitude as the center pulse. This is a brute force method and can be refined for better results.

In Figure 4.7 the focusing is somewhat visible in the x direction. However, notice the ringing effects caused by the weighting especially visible when looking at the pixel values for a horizontal line across the image at the center of the target. Even though minuscule in this synthetic dataset, this effect is important to be aware of when processing real data. This might be avoided with more refined methods of weighting (e.g. Gaussian windowing).

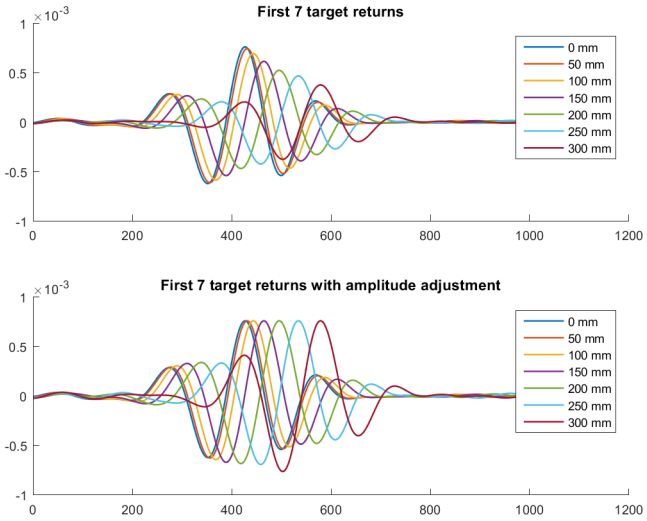

Figure 4.6: Recorded pulses before and after weighting. The noted distances for each plot are the offset from the center of the image.

To reduce the computational load of this algorithm the computation can be performed in the Fourier domain instead. This is commonly known as F-K migration.

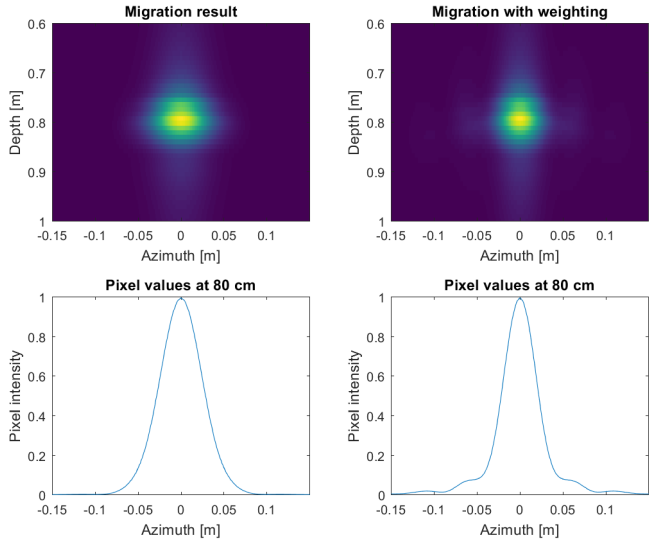

Figure 4.7: Migration results with and without amplitude weighting. Below each image is the Azimuth pixel values of each image.

4.4.2 F-K Migration

F-K migration is a generalization of the Doppler migration technique used in SAR imaging [47]. The technique is widely used in GPR [38] and ultrasound imaging [63]. F-K migration utilizes the F-K transform to migrate the scattered return. The F-K transform is a two-dimensional Fourier transform over time and space. Now, consider the expression in equation (4.31). If we denote the Fourier transform of $s_R(\mathbf{r}_0, t)$ as $S_R(\mathbf{r}_0, \omega)$ we can rewrite the equation as:

$$R(x,z) = \int_\Sigma \int_\Omega S_R(\mathbf{r}_0, \omega) \exp\left(j\frac{2\omega}{v}\sqrt{(x-x_o)^2 - z^2}\right) dx_o d\omega \ . \tag{4.33}$$

Inserting $k = \frac{\omega}{v}$ rewrites equation (4.33) in terms of integration of wavenumber k instead:

$$R(x,z) = \int_\Sigma \int_{\Omega_k} S_R(\mathbf{r}_0, k) \exp\left(j2k\sqrt{(x-x_o)^2 - z^2}\right) dx_o dk \ , \tag{4.34}$$

where Ω_k now denotes the frequency band in the k domain. This expression is essentially a convolution in x_o and an integration in k. The convolution can be computed in the spatial Fourier domain. From [47] we can get the

full derivation of this expression which recasts the transform in terms of the spatial spectral k_x and makes some assumptions such as ignoring the amplitude factor. The resulting F-K migration expression becomes:

$$R(x,z) = \int_{\Omega_{kx}} \int_{\Omega} S_R(k_x,\omega) \exp(-jk_x x) \exp(jk_z z) dk_x d\omega \ . \tag{4.35}$$

Inverse filtering has shown to perform slightly better in terms of reconstructing the target [47]. However, F-K migration has a lower computational cost and will in many low noise cases perform as good as inverse filtering. A further study of migration methods for radar signal processing is presented in Sayedelahl and Bording [64] where more complex methods are investigated (e.g. reverse time migration and exploding reflector modeling).

In Lertniphonphun and Mcclellan [65] migration techniques are presented for UWB SAR systems where it is pointed out that the assumption of constant pulse propagation velocity will blur or shift target locations for media with non-constant pulse propagation velocity. This complicates the task of migrating the radar signal from snowpacks significantly, as there are several transitions in density (i.e. pulse propagation velocity) throughout the snowpack. Aftanas et al. [66] present a migration method to compensate for dielectric transitions with through-wall radar imaging. However, in that case, there is only one layer (i.e. the wall) instead of several as in a snowpack.

Part II

System Description

Chapter 5

Radar Sensor Systems

In the task of obtaining snow profiles from radar imagery, one should try different approaches to identify the most suitable method. Therefore, two different radar systems have presently been tested. The systems vary in almost all respects including signal excitation method, data acquisition, antenna type and performance characteristics (bandwidth, resolution, and output power). However, the general set up is quite similar: In Figure 5.1 we see how the parts in a typical bistatic radar system work together. This is identical for both systems tested in this project. In the following sections, we will describe the radar sensors, antennas, and the physical platform used to obtain the measurements.

The control PC has custom developed software that activates the radar sensor and requests a sample. The radar sensor, in turn, sends a signal via coaxial cables to the TX antenna that radiates the signal towards the target. The scattered response of the target is then collected by the RX antenna and sampled by the radar sensor. Thereafter, raw data is delivered back to the control PC for storage and further processing.

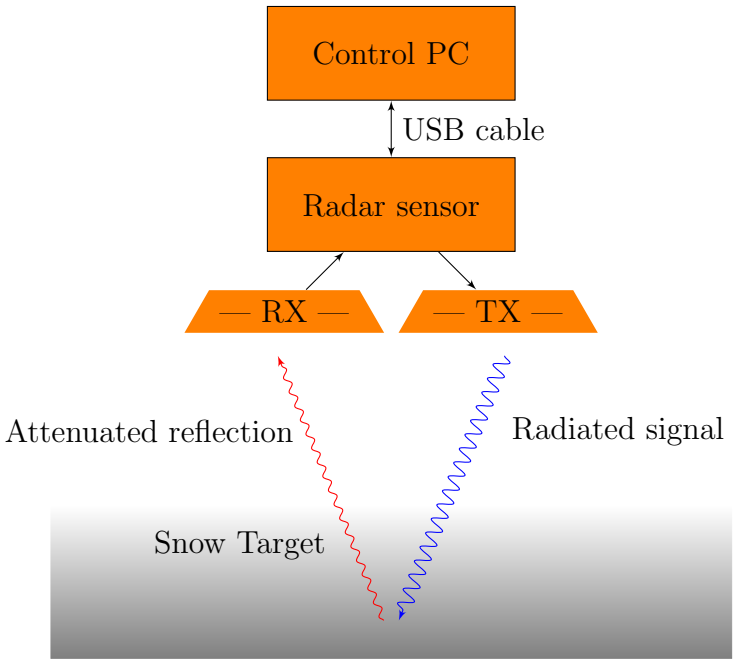

Figure 5.1: Bistatic radar system setup

5.1 ILMsens SH-3100 m:explore

This newly developed commercial UWB sensor has several desirable characteristics concerning high resolution radar imaging[1] . Using their own developed m-sequence pseudo random noise (PRN) signal generator, this sensor performs well for radar sensing tasks. Especially, when we have restrictions regarding high peaks of energy commonly associated with pulse radars. The sensor has a transmitter and two receivers working in parallel. This double receiver can be useful for detecting composite polarizations which might be desirable for some applications.

[1]Visit the ILMsens website at: `http://ilmsens.com/index.php/en/m-explore`

Table 5.1: ILMsens Sensor RF properties (from the ILMsens m:explore datasheet [67])

Transmitter
UWB pseudo-noise signal
No high voltage peaks, low field strength operation
(when connected to antennas)
Extremely stable generation driven by phase locked RF clock
Instantaneous -10 dB bandwidth 0.1 - 6 GHz
Total output power: approximately -7 dBm
Observation time window: 39.3 ns
Unambiguity range (two way travel): 5.9 m (air)
Receiver
UWB analogue input bandwidth beyond: 0.1 - 6 GHz
Continuous, synchronous sub-sampling operation
Extremely stable timebase derived from transmitter clock with
timebase jitter less than 20 fs (rms)
Digital Backend
Measurement rate, up to 1000 samples per second
(actual max. rate depends on capabilities of control computer)
Digital correlation in control computer to suppress noise

5.2 M-sequence Signal Generation

"A maximum length binary sequence (MLBS), in short an M-sequence, is a special kind of pseudo random binary sequence (PRBS)" [38]. This sequence is called pseudo-random because it is to some extent periodic using maximal-length linear feedback shift registers reproducing every binary sequence (except the zero vector) that can be represented by the shift registers. They have, however, properties which are very close to those of real random signals. Since the shift registers are very large (a large number of bits), the number of clock pulses, before one period of the number series (usually Fibonacci) is completed, is relatively large. In our acquired radar sensor we have 9 bits (511 possible values). This is what is meant by pseudo-random noise (PRN), as it can be approximated as white noise. The autocorrelation function of this sequence will in principle be a delta function, which in turn gives us a wide power spectral density [68]. This is one of the basic requirements for UWB radar signals.

Now, due to the random nature of the radiated signal, the received reflection of the target will also be of random nature. Therefore, we must

examine the cross-correlation function between the input and output to be able to analyze the back-scattered return. The information of interest in most radar-measuring situations is the impulse response of the target $h(\tau)$.

If we have a radiated output signal $x(t)$ and return signal $y(t)$; these are related to the impulse response by a convolution [38]:

$$y(t) = h(t) * x(t) \ . \tag{5.1}$$

The autocorrelation and cross-correlation are also related to the impulse response by a convolution [38]:

$$R_{yx}(\tau) = h(\tau) * R_{xx}(\tau) \ . \tag{5.2}$$

If the autocorrelation is a delta function $R_{xx}(\tau) = \delta(\tau)$, equation (5.2) simplifies to:

$$R_{yx}(\tau) \sim h(\tau) \ . \tag{5.3}$$

Practically, this means that the cross-correlation function between the received signal and stimulus is proportional to the impulse response function as long as the autocorrelation function of the stimulus is narrow compared to the impulse response of the device under test (i.e. an impulse/delta function $\delta(\tau)$). This method can be compared to exciting the antenna with an impulse (e.g. Gaussian pulse) but has some differences. Here, we must first determine the cross-correlation function to be able to find the impulse response.

The most important result gained with this method is the ability to replace impulsive waveforms by signals, which spread their energy equally over a long time, hence reducing the peak power. For this reason, the electronic components only have to handle low voltage signals, which allows for cheap and low noise circuit integration [69]. Moreover, for active components, the nonlinear distortion will also be reduced compared to pulse excitation due to the low peak power of m-sequence excitation [37]. Furthermore, the charge and discharge of parasitic circuit elements profit from low voltage variations, which results in an increased bandwidth of the signals.

From Figure 5.2 one can intuitively see that the radio frequency (RF) clock rate f_c plays a vital role in defining the performance of the sensor. In addition, the length of the shift registry also affects central characteristics of the sensor. Some of the key parameters for this system is described below.

Bandwidth: We can with some simplification relate the bandwidth to just one variable; the clock rate f_c [38]:

$$BW \approx \frac{f_c}{2} \quad [Hz] \ . \tag{5.4}$$

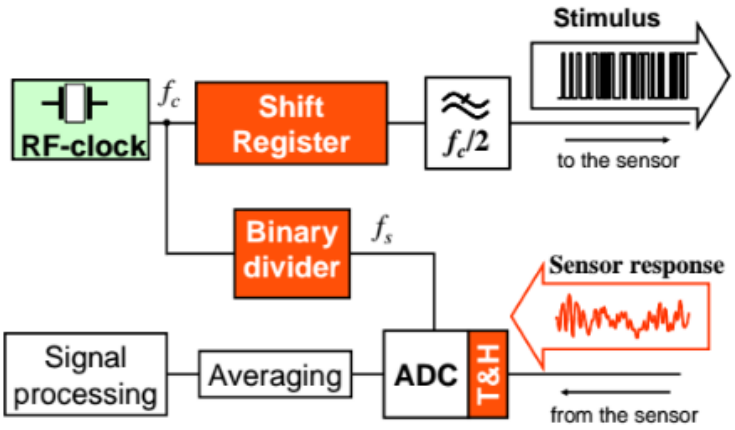

Figure 5.2: Basic concept block diagram of UWB m-sequence. Reprint from [70]. Note f_c is the RF clock rate.

Observation time window length: This characteristic tells us the time it takes to run through all the values of the shift register up to the maximal length. If the shift register has a size of m bits, then the maximal length (i.e. period) is $2^m - 1$. The observation time window length T is defined as [38]:

$$T \approx \frac{2^m - 1}{f_c} \quad [s] \ . \tag{5.5}$$

The total time to acquire a sampled signal depends on the binary divider, the internal averaging of the radar sensor and eventually the processing capabilities of the control PC.

Range resolution: The range resolution δ_r is an important quantity as it tells us what size of objects we will be able to resolve. Range resolution can be approximated by [38] :

$$\delta_r \approx \frac{c}{f_c} \quad [m] \ , \tag{5.6}$$

where c is the speed of light in vacuum.

Unambiguity range: The maximum range at witch a target can be located is restricted by the observation time window length. The unambiguous range R_0 can be expressed as [38]:

$$R_0 = \frac{cT}{2} = \frac{c(2^m - 1)}{2f_c} \ . \tag{5.7}$$

In table 5.2 unambiguous range for air, dry snow and wet snow is calculated, using average permittivity, and assuming that the entire range of the radar is the same material. In practice, some of the range will be air, some will be snow and some will be soil. This measure is only to give an impression of the range through different materials based only on relative pulse velocity and observation time window length, not factoring in dielectric and spreading losses.

The sampling operation of the m-sequence radar utilizes the fact that in contrast to random noise, pseudo-random noise represents a periodic signal [71]. This facilitates for sub-sampling (i.e. under sampling) which drastically reduces the speed requirements for the receiving electronics. Clearly, the measurement time will be expanded by that approach, but it can be accepted in many cases because the propagation speed of the radar signal is orders beyond a typical target speed. However, the sample timing must be as accurate as possible as UWB signals change their voltage rapidly. In all electronic timing systems, a point in time is defined by crossing a threshold level with a rising (or falling) edge. Since neither the threshold or edge are perfectly sharp, there will be timing errors. This might result in drift errors due to an unstable threshold or non-equidistant sampling intervals due to a non-linear ramp. The use of swept thresholds when sampling (as described in section 5.4) provide these problems.

Due to the periodicity of the PRN signal, the sampling process can be distributed over several periods. If the spectral band of the transmitted signal is limited to $f_c/2$, only one sample per registry chip can be sampled with the Nyquist-Shannon theorem held. To reduce and control the data capturing rate, a binary divider is used to control a track & hold (T&H) analog-to-digital converter (ADC). A T&H ADC captures the voltage and holds its value at a constant level for a specified time, in this case controlled by the binary divider (see Figure 5.2). This method of sampling is excellent regarding time stability since all trigger events are based on steep flanks, and threshold levels must not be swept. The remaining noise contribution comes from additive noise as well as phase noise and drift of the RF-clock.

5.2.1 Why m:sequence?

Considering previous work (section 1.4) regarding snow stratigraphy scanning with radar systems, where most studies have used FMCW radars, the choice of using PRN m:sequence radar should be addressed. The m:sequence method is compared to real pulse excitation with the two radar systems that have been used during the measurement campaign. However, an FMCW radar was not available and was therefore not tested during the measurement

campaign. In Sachs, Gmbh, and Ilmenau [72] and Ng, Feger, and Stelzer [73] the PRN radar technique (i.e. m:sequence) is thoroughly described and compared to FMCW and pulse radar methods. The main advantage PRN has against FMCW is that the PRBS generator in PRN radars need far less digital building blocks than the FMCW voltage controlled oscillator (VCO) (i.e. frequency synthesiser), enabling single chip integration which reduces cost, size and power consumption while still maintaining the same target resolution. Additional effort is also needed to keep the VCO linearised and stable. Linearity in VCO's usually decrease with increased sweep bandwidth where sweep non-linearities result in a widening and a shift of peaks along the frequency axis, thus degrading the resolution. PRN and pulse radars do not need a linear frequency sweep as a TX signal and thus avoids these problems.

5.3 Ultra Wideband Snow Sensor

The ultra wide band snow sensor (UWiBaSS) is a radar system specifically designed to detect variations and layer configuration in snow. The radar system was developed at UiT The Arctic University of Norway. It consists of an ILMsens m:explore sensor connected to a single board computer running ILMsens developed software to acquire and log the impulse responses. In addition, the system uses two Archimedean spiral antennas (one RX one TX) for transceiving the signals (see Figure 5.3).

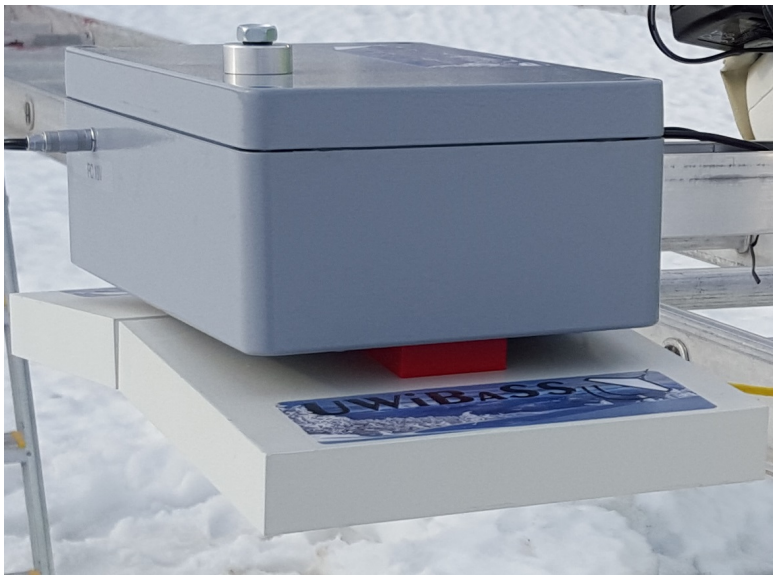

Figure 5.3: UWiBaSS system with antennas at the bottom. ILMsens sensor and control PC mounted inside the box.

5.3.1 The Archimedean Spiral Antenna

Spiral antennas belong to the class of "frequency independent" antennas. Impedance, radiation pattern and polarization of these antennas remain almost unchanged over a large bandwidth. This type of antenna is widely used in sensing applications where a very large bandwidth is desired. With a fractional bandwidth of up to 30:1, these antennas can e.g. be efficient from 1 GHz up to 30 GHz. Spiral antennas are inherently circularly polarized from its construction and have a radiation beam with maximum perpendicular to the plane of the spiral. The HPBW is approximately $70 - 90°$. In this study, the antennas are designed with two "arms" extending from the center of the dielectric plate and fed with a balanced signal through a balun (see Figure 5.4). A balun converts between an unbalanced signal and a balanced signal. However, these antennas can be constructed with any number of arms, even with one arm and a backing ground plane that does not need a balanced feed signal [74].

As we can see in Figure 5.5 the antenna has a bidirectional radiation-pattern. To make the antenna operate in only one direction one could use metallic cavity backing (often used in narrow-band systems), but this would greatly reduce the bandwidth since the reflected field will tend to cancel the forward traveling field for certain frequencies. To keep the wide-band characteristics one could include an absorbing material inside the enclosure

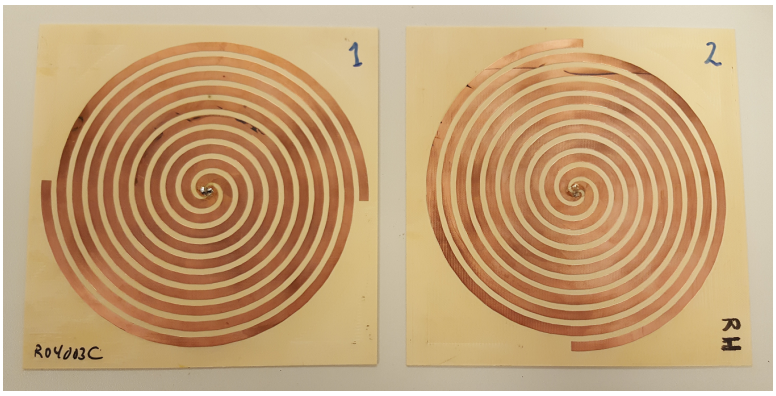

Figure 5.4: Archimedean spiral antennas manufactured at the UiT The Arctic University of Norway; ready for mounting in an aluminum frame with absorbing material in the back.

of the antenna at the cost of antenna efficiency. Because of the symmetry of the antenna, this loss of efficiency is often estimated to be about 3 dB, which might be tolerable depending on the application.

The impedance of the antenna is relatively stable over a large bandwidth. This, in turn, gives a low and stable return loss when matched to a transmission line. Return loss if often denoted as S_{11} from scattering matrix theory [37].

In Figure 5.6, the simulated return loss shows stability over a large bandwidth, with maximal effectiveness at approximately 2.5 GHz. This antenna will prove to have significantly more stable return loss than the Vivaldi antenna mentioned in section 5.4 (see Figure 5.10b).

The antennas have a measured bandwidth of approximately 950 MHz - 11 GHz. However, the radar sensor operates at 0.1 - 6 GHz bandwidth, thus the radar sensor and antenna bandwidth do not completely overlap. This is due to the size restrictions when designing the antennas. To facilitate a bandwidth all the way down to 0.1 GHz would result in a spiral radius too large for mounting on a UAV (see equation (5.8) and (5.9)). The highest frequencies within the antenna bandwidth radiate from the inner parts of the spiral which in principle could be removed, but with no improvement in performance or size. It should be noted that the extra space gained in the center of the spiral could be used to mount a low noise pre-amplifier.

The antennas were placed in a metallic housing with absorbing material in the backing cavity to remove the rear lobe of the antenna while still keeping the wide-band characteristics. As previously stated; this causes a reduction of 0.5 (50 %) in antenna efficiency (i.e.3 dB gain loss). There are several suitable antenna designs for snow measurement applications [75], however,

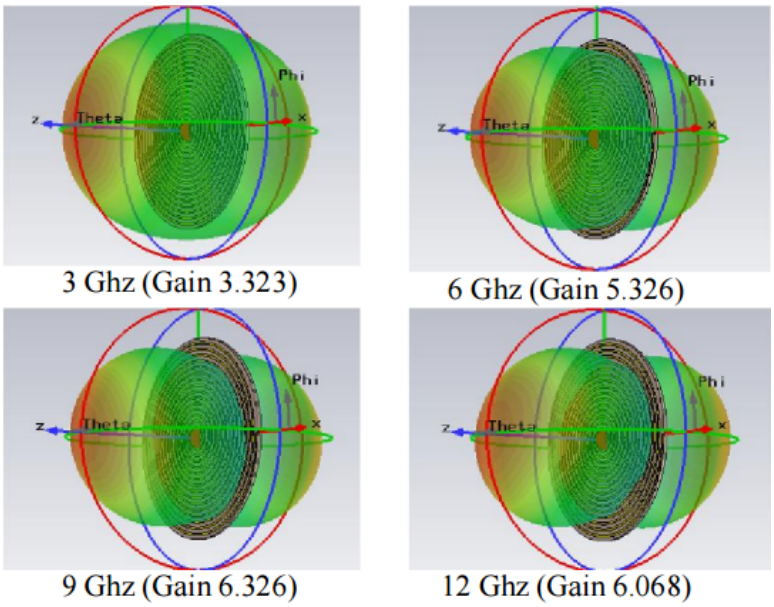

Figure 5.5: Simulated radiation pattern of Archimedean Spiral Antenna. Reprint from [42]

the Archimedean spiral antenna has an impedance stability over a very large bandwidth that is hard to match with other antenna designs. The lowest operating frequency of the Archimedean spiral antenna can be estimated by [76]:

$$f_{low} = \frac{c}{2\pi R_2} \ , \tag{5.8}$$

where R_2 is the outer radius of the spiral. Solving for R_2 with $f_{low} = 0.1$ GHz as the lowest frequency give us:

$$R_2 = \frac{c}{2\pi f_{low}} = 0.477 \quad [\text{m}] \ . \tag{5.9}$$

This radius is too large for many practical UAV purposes. Solving for 950 MHz results in an outer radius of 5.02 cm, which is a more suitable size for UAV mounting. Notice in equation (5.8) that the frequency is related to the radius of the spiral. This implies that a high-bandwidth pulse will be transmitted as a chirp, since each frequency component of the pulse is transmitted at different distances (i.e. different radii) from the feed point in the center of the antenna.

The combined bandwidth of the UWiBaSS radar system becomes 0.950-6 GHz when considering the limitations in both the radar sensor and the antennas. In table 5.2, the key parameters of the UWiBaSS system are

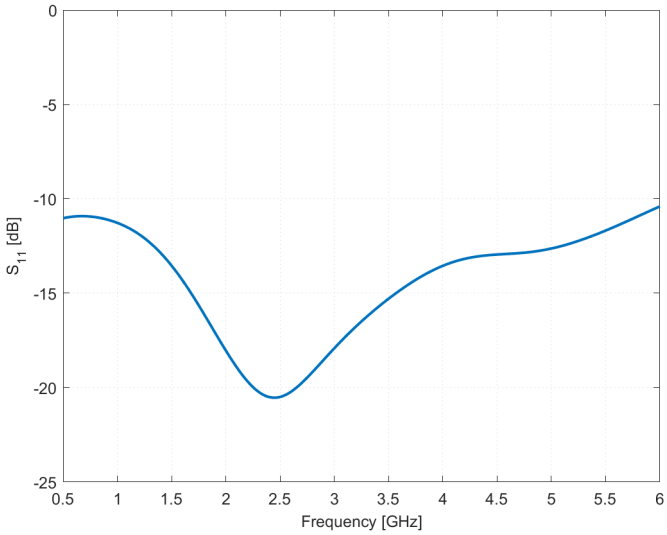

Figure 5.6: Simulated return loss (S_{11}) of Archimedean Spiral Antenna.

presented. Some parameters are calculated from equations (5.4 - 5.6) while others are gathered from the ILMsens m:explore datasheet [67] and from Sachs et al. [70]. Note that the measurement rate stated in table 5.1 is dependent on the capabilities of the control computer. The measurement rate has been calculated based on collected data from the radar system, and shows that the rate of measurement is highly dependent on a computer with high processing capabilities.

The range resolution stated in table 5.2 is in the ideal case with rectangular windowing. In any practical case, to avoid spectral leakage when performing Fourier domain processing, tapered windows are used (i.e. Band pass windows, e.g. Hanning or Hamming). Tapered windowing inherently decreases range resolution slightly. In section 5.5 we take a closer look at the range resolution of both radar systems used.

Table 5.2: UWiBaSS key characteristics

ILMsens sensor	**Value**
Signal generation	Pseudo noise
Bandwidth	5.9 GHz (0.1-6)
Range resolution (rectangular window)	2.252 cm
Equivalent sampling rate	13.312 GHz
Nominal output power	-7 dBm
Measurement rate	32 Hz (max 1000 Hz)
MLBS order	9 (511 values)
Unambiguous range in air	5.9 m
Unambiguous range in dry snow	5.0 m
Unambiguous range in wet snow	3.8 m
Average power consumption	8.1-9 W
Archimedes spiral antenna	**Value**
Bandwidth	10.05 GHz (0.95-11)
Efficiency	0.5
HPBW	70°
Combined Bandwidth	**5.05 GHz (0.95-6)**

5.4 Novelda Radar with Vivaldi Antennas

Another radar system we had at our disposal were the Novelda impulse radar sensor [77]. This system was fitted with Vivaldi antennas and a small UWB low noise RF amplifier at the RX stage.

Instead of pseudo-random noise, this radar relies on a traditional Gaussian pulse for excitation of the antennas. In the signal acquisition stage, a type of stroboscopic sampling is utilized [13]. Stroboscopic sampling means the radar receiver samples the back-scattered pulse after a given time offset. This offset represents the signal time-of-flight relative to the time of transmission, i.e. the number of range increments to the target. The Novelda radar has 512 range bins to where it can sample the incoming signal [77]. This leads to 512 "shells" in the direction of propagation from the radar antenna. These shells can be monitored individually or in combination depending on the systems intended application.

An improvement to the traditional stroboscopic sampling technique is the continuous time binary valued (CTBV) method of sampling. This uses a 1-bit quantizer at the receiving end that is then sampled by a sampling bank with individual time offsets (τ). This only yields a 1-bit resolution on our received signal dynamic range. To increase the dynamic range resolution

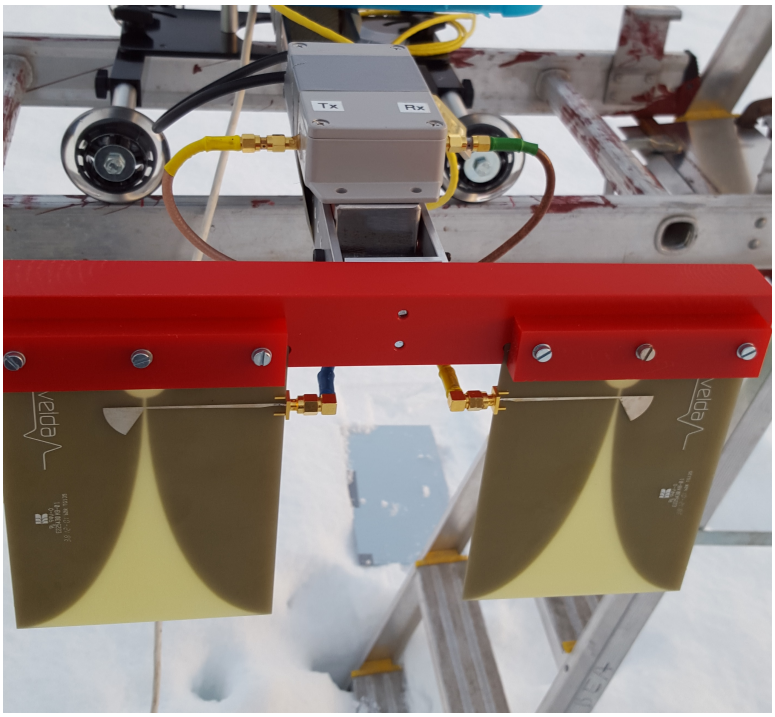

Figure 5.7: Novelda Radar (top) with Vivaldi antennas mounted on custom made nylon fasteners.

a Swept Threshold Sampling technique is also applied. We still use a single quantizer, but the sampling procedure repeats while we sweep the threshold over the range of interest. For each threshold step, the conversion results accumulate in a digital counter. After the completed sweep, the counter indicates the converted value which indicates the amplitude of that sample. Then it moves systematically through the range bins to get the corresponding distance of the sampled signal amplitude.

In Figure 5.9 we can see how the quantizer works with swept threshold sampling. It is somewhat similar to direct analog-to-digital conversion, but it does not use comparator banks working in parallel. Instead, it uses a single quantizer with a sweeping threshold. A more comprehensive study of stroboscopic sampling and swept threshold sampling is presented in Hjortland [78].

Simple pulse radar systems operating at a constant PRF have a maximum unambiguous range based on the transmission time from one pulse to the next. If the transmitted pulse is very short compared to the pulse repetition time, the maximum unambiguous range for pulse radars can be expressed as [13]:

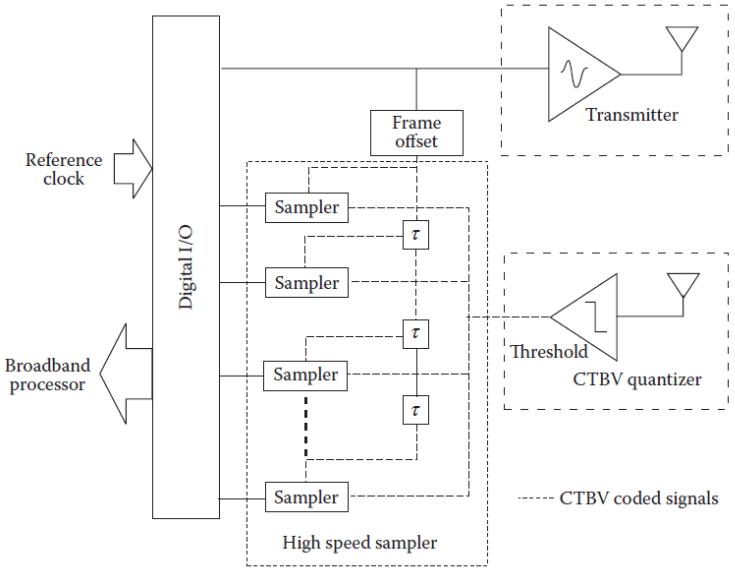

Figure 5.8: Novelda Radar CTBV signal acquisition system. Reprint from [13]

$$R_0 = \frac{c}{2\text{PRF}} \ . \tag{5.10}$$

The maximum PRF of the Novelda radar is 100 MHz yielding a maximum unambiguous range of 1.5 m. The Novelda radar expands this range by using a staggered PRF effectively increasing the maximum unambiguous range. This introduces a certain amount of randomness to the pulse transmission interval, where reflections will appear at slightly different time intervals relative to the most recently transmitted pulse. Because of the range increment averaging (512 increments) of the receiver, these uncorrelated pulses will cancel out instead of appearing as ghost reflections [13]. The staggered PRF enables the 512 range bins to, in principle, be moved to any range of interest.

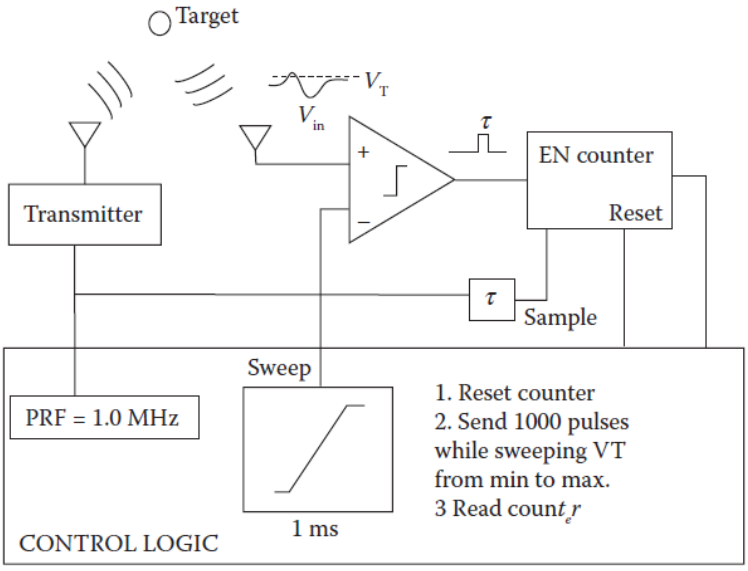

Figure 5.9: Swept Threshold Sampling functional diagram. Reprint from [13].

5.4.1 Vivaldi Antenna

Vivaldi antennas are planar, broadband antennas. The main differences compared to spiral antennas are the HPBW ($\approx 20°$), less impedance stability over a large frequency band (i.e. return loss S_{11}) and linear polarization. Additionally, when considering the physical shape of the antenna it is evident that these antennas are more prone to vibrational effects from wind and internal vibration in whatever system they are mounted on. Therefore, careful design of the fastening platform is needed (see Figure 5.7).

As previously stated, the return loss for this antenna type, shown in Figure 5.6, is not as constant and low as for the Archimedes spiral antenna. This in combination with pulse excitation from the Novelda radar gives a more variable return loss (scattering matrix element S_{11}) than the UWiBaSS system.

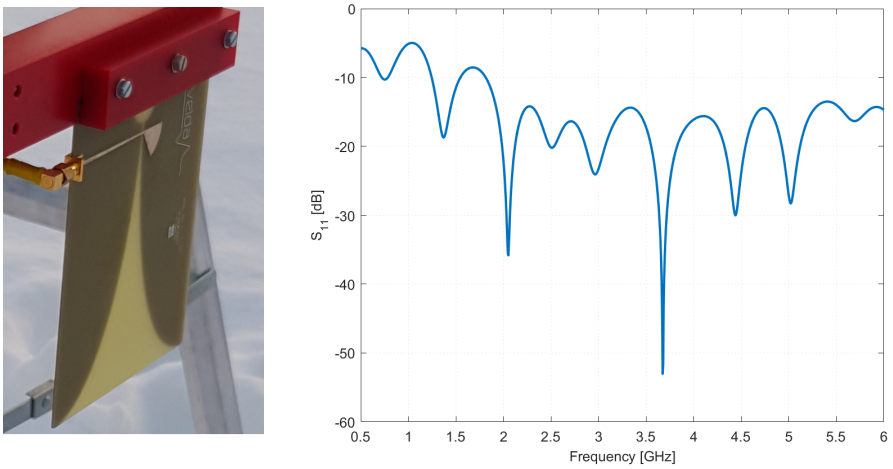

(a) (b)

Figure 5.10: Vivaldi antenna (a) and simulated return loss (S_{11}) (b).

Table 5.3: Novelda radar key characteristics collected from [13] and [77]

Novelda sensor parameter	**Value**
Signal generation	1^{st} order Gaussian
Bandwidth	0.85 - 9.6 GHz
Range resolution (rectangular window)	4 mm
Equivalent sampling rate	39 GHz
Nominal output power	-19 dBm
Maximum PRF	100 MHz
Depth perception	512 depth levels
Unambiguous range	60 m
Power consumption (Max utilization)	113 mW
Vivaldi antenna parameter	**Value**
Bandwidth	4.1 GHz (0.9 - 5 GHz)
HPBW	20° E-plane, 50° H-plane
Combined bandwidth	**4.1 GHz**

5.5 Case Study: Range Resolution Measurements

We performed a simple test to check the actual range resolution of the radar systems. In this test, we scanned a perfect electrical conductor (PEC) plate to get a pulse as clean as possible to analyze. We characterize the range resolution as the full width at half maximum (FWHM) distance in terms of power. Thus, in this case, the rectified pulse is analyzed in terms of power, not voltage as in the remaining thesis.

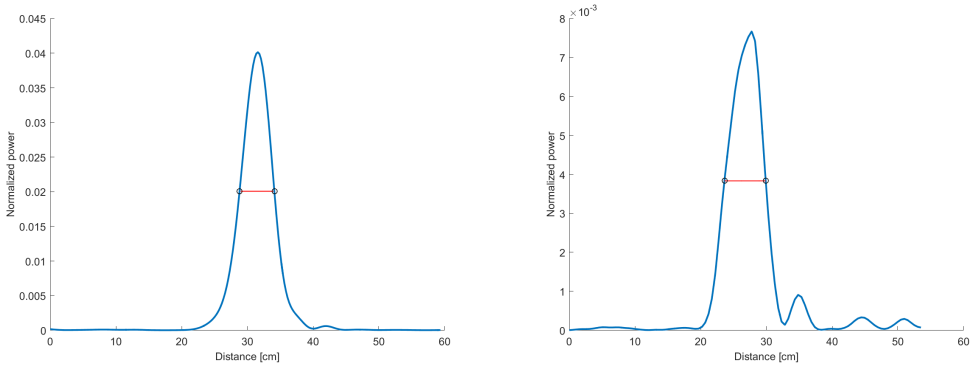

(a) FWHM = 5.3 cm (b) FWHM = 6.3 cm

Figure 5.11: PEC plate pulse returns and FWHM (red line) of the UWiBaSS system (a) and Novelda radar (with Vivaldi antennas)(b). This width effectively becomes the range resolution of the radar systems.

The resolution might be slightly improved by additional fine-tuning of the windows to match the radar system bandwidth. Nonetheless, the resolution will be reduced compared to the ideal case presented in the radar sensor data-sheets.

5.6 Radar System Comparison

To summarize, we have a comparison of the two systems in table 5.4. This comparison is based on what is desired for this project (i.e. what works best for UAV snow measurements).

It is important to note that the detection range of any radar system depends on both unambiguous range and the radar equation (see equation

Table 5.4: Performance comparison between radar sensors with mounted antennas

Pros/cons	ILMsens radar with spiral antennas (UWiBaSS)
+	Higher bandwidth (5.05 GHz)
+	Higher output power (-7 dBm)
+	Pseudo noise = stable power
+	Range resolution (tapered window) = 5.3 cm
−	Relatively large in size
−	Large beamwidth (approx. 70°)
−	Unambiguous range = 5.9 m
−	Power consumption = 8.1-9 W
	Novelda radar with Vivaldi antennas
+	Small form factor
+	Narrow beamwidth (approx. 20°)
+	USB powered
+	Easy to operate
+	Unambiguous range = 60 m
+	Power consumption = 113 mW
−	Lower bandwidth (4.1 Ghz)
−	Lower output power (-19 dBm)
−	Range resolution (tapered window) = 6.3 cm
−	More noise due to pulse excitation

3.4), where the maximum range depends on transmitted power and received power among other factors. In other words, the beamwidth of the antennas and transmitted power influence the received power.

5.7 Safety Aspects

If these radar systems are to be commercially used in the future, one should consider the safety aspects of human exposure to ultra wideband radar fields. According to Cavagnaro, Pisa, and Pittella [79]: "a UWB radar that satisfies the FCC mask emits an electromagnetic field whose maximum value is well below the maximum value settled by the safety guidelines." According to the defined specifications of the radar sensors, this requirement is to some extent full-filled. However, more extensive testing should be performed to investigate further if the specific absorption rate is within the defined safety guidelines. Since the general UWB radar emits non-ionizing electromagnetic waves in the band 3.1-10.6 GHz, the main effect that this wave can cause in

the human body is power absorption creating heat [79].

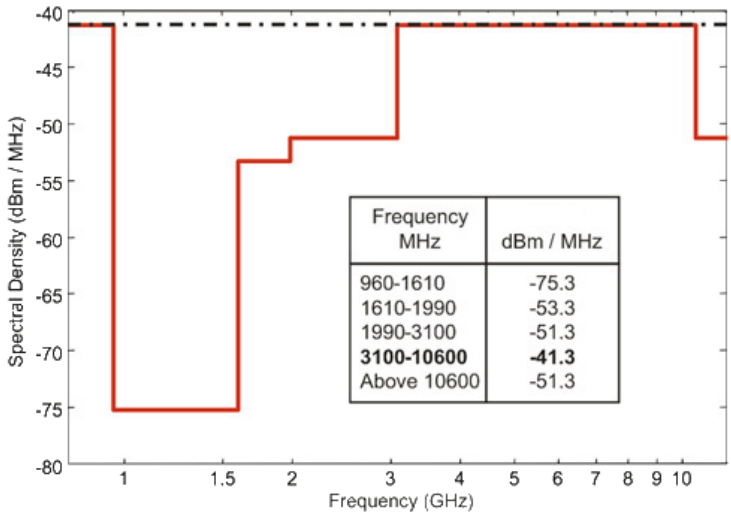

Figure 5.12: FCC UWB mask

As we can see in Figure 5.12, the maximum radiated field is defined as -41.3 dBm/MHz. This mask is defined well below the safety guidelines of UWB radiation, and is intended as a restriction regarding interference with other communication-systems. The interested reader can note that the 960-1610 MHz band is allocated for GPS communication, which operate at 1.22 and 1.57 GHz with a 1.023 MHz band for each frequency.

Also, note that Figure 5.12 show the American regulations. The European mask (ETSI EN 302 066-1, 2007) is more restrictive (especially above 6 GHz) for mean power spectral density.

5.8 Radar Measurement Platform

To obtain measurements above the snowpack, considerations regarding stability and functionality needed to be taken into account. The intended purpose of the platform was to facilitate non-invasive, above ground, measurements where the radar could be moved continuously to simulate UAV flight. Four main requirements were defined in the process to find the best solution for this particular task:

- The radar system should be situated approximately 1 m above the snow surface.
- The applied radar had to be able to move, but limited to one direction (Azimuth).
- The platform had to be somewhat stable so that wind gusts would make little impact on the radar measurements.
- The platform had to be built with easily obtainable parts.

To allow the radar to move continuously and controlled in a single direction a camera-dolly (mostly used in film production to allow cameras to move smoothly) specially made to roll on aluminum ladders were chosen. This dolly type was chosen for its adaptability to different rails and ladders so that a custom rail system did not have to be ordered. This proved to save both time and funds and yielded a smooth, controlled, continuous data acquisition platform. Step ladders were used as "feet" for the rig, with screw-clamps to hold the suspended ladder between them. This assembly functioned very well for its task and was easily moved to different locations if necessary. The constructed platform also proved to be very stable. The total measurement scan length became effectively the length of the ladder chosen. The ladder used was approximately 4.3 m and provided a measurement length of 4.2 m due to the fastening at the end, and the length of the dolly.

To facilitate the use of both the UWiBaSS and Novelda sensors, the dolly was fitted with a 2 m aluminum beam with each radar sensor at each end. This allowed quick switching between the systems as the dolly only needed to be lifted and rotated 180° to measure on the exact same snowpack. Both systems were controlled with a laptop mounted at the center of the dolly. The total measurement time with both systems was approximately 10 minutes. To maintain constant speed across the transect, 10 cm increments was marked along the ladder. This, in combination with a stopwatch allowed us to move

the dolly with adequately accurate speed. The approach was to define a set time it should take to move 10 cm (e.g. 10 sec/10 cm = 0.01 m/s). Even if the speed within each 10 cm step was not constant, at each new 10 cm step we should know what time the stopwatch should be at and could speed up or slow down based on that. The drawback of this method is that high speeds are harder to control, and made testing of maximal scanning speed difficult.

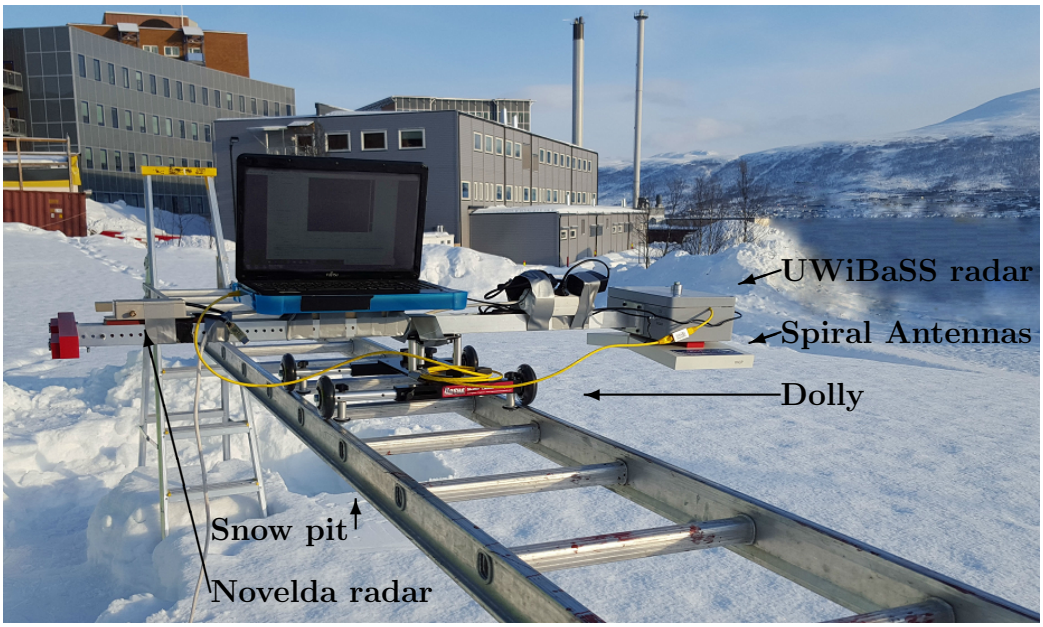

(a)

(b)

Figure 5.13: Radar measurement platform (b) with mounted radar systems and PC to log data (a).

Chapter 6

In situ Measurement Methods

During the measurement campaign, several different *in situ* parameters were collected from the snowpack. In this chapter, we will go through the methods used to measure snow density, liquid water content, stratigraphy, depth and relative permittivity.

Among these, density is an important parameter when considering dry snow. The density allows us to approximate the real part of the relative permittivity of snow, which in turn can give us several important RF parameters of the snow [41]. To account for the changing pulse velocity through the snowpack, accurate density measures for all layers need to be taken. This can be done by several methods, as discussed below.

6.1 Density Cutters

One of the most intuitive methods for measuring density is using density cutters. This method involves taking a volumetric sample of the snow, where density is calculated by weighing the defined snow volume which is extracted from the snow using a cylinder-, wedge-, or box-type cutter. In [80] the different types of density cutters are compared in regards to accuracy and vertical resolution. The major drawback of density cutters is the destructive measurement method and the vertical resolution. During this project, the wedge type density cutter was used as a control measurement for the Toikka Snow Fork [43]. The wedge type density cutter takes out a sample of approximately $10 \times 10 \times 20$ cm (see Figure 6.1c) from the snowpack, thus high-resolution measurements down the snowpack are difficult to perform.

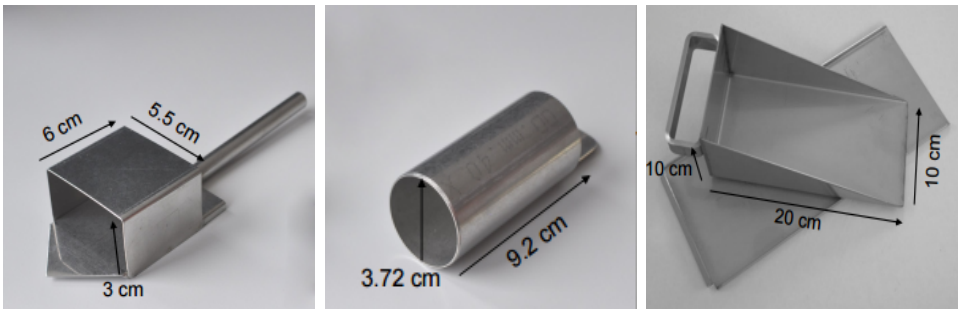

(a) (b) (c)

Figure 6.1: Types of density cutters: (a) box, (b) cylinder, and (c) wedge. Reproduced from [80].

6.2 Radio-Wave Resonators

Using instruments that can measure the resonant frequency of a medium one can calculate the relative permittivity of the same medium [43]. There are several methods to perform these measurements, where some are more destructive to the snowpack than others. In Denoth et al. [81], Denoth and Foglar [82] and Kinar and Pomeroy [83] several resonant sensors are compared (including the Snow fork and Denoth capacitive sensor mentioned here), and show that discrepancies between the sensors are approximately 1%. However, the Snow fork and Denoth capacitive sensor produce nearly non-destructive measurements compared to other relevant instruments. This is desirable as the same snow pit can be used several times. In Williams [84] it is shown that there is no statistically significant difference between measurements from the Denoth meter and the Finnish snow fork. The Snow fork was chosen as it was the only obtainable instrument of the two.

These instruments are also capable of measuring the liquid water content of snow. In Techel and Pielmeier [85], the Denoth meter and Snow Fork is compared to the traditional "hand test" (i.e. hand squeezing) to classify wetness where it is concluded that the "hand test" is not a reliable method of measuring the wetness of snow. Koch et al. [86] propose a wetness measurement approach based on the attenuation of microwave radiation emitted by GPS systems. This method is yet to be manifested in a commercial product, but might prove useful in future measurement campaigns.

6.2.1 The Denoth Capacitive Sensor

The Denoth capacitive sensor was developed at the University of Innsbruck. This instrument is also known as a Denoth meter and consists of a flat

plate antenna that is inserted into the snowpack [87], [82]. The area of measurement has been estimated to 176 cm^2 from a 13×13 cm (169 cm^2) plate antenna, due to the fringing fields at the plate edges.

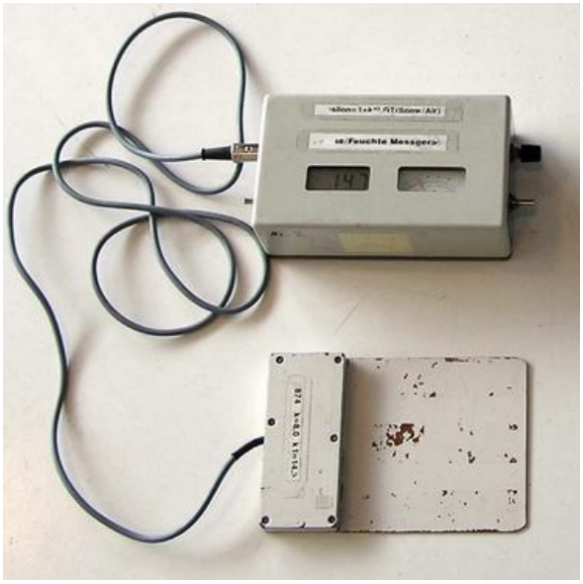

Figure 6.2: Denoth meter. Reproduced from [85].

The real part of the relative permittivity can be found by [81]:

$$\epsilon_r^{'} = 1 - \alpha \Delta c \ , \tag{6.1}$$

where Δc is the difference in detected capacitance in air and snow, and α is the attenuation constant of the medium.

This sensor can also measure the imaginary part of the relative permittivity, however, it is not covered in [81]. It most likely utilizes a similar method as The Snow Fork described below, measuring the loss tangent based on the Q-factor of the resonant frequency.

6.2.2 The Snow Fork

The Snow Fork is a radio-wave sensor for determining the density and wetness profiles of a snow pack with a single measurement. The snow fork is based on the measurement of the dielectric properties (real and imaginary part) of snow around 1 GHz [43]. From these measurements we can estimate the density and liquid water content of the snow based on the relation derived in Sihvola and Tiuri [43] and Tiuri et al. [41].

The snow sensor developed at the Radio Laboratory, Helsinki University of Technology, consists of a resonator that can be pushed into snow or any other porous, granular, or liquid material that is to be measured. Measurement of dielectric properties is achieved by measuring the change in the resonance curve when pushing the resonator into the snow. The sensitive parameters are resonant frequency and bandwidth quality factor (Q-factor). From these measurements, the relative permittivity is calculated. The real part of the relative permittivity can be calculated by [43]:

$$\epsilon_r^{'} = \left(\frac{f_a}{f_s}\right)^2 \ , \tag{6.2}$$

where $\epsilon_s^{'}$ is the real part of the relative permittivity, f_a is the resonant frequency in air (i.e. the reference frequency) and f_s is the resonant frequency measured in the snowpack.

The imaginary part of the relative permittivity can be found by measuring the loss tangent:

$$\frac{\epsilon_r^{''}}{\epsilon_r^{'}} = \tan\delta \ , \tag{6.3}$$

where $\epsilon_r^{''}$ is the imaginary part of the relative permittivity and $\tan\delta$ is the loss tangent. The loss tangent can be found via the Q-factor. If we denote the 3 dB bandwidth of the resonant frequency in the snow as Δf_s and Δf_ϵ as the 3 dB bandwidth of the resonant frequency with the resonator in a loss-less material with the same real part of the permittivity as the snow, we have:

$$\frac{\epsilon_r^{''}}{\epsilon_r^{'}} = \frac{\Delta f_s - \Delta f_\epsilon}{f_s} \ . \tag{6.4}$$

The measurements involve pushing the sensor inside the snow at each visible layer, or at a finite set of increments down the snowpack. Then density and liquid water content can be read directly form the instruments display. The Snow Fork averages over a cylindrical volume that is orthogonal to the layer protruded, and whose center of sensitivity is 6 cm inside the surface of the protruded layer.

During this project, a Snow Fork sensor was borrowed from The Norwegian Polar Institute. The measurements were performed in the same snow pit as the other *in situ* measurements took place. That is, at the start of the transect the radar passed over. At each measurement point in the snowpack, three measurements where taken and averaged. The resulting density curves showed that the snow had a generally increasing density from top to

Figure 6.3: Toikka Snow fork at snow pit 29.03.16.

bottom. The density measurements where verified with box cutter density measurements at the center of the snowpack. The picture in Figure 6.3 is from the last day of measurements where the snowpack had melted down from a maximum thickness of 90 cm to about 35 cm.

6.3 Snow Stratigraphy Measurements

The stratigraphy (i.e. profile) of a snowpack can be quantified in several different ways. A common method is a manual measurement by digging a snow pit and identifying the different layers visually. The depth of each layer is measured and each layer gets a hardness classification based on the amount of force required to penetrate into each layer. This hardness scale is far from scientific and is classified by what object that can penetrate the snow [3]. A typical example of this type of hardness classification is presented in table 6.1.

A different method of measuring snow stratigraphy is by using a penetrometer. The snow penetrometer can characterize the snowpack far better than traditional hand hardness methods where thin layers often go undetected, which are highly relevant to avalanche formation [4]. The snow penetrometer apparatus with data acquisition hardware measures the force re-

Table 6.1: Snow hardness estimation [3]

Penetration resistance	**Estimated Hardness**
Fist	Very Soft
Four Fingers (Tips)	Soft
One Finger (Tip)	Medium
Pencil Point	Hard
Knife	Very Hard
	Ice

quired to push a small dimension tip member into a snow surface at constant speed. In Lutz and Marshall [88] the AvaTech Snow penetrometer prototype (SP1) is tested versus classical methods of determining snow stratigraphy, where the accuracy could at times be as low as 5-10 cm. During this project, the commercial version AvaTech SP2[1] was used. This sensor measures the force required to penetrate each layer through the snowpack in kPa. In Hagenmuller, Pilloix, and Lejeune [89] the RMS error of total depth measurements with the AvaTech SP2 was found to be 7.5 cm. This needs to be taken into account when comparing the snow probe and radar stratigraphies as the general shape of the *in situ* stratigraphy might be correct, but the overall depth might have deviations. However, we have no other *in situ* stratigraphic measurement tool available and will, therefore, correlate our measurements with the stratigraphy from the Avatech SP2 probe. Additionally, manual snow depth measurements were performed as a control measurement to counteract the total depth error of the Avatech SP2 probe.

Stratigraphy measurements were performed by plunging the probe vertically down the snowpack. The probe measures the penetration resistance over time with the tip force sensor. Depth is calculated by combining the signals of an infrared sensor, an optical sensor, and the tip force sensor. The infrared sensor, located at the top of the probe facing the snow surface compute the distance to the surface. The optical sensor, located at the bottom of the probe, and the force sensor detect whether the tip has entered the snowpack and their outputs are used to scale the measured depth.

[1]Visit the AvaTech web page at www.avatech.com

Figure 6.4: AvaTech SP2 snow penetrometer. Reprint from the AvaTech web page.

Part III

Results

Chapter 7

A-scan Processing

Raw radar data is usually hard to read by visual inspection. As the radar systems in question have not been extensively tested before, some considerations regarding creating trustworthy data were taken into account. In these measurements, two references were used as it was important to determine the air-snow interface and to confirm calculated distances within the radar maximum range. The most common reference point was the setting of zero time at the start of the antennas. This is done by localizing the crosstalk between the antennas and setting the start of the crosstalk as zero (see chapter 4). Additionally, a PEC plate was placed on top of the snowpack at the start of the transect (see Figure 7.1), thus giving a good measure as to where the air-snow interface was in the vertical direction. This additional reference was used to avoid errors in depth measurements due to the powder-like top layer of the snow as it was expected that this snow type would give low reflections. This proved very useful when determining the start of the snow in the radar image. In the following sections, we will look at the results from the data processing methods. We will take a UWiBaSS radar measurement from 11.03.16 as our case study dataset. Later, we will look at results from the Novelda radar as well as results from different days of measurement.

The processing of this data can be time-consuming. After extensive code optimization, it will still take approximately 10 minutes to process a full scan of the snowpack at maximum resolution. This is simply due to the sheer size of the recorded data which can contain several million data-points. However, for quick analysis, a low-resolution image can be processed in approximately 1 minute.

Figure 7.2 show the basic processing steps, where each step involves several methods described in chapter 4. Depending on the application, the final step could be to only classify layer transitions if no *in situ* measurements are available.

The first stage of processing involves shifting the signals such that zero

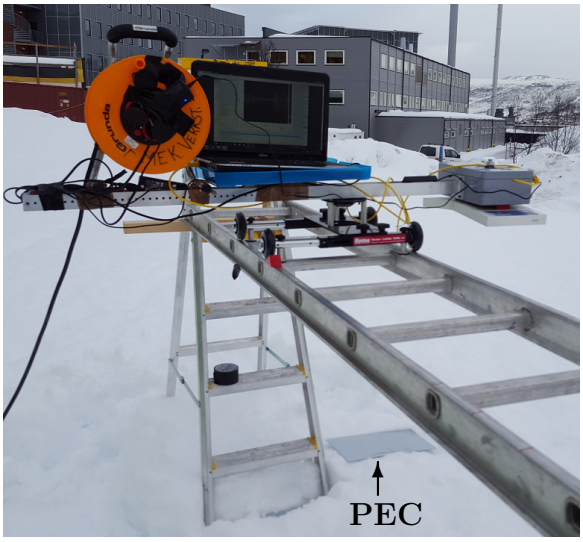

Figure 7.1: Photo of PEC plate placed below the radar acquisition platform.

time is at the antennas. The resulting image is a raw radar image with zero time at the correct location. In Figure 7.4a we can see the PEC plate (to the left in the middle) and a considerable amount of crosstalk and clutter. After subtracting the free space reference signal, the phase response is modeled according to section 4.2.4 and adjusted by subtracting the non-linear term c/f (see equation (4.4)). In Figure 7.3 the non-linear term of the phase response is modeled and adjusted.

As we can see in Figure 7.4b the PEC plate and soil below (at ≈ 80 cm) is visible. This allowed us to set a zero point at the start of the PEC reflection, giving an accurate measure of snow depth down towards the soil. At this point the data is somewhat processed: the zero-time point has been set, the free space reference has been subtracted, the pulses have been rectified with a Hilbert envelope set to output voltage, the non-linear phase of the antennas and relative phase velocity for different layers have both been compensated for. These methods are covered in section 4.2. The resulting image is an accurate representation of the returned data from the radar system. We now have an image ready for further signal processing.

In the next section, we will look at some methods to further improve the response with image processing methods and data mining with the constructed B-scan. Some of the methods described will not produce significant improvements to these images but should be mentioned as they might prove useful at a later stage in this project.

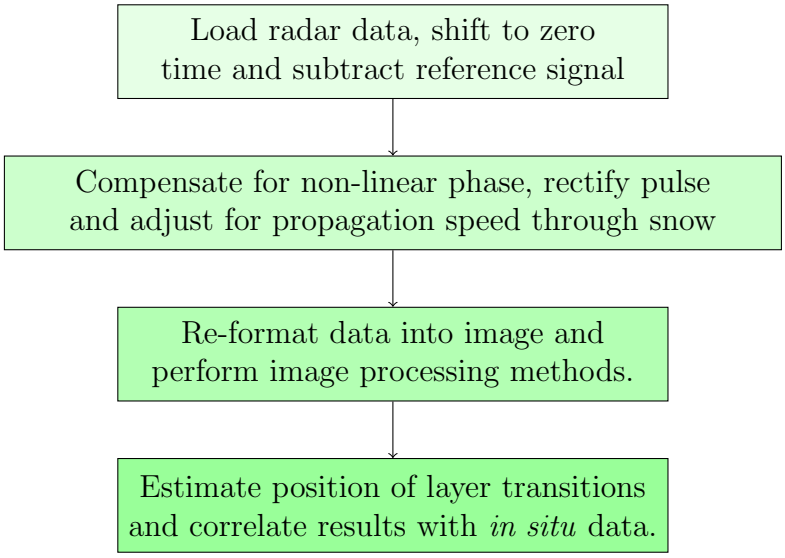

Figure 7.2: Data processing flow chart

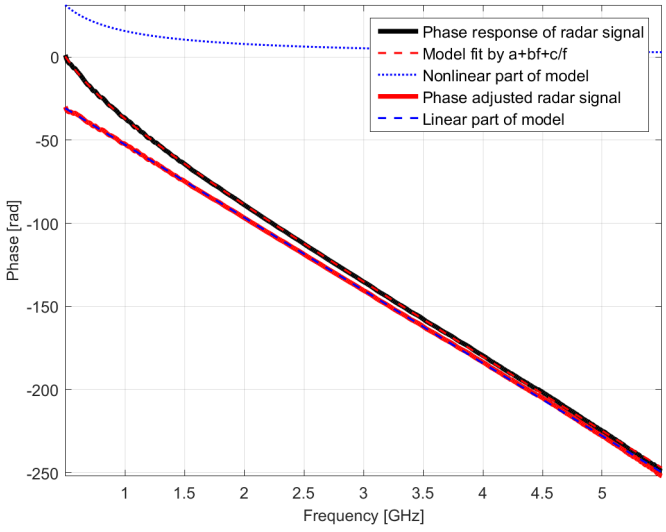

Figure 7.3: Non-linear phase response model of the radar system due to Archimedean antenna dispersion.

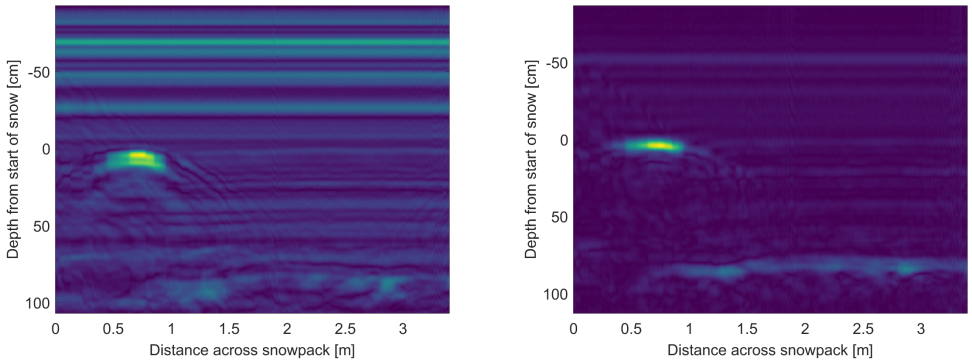

(a) Raw radar image (b) After A-scan processing

Figure 7.4: Radar image of PEC plate and ground.

Chapter 8

B-scan Processing

8.1 Histogram Equalization

Looking at the histogram (i.e. pixel intensity distribution) of the image in Figure 7.4b it is evident that the pixel intensities are not evenly distributed (see Figure 8.1a). Now utilizing histogram equalization, we can spread out the intensity distribution so that details in the image become more distinct.

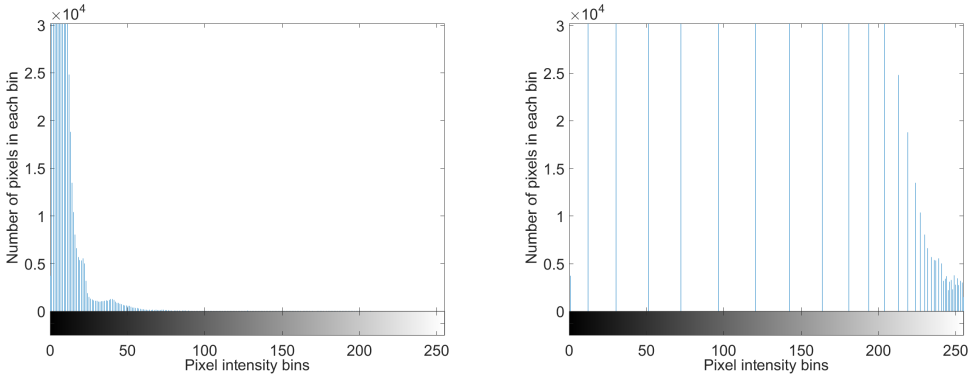

(a) (b)

Figure 8.1: Histogram before (a) and after (b) histogram equalization.

Looking at Figure 8.2 it is apparent that a lot more information is visible to the human eye. Notice the hyperbolic shape of the reflection from the PEC plate. This is an expected diffraction effect as explained in section 4.4.

From now on we will look at the radar image where the PEC plate have been cropped out to better visualize the layers in the snow.

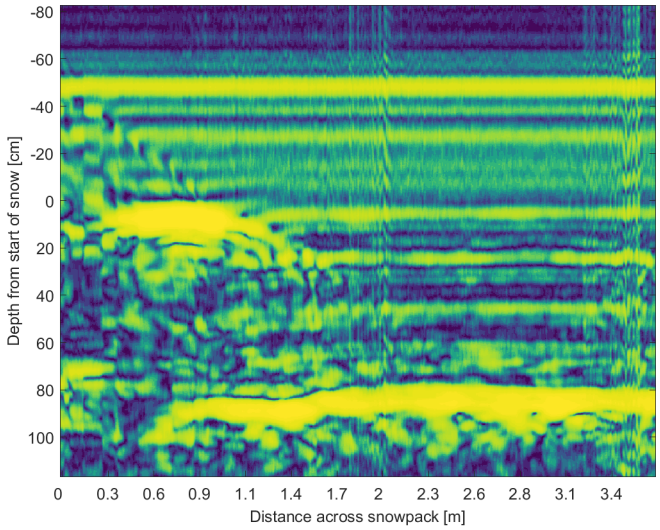

Figure 8.2: Figure 7.4b after histogram equalization.

8.2 Interference Removal with SVD

In Figure 8.3a, there are signs of vibrational interference (marked with red rectangles). This type of noise only occurred on a single day of measurement (11.03.16) and was due to excessive wind that caused the acquisition platform to slightly sway while scanning. This interference gives us the opportunity to test eigen image filtering by SVD which might be a useful processing method in situations where vibration is inherent in the system (e.g. UAV operations).

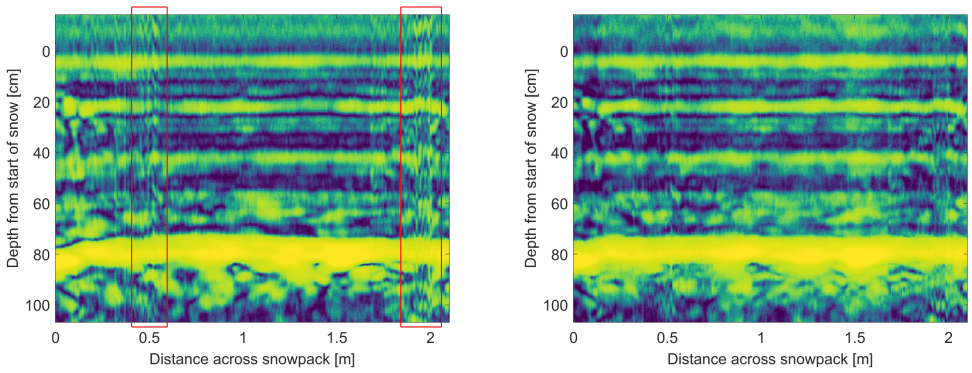

Figure 8.3: Cropped radar image with vibrational interference (a) and filtered image using eigen image filtering by SVD (b).

Looking at Figure 8.3b, we see that the interference is significantly reduced. However, some details in the image are also lost. For instance, the ground layer has lost some of its contours. When selecting a specific set of eigen images to represent the image, we will lose information from the image, which might not only be unwanted information. In this case, the bandpass version of the SVD method was used.

8.3 Layer Detection with Hough Transform

It might prove useful to quantify the layers in the snowpack. This can be done by looking for horizontal lines in the image with the Hough transform. Here, thresholding is necessary to select the features of interest. Specifically, a threshold for maximal angle (i.e. we only want lines close to horizontal) and a neighborhood threshold to avoid multiple detections of essentially the same layer. The angle threshold was set to $\pm 10°$ deviation from a horizontal line ($\pm 90°$). The algorithm was also limited to only perform layer detection within the snowpack defined by the PEC plates.

In Figure 8.4a the x and y axis represent the angle and position of the lines respectively. Here the position is denoted in pixels, not distance or depth.

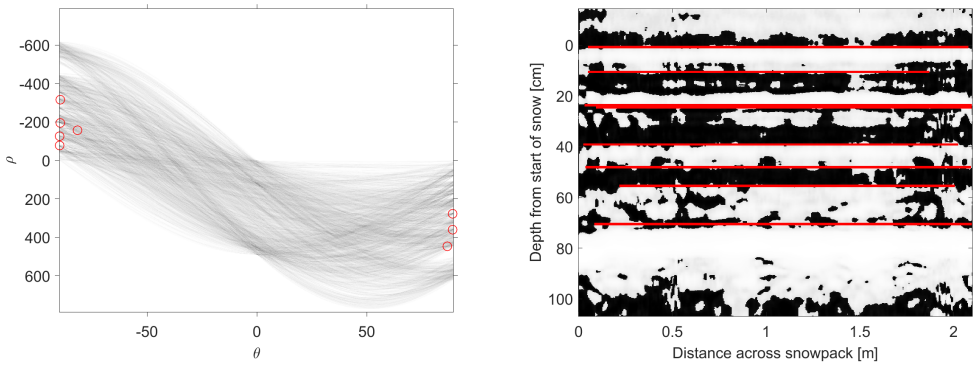

(a) (b)

Figure 8.4: Hough space of radar image (a) (detected lines marked with red circles) and radar image with red Hough lines (b).

Chapter 9

Correlation with *In Situ* Measurements

With the processing stage done, we can now investigate the correlation between the *in situ* and radar measurements. Some important factors regarding the *in situ* measurements are worth noting first. The main device used to measure *in situ* snow stratigraphy is the AvaTech SP2 snow probe. This is a penetrometer designed to detect snow stratigraphy based on the pressure required to penetrate each layer. The measurement is performed by thrusting the probe vertically through the snow all the way down to the soil. This gives a reading of the amount of kPa required to penetrate each layer, thus giving a measure of the stratigraphic force resistance within the snowpack. Hence, this is a point measurement system (i.e. one dimensional) whereas the radar system scans a transect (i.e. two dimensional). The radar image is therefore averaged to a vector, which enables us to correlate the measurements. The radar image can be segmented to only average over the start of the transect where the *in situ* measurements took place.

More importantly, we should note that the dielectric (radar response) and mechanical (probe response) properties of snow are related in an unknown way [16]. It is therefore not straightforward to correlate these measurements. However, snow hardness is somewhat related to the density [17], thus we might be able to find transitions in the radar image that correlate with a change in snow hardness.

To better compare the two measurements, the radar signal and stratigraphic profile obtained by the snow probe are normalized (i.e. both curves integrates to 1). This is only for visual purposes as the profiles now have similar amplitudes. The averaged, normalized radar response in Figure 9.2 can be considered as a PDF for the occurrence of a dense layer in the snowpack along the transect.

Using the Snow Fork density measurements, we can calculate the pulse

propagation velocity through the snow [41] (shown in Figure 9.2). If the snow contains a significant amount of liquid water, then we also have to include that as a factor in the model (see section 4.2.6). However, in the presented measurements in this chapter, the snow had no measurable amount of liquid water.

In Figure 9.1 we have the collected data from the snow fork, and the calculated relative permittivity. Note that the resonant frequency of the snow fork in air is 844 MHz with a 3 dB bandwidth of approximately 5 MHz [43], which changes as we go down the snowpack. This information is what we use to calculate density, permittivity and eventually pulse propagation velocity shown in Figure 9.2.

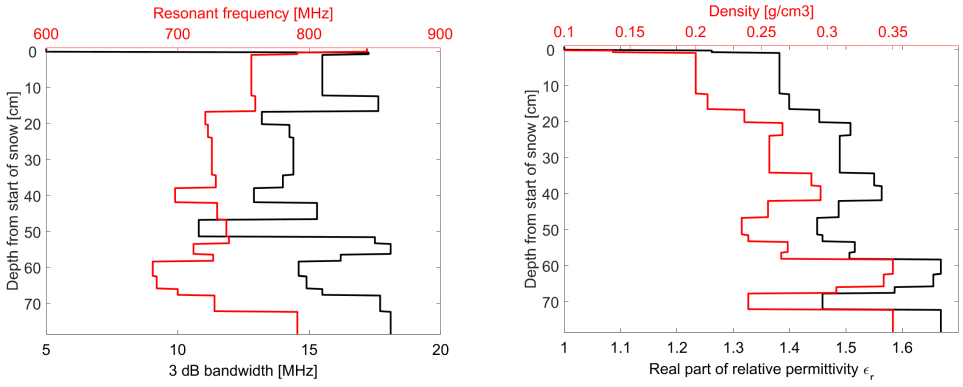

(a) (b)

Figure 9.1: *In situ* measurements with snow fork showing resonant frequency and bandwidth (a) and the corresponding calculated values for density and relative permittivity (b).

Looking at the main features of each curve in Figure 9.2, there are some apparent similarities. The first two hard layers seem to correlate well. Going deeper down the snowpack, the main features are still similar, but with a small offset in depth. The amplitude of the radar signal compared to the *in situ* measurement is one of the features that is difficult to compare given the unknown relationship between mechanical and dielectric properties of snow.

Now, consider only looking at peaks and valleys of the two stratigraphies in Figure 9.2 and classify them as dense or porous layers. These points become transition points between different densities (or hardness). Here we define peaks and valleys based on several criteria: Amplitude, width, separation from other peaks and prominence. The prominence of a peak measures how much the peak stands out due to its intrinsic height and its location relative to other peaks. This means that a low isolated peak might

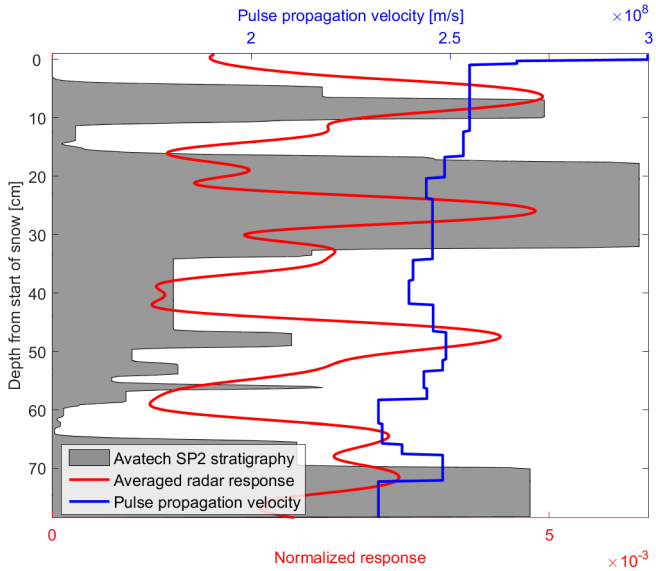

Figure 9.2: Snow stratigraphy comparison between *in situ* measurements performed with the Avatech SP2 snow probe and the averaged radar response of the same snowpack measured with the UWiBaSS system. The pulse velocity is plotted in blue. These measurements were taken 11.03.16.

be more prominent than a high peak in the vicinity of a large range of peaks. Finally, we choose to classify the most prominent peaks for each class (porous and dense). The points at the wide, flat peaks in the Avatech SP2 stratigraphy are centered to represent the center of the layer. We could choose more or fewer peaks, but the stratigraphy in Figure 9.2 seems to have about 7 major layer transitions. In Figure 9.3, the most prominent peaks and valleys are labeled. This method gives a quite crude representation of the snow stratigraphy, but it reduces the complexity of the measurements down to just a couple of points that might be sufficient to analyze the snowpack.

In Figure 9.4 we compare the depth of transitions measured with the Avanet SP2 probe and the UWiBaSS radar system from two different days of measurement.. Each transition in the radar scan is classified as a dense or porous layer and the closest transition of the same class in the *in situ* stratigraphy is connected to form the plot in Figure 9.4. Note that there are 10 detected transitions from 24.02.16, as the snowpack had several more layers than the snowpack from 11.03.16. The correlation between the transitions in Figure 9.4 is listed in table 9.1

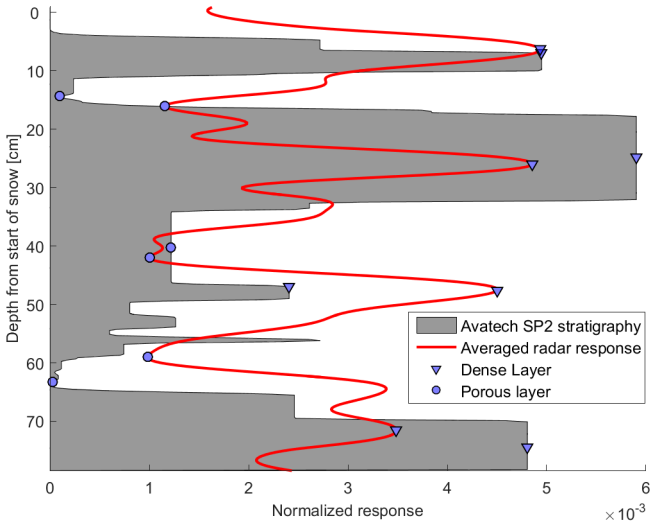

Figure 9.3: *In situ* error measure where dense and porous layers are classified and labeled. From 11.03.16.

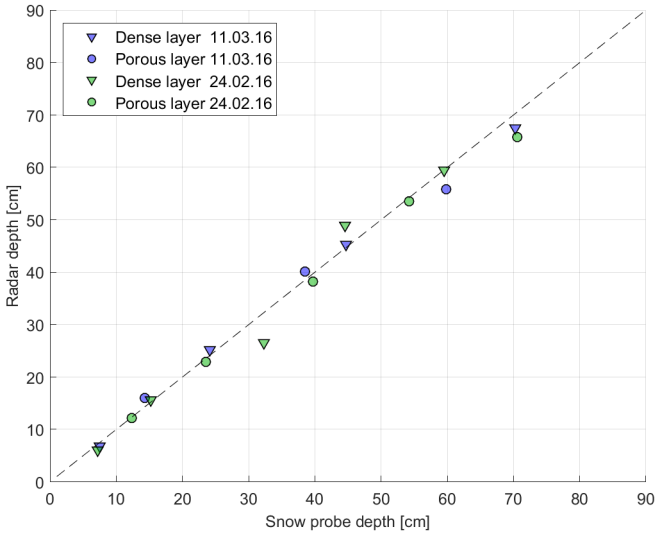

Figure 9.4: Comparison of transition depths from radar and snow probe measurements. The presented data is from two different days during the measurement campaign. From each day, transitions were classified as either porous or dense.

Table 9.1: Correlation between UWiBaSS radar and *in situ* measurements for two different days of measurement. Pearson correlation coefficient calculated with 3σ confidence interval.

Date	**Correlation coefficient**	**RMS error**
11.03.16	0.97 ± 0.03	2.11 cm
24.02.16	0.96 ± 0.04	2.84 cm
Average	0.97 ± 0.04	2.48 cm

Chapter 10

Complementary Results

The results in the previous chapter arise from measurements performed on a single day (11.03.16), except for the transition depth comparison in Figure 9.4 and table 9.1 that included measurements from 24.02.16. In the next sections, we will look at other results from this project including radar system comparison, measurements on wet snow, target detection tests, and initial UAV flight tests.

10.1 Dry Snowpack 24.02.16

The data collected on 24.02.16 underlined one important point regarding the *in situ* measurements. That is, the snow probe only measures the stratigraphy at a single point whereas the radar is scanning a transect. Consider Figure 10.1, the red square marks the area where the *in situ* stratigraphy was taken. Note that the prominent layer at a depth of approximately 30 cm does not properly start until 80 cm into the transect.

The contribution of this artifact become clear when we compare the averaged radar image and the snow probe stratigraphy in Figure 10.2. In Figure 10.2a we can see that most detected layers correlate to some degree, however, we have a strong reflection at approximately 30 cm which seems to be an error. Regarding the first reflection at approximately 5 cm; we expect to get a large reflection at the transition from air to snow, no matter the mechanical resistance measured with the snow probe.

If we instead segment the first 50 cm of the transect and average that, we get a result with better correlation as can be seen in Figure 10.2b. It is important to discuss how to best measure snow stratigraphy and how the measurement should be processed and represented. In our case, the ground was relatively flat and the snow depth was to be considered constant along the transect. Therefore, an averaging of the entire transect might be a correct

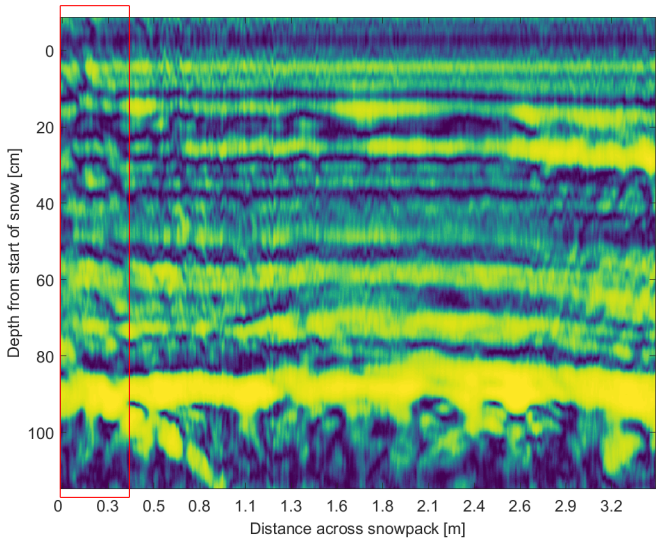

Figure 10.1: UWiBaSS B-scan image from 24.02.16

way to approximate the stratigraphy. However, the snow tends to lay flat on top of uneven soil as well and an averaging of a long transect would, in that case, give an inaccurate measurement. Therefore, it is important to gain information about the shape of the ground layer as well as the depth of the snow before averaging, which has been shown to be possible with the UWiBaSS system as the ground layer is easily distinguishable in the radar images. Also note that there is many more layer transitions in the stratigraphy in Figure 10.2b compared to Figure 9.2.

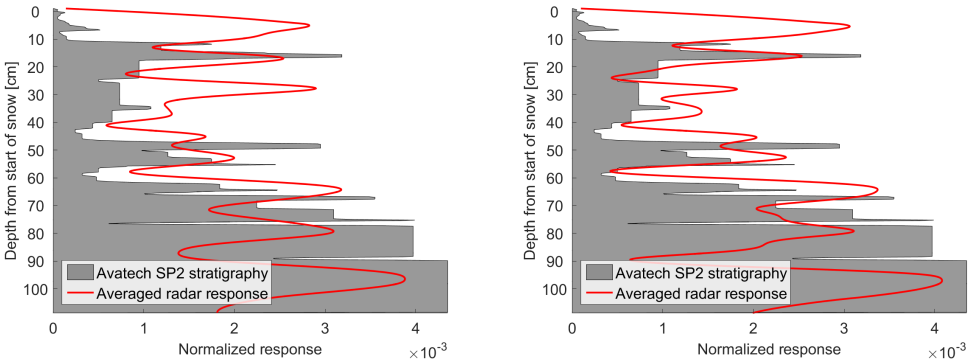

Figure 10.2: Averaged radar image correlated with *in situ* stratigraphy, where (a) is the entire transect and (b) is the first 50 cm.

10.2 Radar System Comparison

The radar image produced by the Novelda radar proved much more difficult to process as the image contained a severe amount of noise and ringing. Canny edge detection was used to add contrast to layers in addition to the same methods used on the UWiBaSS image.

As seen in Figure 10.3, the overall look of the image is much more noisy even after extensive processing. Severe ringing occurred at each layer transition, however after SVD, some of the ringing was removed. The detected transitions from the average of the entire image in Figure 10.4 correlate well with the *in situ* measurements with a correlation coefficient of 0.81 ± 0.27 and RMS error of 3.2 cm. However, in Figure 10.6, the penetration abilities of the Novelda system become apparent as no transitions are detected below 55 cm.

It is also apparent in Figure 10.3 that the ground layer is not particularly visible. This might be a major drawback as we will need to be able to scan even deeper snowpacks from even larger heights.

Looking at figures 9.2 and 10.4, there is a definitive similarity between the measurements of the different radar systems. As seen in Figure 10.5 the two radar systems correlate moderately yielding a correlation coefficient of 0.53 ± 0.16. This serve as a measurement validation since the two radar systems are different in almost every way (e.g. Transceiving principle, antenna, bandwidth etc.).

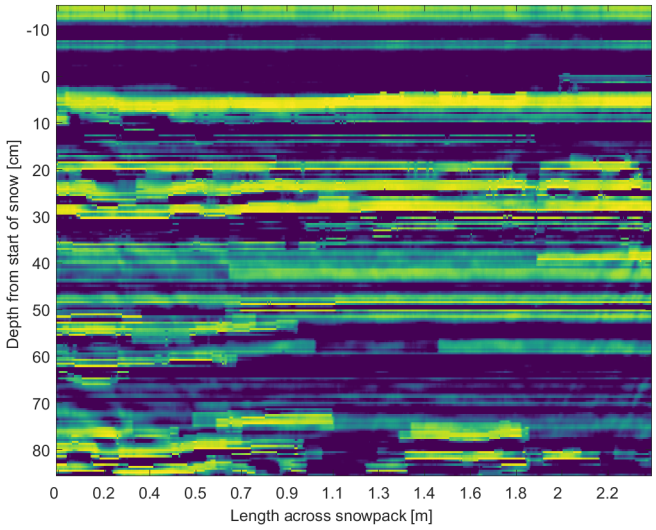

Figure 10.3: Processed Novelda radar image, with ground layer at approximately 75 cm.

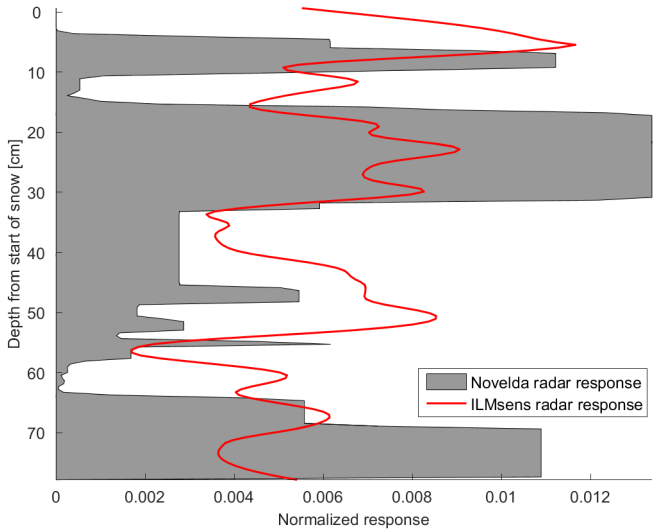

Figure 10.4: Snow stratigraphy comparison between *in situ* measurements performed with the Avatech SP2 snow probe and the averaged radar response of the same snowpack measured with the Novelda system. 11.03.16.

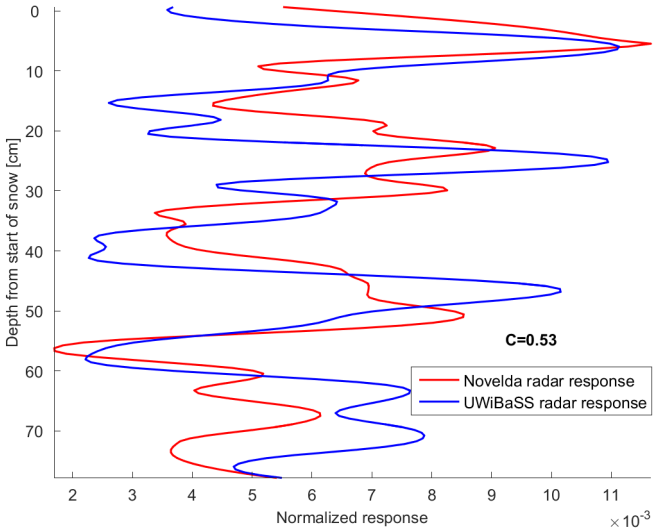

Figure 10.5: Correlation between Novelda and UWiBaSS radar.

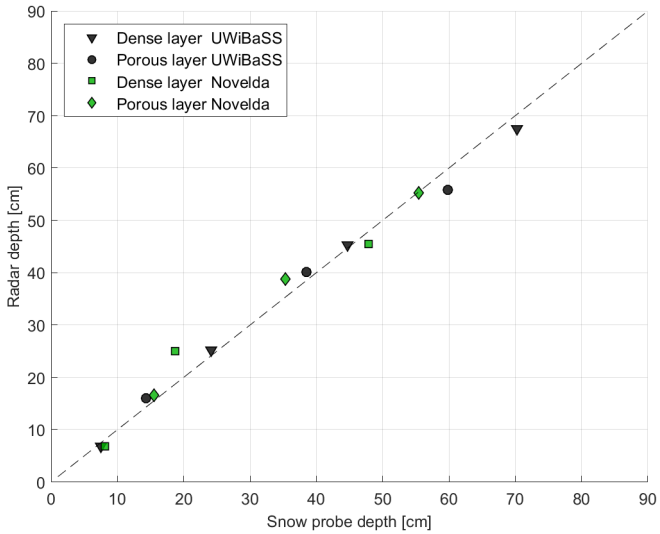

Figure 10.6: Comparison between the detected transitions with Novelda and UWiBaSS systems from 11.03.16. The Novelda system yielded *in situ* correlation of 0.81 ± 0.27 and RMS error of 3.2 cm, but no detection after approximately 55 cm.

10.3 Target Detection with SVD

The eigen image filtering method with SVD can also be used to remove clutter around targets. We can imagine that we are to detect the PEC plate on top of the snowpack. Albeit a very easy task, it works as a starting point for this method. Note that this is not necessarily interesting regarding the scope of this thesis, but in future work, it would be interesting to look at possibilities for detecting buried objects or even buried people. In our case, the only target to test the method on is the PEC plate mentioned earlier. This "target" is already clearly visible even in the unprocessed images, but it could serve as a test to see if we can use SVD to refocus the target.

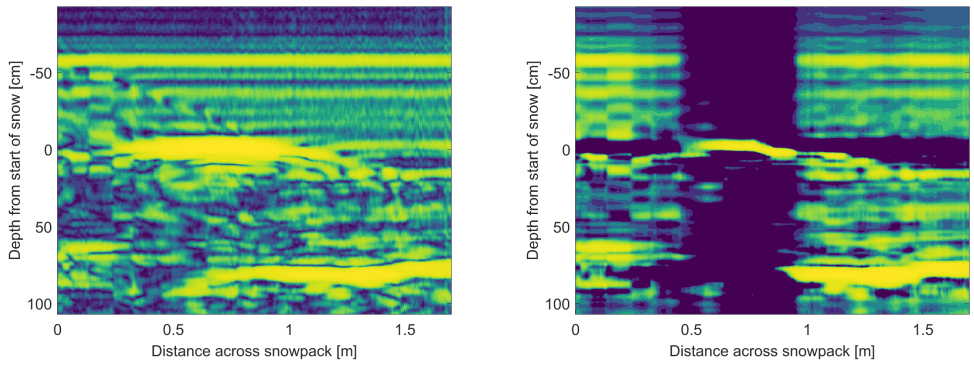

(a) (b)

Figure 10.7: Example target detection. (a) Before SVD processing. (b) After SVD processing.

From Figure 10.7a it is evident that the prominent PEC plate becomes even more visible after SVD filtering. This would be interesting to test on less visible targets. However, target detection was not prioritized during the measurement campaign and therefore no realistic buried target detection data were generated. In future projects, this would be interesting to investigate further.

10.4 Alternative Method of Radar Image Enhancement

The presented radar images have intentionally a minimal amount of filtering. During the work on this thesis, several methods of image enhancement were tested with different results. An alternative to histogram equalization is histogram specification, where in this case we try to force a separated pixel intensity distribution. Additionally, more filtering might make the main artifacts in the image clearer. The image in Figure 10.8 have been convolved with a mean filter kernel specially designed to favor horizontal lines.

The horizontal filter kernel $\mathbf{K}$ can be expressed as:

$$\mathbf{K} = \begin{bmatrix} 0 & 0 & 0 \\ \frac{1}{3} & \frac{1}{3} & \frac{1}{3} \\ 0 & 0 & 0 \end{bmatrix} . \tag{10.1}$$

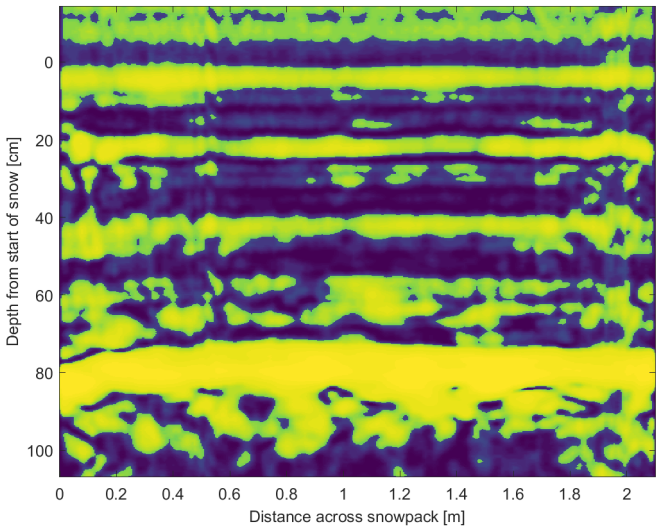

Figure 10.8: Alternative processing method of the radar image from 11.03.16 (e.g. Figure 8.3b) using histogram specification and a mean kernel specially designed to favor horizontal lines.

This method does improve the contrast of the main artifacts in the image, but small variations become less visible.

10.5 Wet Snow Measurements

Another important factor when scanning snow with radars is the liquid water content as discussed in section 4.2.6. In addition to the increased attenuation caused by the liquid water content, it is expected to observe increased scattering effects from icy, granular snow ([90, 91]) typical during the melting season. This will further reduce the power of the returned signal and decrease the visibility of the ground layer.

The snowpack was scanned one last time during the melting season with the intent of observing these effects compared to the scan of dry snowpacks. The snowpack had at this point melted considerably and had no detectable layer structure using the snow probe or even with manual inspection. The layer structure of the snowpack was in this case not interesting anyway since the objective of this scan was to observe the difference in attenuation between dry and wet snow.

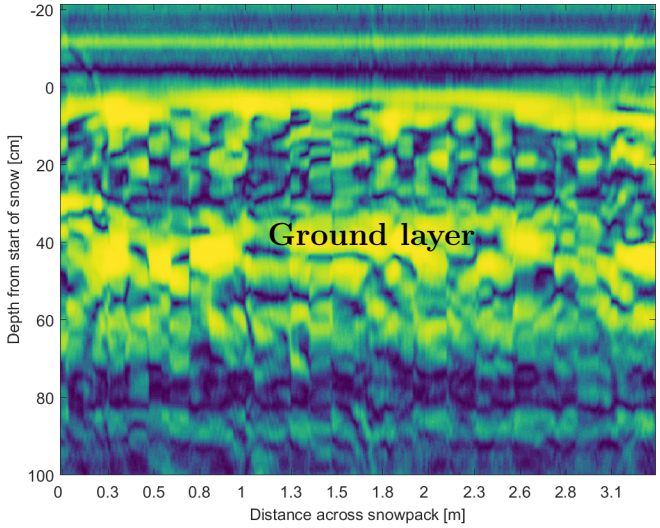

Figure 10.9: Processed response of snowpack with UWiBaSS radar 29.03.16.

As seen in Figure 10.9, the ground layer is less visible than the measurements performed on dry snow. Considering that the snowpack is approximately 35 cm compared to the 75 cm snowpacks previously investigated, it becomes apparent that we have significantly higher attenuation.

The liquid water content of this snowpack was measured to be 0.035 per unit volume. That is a significant amount of water, thus we need to use equation (4.9) to calculate the relative pulse velocity through the snow. With a measured density of 0.47 g/cm^3, equation (4.9) yield a relative permittivity of

2.34, which is significantly higher than for the dry snowpacks (average measured relative permittivity of dry snow ≈ 1.4). Relative permittivity affects both pulse propagation velocity and attenuation, effectively decreasing the detection range of the radar with increased losses and shorter unambiguous range due to the low pulse propagation velocity.

10.6 Altimetric Comparison

In the spring of 2016 (20.05.16) we conducted an octocopter UAV flight test with the UWiBaSS system. This was mainly to test the system while airborne to see how it performed with the added vibration of the octocopter. The test consisted of measuring the altitude with the UWiBaSS system and correlating it with other altimetric sensors. The UAV was to fly at different altitudes above ground while logging its altitude with both a barometric sensor as well as collecting altitude information from the GPS system. Meanwhile, the attached radar scanned the ground which in turn also provided a measurement of altitude. The test was conducted at a flat marshland where the UAV flew back and forth in the same line at different altitudes. This particular area was selected because the water content of the marshlands wet soil gives a stronger radar reflection than dry soil.

The UWiBaSS radar was fitted with voltage converters to be able to run on battery power and was mounted below an Octocopter named "Kraken", that was borrowed from Norut (Northern Research Institute). The vibration was one key concern regarding new noise introductions to the system. Therefore, a specially made mounting bracket was constructed to ensure minimal mechanical coupling between the UAV frame and the radar with rubber dampening on all contact points.

(a) (b)

Figure 10.10: Kraken Octocopter with UWiBaSS radar mounted below. Grounded in marshlands (a) and during flight (b).

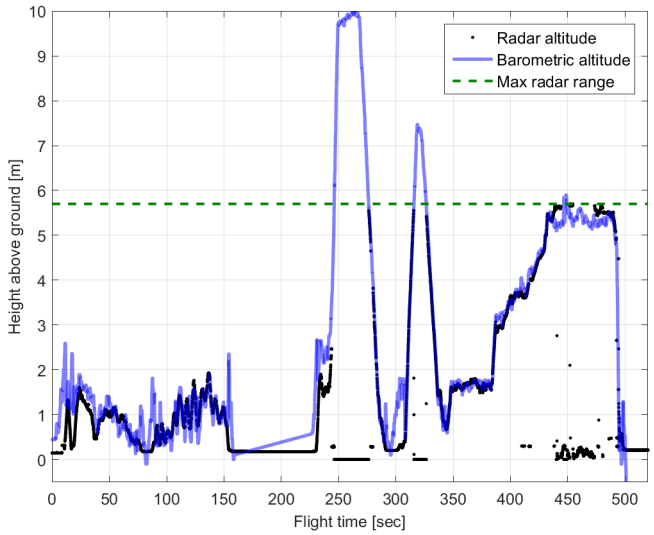

Figure 10.11: Altimetric comparison of radar pulses (black) and barometric sensor (blue).

The received radar data was processed the same way as for the snow measurements. Additionally, a peak detection algorithm was used (same as for snow transition detection in chapter 9) to find the first peak above a set threshold in the radar signal which in this case would be the ground. The resulting image gave a acceptable measurement of the altitude with clear similarities to the altimetric sensor already on board the UAV (Figure 10.11). However, as expected, the radar system had altitude limitations measured

to approximately 5.7 m, not far from the unambiguous range of the radar system which is 5.9 m in air (see table 5.2).

Notice in Figure 10.11 that the radar altitude show 0 m at high altitudes with a small amount of what appears to be noise (240-270 sec. and 420-490 sec). This effect is ghost reflections returning to the RX antenna after a given acquisition period has ended, thus, appearing in the next period as much closer to the antennas (actually, closer by the length of the unambiguous range). By shifting all pulses that are collected while flying above the unambiguous range an offset the length of the unambiguous range, an effectively longer range is obtained. Now we use the barometric altitude as a ground truth to our actual height and give all pulses above a set barometric height an offset.

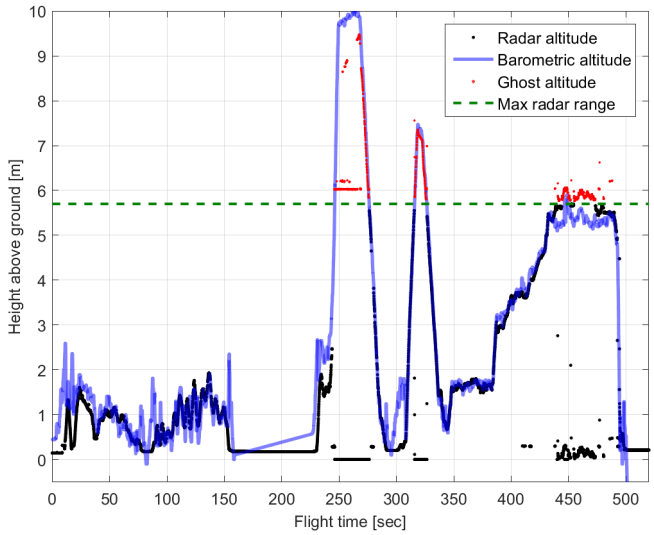

Figure 10.12: Altimetric comparison of radar pulses (black), ghost reflections (red) and barometric sensor (blue).

Figure 10.12 shows that the ghost reflections actually correlate well with the barometric altitude above the unambiguous range, with a small offset towards the end.

Part IV

Chapter 11

Discussion

In this chapter we will discuss the results from each section in Part III. This thesis contains several results to be discussed in this chapter. However, the key challenge in this thesis was to investigate the possibility to noninvasively measure snow stratigraphy with UWB radar and in that regard, chapter 9 which correlate the *in situ* measurements is the most central part.

Correlation with *In Situ* Measurements

One might require previous experience with snowpack assessment to classify porous layers and avalanche risk in the presented radar images. However, even an inexperienced reader will still be able to easily distinguish the most prominent layers in the snowpack.

In Figure 9.2, the layers detected by the radar and snow probe seem to correlate well. Going deeper down the snowpack, the main features are still similar, but with some offset in depth. The radar scans appeared to be slightly "shrunk" together compared with the *in situ* stratigraphy. This could be due to inaccuracies in the *in situ* measurements. The density measurements performed with the snow fork was used to calculate the pulse propagation velocity of the radar signal through the snowpack. Deviations in this calculation will "stretch" or "shrink" the signal extent and cause measurement errors. It could also be caused by depth measurement errors from the Avatech SP2 probe. The depth measurements performed by the Avatech SP2 probe were controlled with manual folding rule depth measurements and a 5 cm deviation between the probe and folding rule was found in the measurements from 11.03.16. The resulting stratigraphy from the Avatech SP2 probe was, therefore, adjusted to fit the correct depth of the snowpack. This error could be due to the penetration ability of the probe reaching deeper than both the radar and manual measurements. However, since we have no information about where in the snowpack the error occurred, the Avatech

SP2 stratigraphy was interpolated to fit the correct depth. It should be noted that this error did not affect the results significantly.

The largest deviation between detected layers by the radar and *in situ* measurements was approximately 6 cm, which should not affect the estimated avalanche risk considerably. However, the measurements performed at 24.02.16 resulted in a stratigraphy with very many layers close together. This type of snowpack might be difficult to analyze since each layer transition is spaced close together. In such cases, it might be more useful to visually inspect the result, or perhaps use smoothing filters to visualize the general shape of the stratigraphy. The *in situ* correlation in table 9.1 show an average RMS error of 2.48 cm, and a high linear correlation (0.97) between the most prominent layer transitions. A larger dataset containing measurements on several more snowpacks would contribute to the significance of these results. However, each snowpack measurement takes a full day's work to perform when considering the time it takes to set up the platform and perform the *in situ* measurements. A large scale UAV-mounted measurement along a mountainside with snow profiles taken at e.g. 10 m intervals along a 100 m transect would provide much more data to correlate.

Processing Methods

The processing method that improved the radar image the most was histogram equalization (section 8.1). This is partly due to the radar system not utilizing its full dynamic range and therefore distributed the radar signal over only a few pixel intensities.

In all radar scans taken from the constructed platform we saw a strong reflection about 50 cm above the PEC plate (see Figure 8.2). This is the reflection from the ladder that the radar system was rolling on. This reflection was not expected as the angle from the antenna to the ladder was approximately 180° (20° past HPBW of the antennas). This shows that strong reflectors (e.g. aluminum) should not be situated anywhere near even the side-lobes of the antennas.

Using eigen image filtering by SVD (section 8.2) some interference can be removed from the image. It might not be a huge improvement regarding the presented results (see Figure 8.3), however, when mounted on a UAV it is suspected that such vibrational interference might affect the image considerably. This method must be chosen based on application and will need fine-tuning of set parameters to work as desired.

The Hough transform (section 8.3) might prove useful to extract layer information without visual inspection of the radar image. For instance, one might design a system that outputs the depth location of all layer transitions

(dense-porous and porous-dense) with some additional parameter for each transition indicating the transition type based on the amplitude of the radar signal.

Radar Comparison

The comparison between the Novelda (with Vivaldi antennas) and UWiBaSS systems was mainly a test to compare the two systems in terms of depth penetration and resolution. After post processing, apparent similarities between the stratigraphies from the two compared radar systems emerged. This further implies that there is a deviation between the *in situ* and radar measurements. This could be due to measurement errors in the *in situ* instruments or might be caused by the unknown relationship between mechanical and dielectric properties of snow.

Due to the low output power compared to the UWiBaSS radar, the ground layer was hard to detect even after a low noise RF amplifier was mounted at the receiving end of the Novelda radar. Considering the fact that this snowpack was approximately 75 cm deep, does not show promise for scanning deeper snowpacks. However, we did get a good indication that the same layers were detected down to approximately 55 cm.

To conclude the radar system comparison, it is evident that the UWiBaSS system performs better. This is partly due to the larger radiated power that illuminates the layer transitions and soil with significantly more power than the Novelda radar. This will be important when using the radar system at higher altitude in a UAV and when scanning deeper snowpacks. The next version of the UWiBaSS system will additionally have a factor of 10 in increased output power.

Wet Snow Measurements

Liquid water content increases the relative permittivity of snow and thus will cause more scattering and propagation loss. This makes snow scanning difficult as the radar signal will have more loss while propagating through the snowpack.

It appears to be some artifacts in Figure 10.9 that resemble lumps of high-density snow or collections of liquid water. This effect was not expected and therefore not investigated *in situ*. This artifact could be used in radar-based snow type classification without *in situ* measurements if it proves to be typical for melting snow.

The measurement was performed on a shallow snowpack of only 35 cm. Even so, it is evident that the response from the ground is much lower than

with the dry snowpack. Additionally, we seem to get a special scattered response from inside the snowpack. This could be used later on to identify and classify layers if proved to be somewhat unique for this snow type.

Migration methods

The observant reader might have noticed that migration techniques have only been tested on synthetic data in Part I. This is because the implemented migration algorithms made no significant improvement to the radar images. This was due to a more complex target than a simple point scatterer as in the synthetic case. The targets in snow stratigraphy scanning are layered horizontal lines with little diffraction effects. However, this technique is still mentioned as it will probably be further developed to focus other targets (e.g. rocks on the ground, buried people) in the radar image. If we had more time at our disposal, more work would be put in implementing the Fast Factorized Back-Projection (FFD) algorithm as it is capable of handling large deviations from a linear flight track and give a reduction in processing time of two to three orders of magnitude [92]. However, this algorithm will show its advantages when we have large datasets from airborne snow scans, and not from small transects with highly linear movement.

UAV Mounted radar

The first experiments with mounting the UWiBaSS system to a UAV were successful. The range limitations of the system proved to be approximately 5.7 m. However, the utilization of ghost reflections increased the range considerably (at least 9.5 m) when assigned the simple task of measuring altitude with a radar. The "ghost range" is beyond the specified range from the radar sensor manufacturer (5.9 m), which is quite interesting, but it is not especially useful for snow scanning purposes as the ghost reflections will be very difficult to utilize when scanning a multi-layer target (i.e. Snow).

The on-board altimetric sensor can function as an altitude reference to the radar when snow scanning is performed. However, more accurate sensors (e.g. laser rangefinders) should be used to ensure accurate measurements of the top snow layer. The UAV was grounded for about 1.5 minutes during the flight test (Figure 10.10 from 150 to 240 sec.). The barometric sensor output drifted approximately 0.5 m during that period which seemed to cause an offset to the height measurement for about 1 minute until it returned to the same recorded height as the radar. Hence, a more accurate altimetric sensor might be needed.

How the UAV is to be maneuvered during data acquisition is still a topic open for discussion. Further experimentation to find the maximum scanning

speed is needed to be able to suggest a flight plan. The current suggestion is to fly to selected areas in the mountainside and perform low altitude, slow scans over short distances (e.g. 5-50 m). This can be performed on several selected sites along the mountain instead of a scan across the full length of the mountain. This is to shorten the flight time (i.e. battery usage) so that the UAV can cover as much area as possible in one flight.

Another possible challenge is the possibility of jamming the on-board GPS. Small fractions of the radiated signal could enter the GPS antenna. However, the metal frame of the UAV does provide some degree of shielding. The shielding could easily be improved if jamming causes problems in the future.

During our tests, the GPS system had no indication of corrupted data, but it should be investigated further if the radar will cause any jamming for the on-board GPS, especially after mounting the new antennas presented in section 12.1.

To summarize, the system performed as expected regarding the height measurement. Some expected additional noise were present, but this can possibly be improved with better vibration dampening.

Chapter 12

Conclusions

In this thesis we have investigated the possibility to use UWB radars to non-invasively determine the layer distribution (stratigraphy) in snowpacks, and the prospect of performing these measurements for an UAV. The correlation between the UWiBaSS system and *in situ* measurements in chapter 9 resulted in an average RMS error of 2.48 cm, and a high linear correlation (0.97). Thus, based on the results presented, we can conclude that it is possible to measure snow stratigraphy with m:sequence UWB radars. The task of obtaining dependable snow stratigraphies from an UAV mounted radar system is plausible, but further testing on snow and modeling is needed to gain reliable non-invasive measurements.

Regarding the comparison between the Novelda and UWiBaSS systems, it is evident that the UWiBaSS system performed best for the task of UAV snow stratigraphy measurements due to higher radiated power which illuminated all layer transitions all the way down to the soil. This radiated power will be needed when the altitude above the snow increases in UAV flight operations. This thesis also shows that penetration depth is significantly reduced when the snow contains liquid water. However, most avalanche related fatalities occur with dry snow slabs [2], which is the snow types this proposed system is most likely to perform best at.

12.1 Future Work

The UWiBaSS system is currently under further development. Instead of the Archimedean spiral antenna at the RX port, we now utilize both RX ports of the ILMsens sensor with a specially developed Vivaldi antenna at each port. This allows the radar to receive composite polarization from the transmitted circularly polarized signal as we still use the spiral antenna as TX. Additionally, the increased directivity of these antennas will hopefully

increase the range of the radar when used in combination with a sensor with a longer PRBS registry, which ILMsens currently have available. A longer registry will result in a longer measurement time if the clock frequency and control PC is the same. Therefore a detailed study of minimum measurement rate for UAV flight is needed.

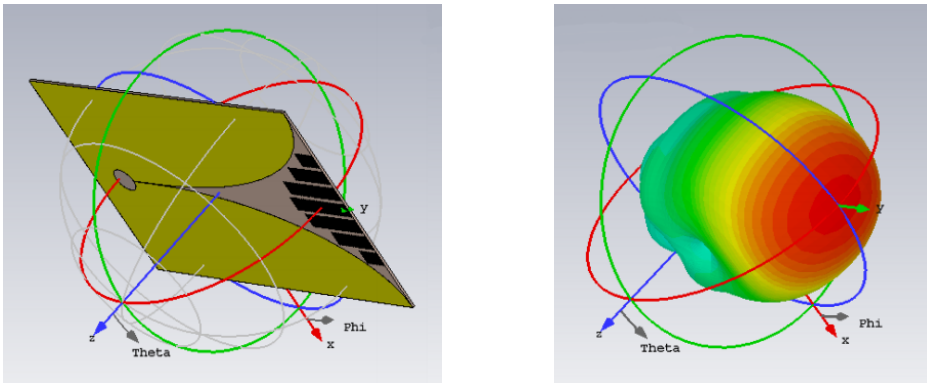

(a) (b)

Figure 12.1: 3D model (a) and radiation pattern (b) of the new Vivaldi antenna with lens elements in front of antenna.

During measurements with the UWiBaSS system we noticed that the dynamic range of the sensor was not completely utilized. The ILMsens sensor have a 14 bit ADC capable of high resolution in the dynamic range, but only a small portion of the input range was utilized due to the low dynamics of the signal at the RX stage. In the UWiBaSS mk2 system we, therefore, use a RF power amplifier at the TX stage which should give more dynamics to the returned signals. This will reduce quantization error during sampling because samples will be distributed broader across the input range of the sensor. In Øyan et al. [27], range gates is used to improve the dynamic range of a SFCW radar. The range gate effectively removes antenna crosstalk which normally is the strongest signal. This enables the system to transmit more power which would without gating saturate the ADC at the receiver end, thus improving the dynamic range of the radar. Range gates could possibly be implemented on m:sequence radar systems as well and might improve the dynamic range. However, extensive modification to the transmitting scheme of the radar is needed and will probably reduce the measurement rate.

The maximal scanning speed of the UWiBaSS system is yet to be found. Experimentation with different speeds while scanning from the measurement platform was performed during the measurement campaign to give some estimation of the maximal speed one could have while still acquiring a non-blurred image. However, the highest speed tested was approximately 0.02

m/s, which did not compromise the image significantly. Higher speeds were not tested on the measurement platform as it was difficult to maintain a constant speed. This can be solved by mounting stepper motors on the dolly to improve the speed and position control.

The UWiBaSS MKII system is to be mounted in an octocopter UAV and flown over large snow areas. The data from this test would be interesting to analyze to see the snow scanning performance at higher altitude.

To facilitate for measurements in alpine areas a solution to angle the antennas perpendicular to the snow is needed. This can be done by using several laser rangefinders to measure the distance to the snowpack at different angles and position the antennas towards the shortest distance. Hence, the antennas need to be mounted on a gimbal to allow adjustment of its relative angle to the snowpack.

The top powder layer of snow is hard to detect with the mentioned radar systems. Therefore, the start of the snowpack needs to be accurately measured to enable accurate layer detection within the snowpack. This can be performed with laser or ultrasound rangefinders.

To increase measurement accuracy when performing non-invasive UAV scans of the snowpack, different models for relative pulse velocity could be created for different types of snow. This will enable calculation of relative pulse velocity without the need for *in situ* measurements. To create these models, a quantitative study of snow parameters is needed, and from this, a generalization of different classes of snow could be found.

A different usage for this system is in the search for buried targets (e.g. buried people [15]). For this task, migration techniques and SVD eigen image filtering might prove useful.

Appendix A

Matlab Scripts Download Link

The interested reader can take a look at a selection of the scripts and functions that were written and used in this thesis (link below). Most scripts initialize by loading a data file containing radar data or other sensor data (e.g. *in situ* measurements), which is not included in the .zip file due to the sheer size of the collected data (more than 10 GB). Hence, the scripts are not directly executable, but can provide the reader with information about how the different processing techniques were implemented.

Click **here** or use the url below:
mathworks.com/matlabcentral/fileexchange/60637-selected-scripts

Bibliography

[1] M. Lutschg. "Characteristics of human-triggered avalanches" (2001), pp. 147–162. DOI: 10.1016/S0165-232X(01)00037-4.

[2] J. B. Jamieson and C. D. Johnston. "Snowpack characteristics associated with avalanche accidents". *Canadian Geotechnical Journal* 29.5 (1992), pp. 862–866. DOI: 10.1139/t92-093.

[3] H. Smith. "Snow Pit Procedures". *NASA* (2007).

[4] C. Pielmeier and M. Schneebeli. "Snow stratigraphy measured by snow hardness and compared to surface section images". *Proceedings of the International Snow Science Workshop* (2002), pp. 1–8.

[5] B. Sovilla and P. Bartelt. "Observations and modelling of snow avalanche entrainment". *Natural Hazards and Earth System Sciences* 2.3-4 (2002), pp. 169–179. DOI: 10.5194/nhess-2-169-2002.

[6] M. Sturm, J. Johnson, and J. Holmgren. "Variations in the mechanical properties of arctic and subarctic snow at local (1-m) to regional (100-km) scales". *Science* (2004), pp. 1–20.

[7] J. Schweizer. "On recent advances in applied snow and avalanche research". *Cold Regions Science and Technology* 97 (2014), pp. 57–59. DOI: 10.1016/j.coldregions.2013.10.005.

[8] Swiss Council for Accident Prevention. *Avalanche danger, how to better assess the risks*. 2010. URL: http://www.slf.ch/dienstleistungen/merkblaetter/bfu_avalanche_danger.pdf.

[9] F. Cappabianca, M. Barbolini, and L. Natale. "Snow avalanche risk assessment and mapping: A new method based on a combination of statistical analysis, avalanche dynamics simulation and empirically-based vulnerability relations integrated in a GIS platform". *Cold Regions Science and Technology* 54.3 (2008), pp. 193–205. DOI: 10.1016/j.coldregions.2008.06.005.

[10] Canadian Avalanche Association. *Guidelines for snow avalanche risk determination and mapping in Canada*. 2002. ISBN: 0-9685856-4-7.

[11] H. Hertz. *Electric Waves: Being Researches on the Propagation of Electric Action with Finite Velocity Through Space*. 1893. URL: http://n3ox.net/files/hertz_Electric_waves.pdf.

[12] J. Clerk Maxwell. "A Dynamical Theory of the Electromagnetic Field". *Philosophical Transactions of the Royal Society of London* 155.January (1865), pp. 459–512. DOI: 10.1098/rstl.1865.0008.

[13] J. D. Taylor. *Ultrawideband Radar Applications and Design*. CRC Press, 2012. ISBN: 9781420089868.

[14] N. Yankielun, W. Rosenthal, and R. E. Davis. "Alpine snow depth measurements from aerial FMCW radar". *Cold Regions Science and Technology* 40.1-2 (2004), pp. 123–134. DOI: 10.1016/j.coldregions.2004.06.005.

[15] E. Zaikov, J. Sachs, M. Aftanas, and J. Rovnakova. "Detection of trapped people by UWB radar". *German Microwave Conference*. Mar. 2008, pp. 1–4.

[16] H. P. Marshall, M. Schneebeli, and G. Koh. "Snow stratigraphy measurements with high-frequency FMCW radar: Comparison with snow micro-penetrometer". *Cold Regions Science and Technology* 47.1-2 SPEC. ISS. (2007), pp. 108–117. DOI: 10.1016/j.coldregions.2006.08.008.

[17] T. Geldsetzer and B. Jamieson. "Estimating dry snow density from grain form and hand hardness". *International Snow Science Workshop* January (2000), pp. 121–127.

[18] C. Pielmeier and M. Schneebeli. "Developments in the stratigraphy of snow". *Surveys in Geophysics* 24.5-6 (2003), pp. 389–416. DOI: 10.1023/B:GEOP.0000006073.25155.b0.

[19] H. Gubler and M. Hiller. "The use of Microwave FMCW Radar in Snow and Avalanche Research". 9 (1984), pp. 109–119.

[20] J. Holmgren, M. Sturm, N. E. Yankielun, and G. Koh. "Extensive measurements of snow depth using FM-CW radar". *Cold Regions Science and Technology* 27.1 (1998), pp. 17–30. DOI: 10.1016/S0165-232X(97)00020-7.

[21] D. Ellerbrugh and H. Boyne. "Snow Stratigraphy and Water Equivalence". *Journal of Glaciology* 26.94 (1980), pp. 225–233.

[22] K. Sand and B. Bruland. "Application of Georadar for Snow Cover Surveying". *Hydrology Research* 29 (1998), pp. 361–370.

[23] J. B. A. Lundberg, H. Thunehed. "Impulse Radar Snow Surveys – Influence of Snow Density". *Hydrology Research* 31 (2000), pp. 1–14.

[24] H. P. Marshall and G. Koh. "FMCW radars for snow research". *Cold Regions Science and Technology* 52.2 (2008), pp. 118–131. DOI: 10.1016/j.coldregions.2007.04.008.

[25] P. Kanagaratnam, T. Markus, V. Lytie, B. Heavey, P. Jansen, G. Prescott, and S. P. Gogineni. "Ultrawideband radar measurements of thickness of snow over sea ice". *IEEE Transactions on Geoscience and Remote Sensing* 45.9 (2007), pp. 2715–2724. DOI: 10.1109/TGRS.2007.900673.

[26] N. Rutter, H.-P. Marshall, K. Tape, R. Essery, and J. King. "Impact of spatial averaging on radar reflectivity at internal snowpack layer boundaries". *Journal of Glaciology* (2016), pp. 1–10. ISSN: 0022-1430. DOI: 10.1017/jog.2016.99.

[27] M. J. Øyan, S. E. Hamran, L. Hanssen, T. Berger, and D. Plettemeier. "Ultrawideband gated step frequency ground-penetrating radar". *IEEE Transactions on Geoscience and Remote Sensing* 50.1 (2012), pp. 212–220. DOI: 10.1109/TGRS.2011.2160069.

[28] S. Gogineni, J. B. Yan, D. Gomez, F. Rodriguez-Morales, J. Paden, and C. Leuschen. "Ultra-wideband radars for remote sensing of snow and ice". *2013 IEEE MTT-S International Microwave and RF Conference, IMaRC 2013* (2013), pp. 1–4. DOI: 10.1109/IMaRC.2013.6777743.

[29] R. Kwok, B. Panzer, C. Leuschen, S. Pang, T. Markus, B. Holt, and S. Gogineni. "Airborne surveys of snow depth over Arctic sea ice". *Journal of Geophysical Research: Oceans* 116.11 (2011), pp. 1–16. DOI: 10.1029/2011JC007371.

[30] B. Panzer, D. Gomez-Garcia, C. Leuschen, J. Paden, F. Rodriguez-Morales, A. Patel, T. Markus, B. Holt, and P. Gogineni. "An ultra-wideband, microwave radar for measuring snow thickness on sea ice and mapping near-surface internal layers in polar firn". *Journal of Glaciology* 59.214 (2013), pp. 244–254. DOI: 10.3189/2013JoG12J128.

[31] A. N. Arslan, J. Pulliainen, J. Lemmetyinen, T. Nagler, H. Rott, and M. Kern. "Effects of snowpack parameters and layering processes at X- and Ku-band backscatter". *International Geoscience and Remote Sensing Symposium (IGARSS)* (2011), pp. 3637–3640. DOI: 10.1109/IGARSS.2011.6050012.

[32] K. Eder, C. Reidler, C. Mayer, and M. Leopold. "Crevasse detection in alpine areas using ground penetrating radar as a component for a mountain guide system" (2004), pp. 837–842.

[33] K. K. Singh, P. Datt, V. Sharma, A. Ganju, V. D. Mishra, A. Parashar, and R. Chauhan. "Snow depth and snow layer interface estimation using Ground Penetrating Radar". *Current Science* 100.10 (2011), pp. 1532–1539.

[34] R. Azadegan, K. Sarabandi, C. Science, and M. A. Arbor. "Analytical Formulation of the Scattering by a Slightly Rough Dielectric Boundary, Covered with a Homogenous Dielectric Layer". *Antennas and Propagation Society International Symposium* 1 (2003), pp. 420–423. DOI: 10.1109/APS.2003.1219876.

[35] R. O. R. Jenssen, M. Eckerstorfer, H. Vickers, K.-A. Høgda, E. Malnes, and S. K. Jacobsen. "Drone-based UWB radar to measure snow layering in avalanche starting zones". *International Snow Science Workshop*. October. 2016.

[36] IEEE Standards Association. *IEEE Standard Definitions of Terms for Antennas*. Vol. 2013. 2014, pp. 1–50. DOI: 10.1109/IEEESTD.2014.6758443.

[37] D. Pozar. *Microwave Engineering*. Wiley, 2012, pp. 469–519. ISBN: 978-0-470-63155-3.

[38] D. Daniels. *Ground Penetrating Radar*. Vol. 1. Institution of Engineering and Technology, 2013, pp. 225–237. ISBN: 978-0863413605.

[39] V. C. Chen, F. Li, S. S. Ho, and H. Wechsler. "Micro-doppler effect in radar: Phenomenon, model, and simulation study". *IEEE Transactions on Aerospace and Electronic Systems* 42.1 (2006), pp. 2–21. DOI: 10.1109/TAES.2006.1603402.

[40] M. Aftanas. "Through Wall Imaging Using M-sequence UWB Radar System". *Dessertion* December (2007).

[41] M. Tiuri, A. Sihvola, E. Nyfors, and M. Hallikaiken. "The complex dielectric constant of snow at microwave frequencies". *IEEE Journal of Oceanic Engineering* 9.5 (1984), pp. 377–382. DOI: 10.1109/JOE.1984.1145645.

[42] M. Wahab, Y. P. Saputera, and Y. Wahyu. "Design and realization of archimedes spiral antenna for Radar detector at 2-18 GHz frequencies". *2013 19th Asia-Pacific Conference on Communications, APCC 2013*. 2013, pp. 304–309. DOI: 10.1109/APCC.2013.6765961.

[43] A. Sihvola and M. Tiuri. "Snow Fork for Field Determination of the Density and Wetness Profiles of a Snow Pack". *IEEE Transactions on Geoscience and Remote Sensing* GE-24.5 (1986), pp. 717–721. DOI: 10.1109/TGRS.1986.289619.

[44] W. H. Stiles and F. T. Ulaby. "Dielectric Properties of Snow". *The Avalanche Book* (1986), pp. 49–71.

[45] C. Mätzler, A. Wiesmann, J. Pulliainen, and M. Hallikainen. "Microwave Emission of Snow" (1999), pp. 1–17.

[46] F. Abujarad. "Ground Penetrating Radar signal processing for landmine detection". *Dissertation* (2007).

[47] F. Soldovieri and R. Solimene. "Ground Penetrating Radar Subsurface Imaging of Buried Objects". *Radar Technology*. December. 2010, pp. 105–126. DOI: 10.5772/7176.

[48] D. Borland and R. M. Taylor. "Rainbow Color Map (Still) Considered Harmful". *IEEE computer graphics and applications* 27.2.April (2007), pp. 14–17. DOI: 10.1109/MCG.2007.323435.

[49] T. W. Hertel and G. S. Smith. "On the dispersive properties of the conical spiral antenna and its use for pulsed radiation". *IEEE Transactions on Antennas and Propagation* 51.7 (2003), pp. 1426–1433. DOI: 10.1109/TAP.2003.813602.

[50] T. Strutz. *Data Fitting and Uncertainty: A practical introduction to weighted least squares and beyond*. 2011, p. 244. ISBN: 978-3-658-11455-8.

[51] L. J. Myers, M. Lowery, M. O'Malley, C. L. Vaughan, C. Heneghan, A. St. Clair Gibson, Y. X. R. Harley, and R. Sreenivasan. "Rectification and non-linear pre-processing of EMG signals for cortico-muscular analysis". *Journal of Neuroscience Methods* 124.2 (2003), pp. 157–165. DOI: 10.1016/S0165-0270(03)00004-9.

[52] B. Boashash. "Estimating and interpreting the instantaneous frequency of a signal. I. Fundamentals". *Proceedings of the IEEE* 80.4 (1992), pp. 520–538. DOI: 10.1109/5.135376.

[53] S. Lawrence Marple. *Computing the discrete-time analytic signal via fft*. 1999. DOI: 10.1109/78.782222.

[54] M. T. Hallikainen, F. T. Ulaby, and M. Abdelrazik. "Dielectric properties of snow in the 3 to 37 GHz range". *IEEE Transactions on Antennas and Propagation* AP-34.11 (1986), pp. 1329–1340. DOI: 10.1109/TAP.1986.1143757.

[55] R. C. Gonzalez and R. E. Woods. *Digital Image Processing*. 2010. ISBN: 978-0-13-234563-7.

[56] J. Lim. *Two Dimesional signal and image processing*. Prentice Hall PTR, 1990. ISBN: 0-13-935322-4.

[57] J.-H. Kim, S.-J. Cho, and M.-J. Yi. "Removal of ringing noise in GPR data by signal processing". *Geosciences Journal* 11.1 (2007), pp. 75–81. DOI: 10.1007/BF02910382.

[58] P. Waldemar and T. Ramstad. "Hybrid KLT-SVD image compression". *IEEE International Conference on Acoustics, Speech, and Signal Processing*. 1997. DOI: 10.1109/ICASSP.1997.595349.

[59] G. F. Margrave. "Numerical Methods of Exploration Seismology" (2003).

[60] P. Sguazzero and J. Gazdag. "Migration of seismic data". *Journal of Statistical Physics* 76.1-2 (1994), pp. 703–723. DOI: 10.1007/BF02188682.

[61] S. Jacobsen and Y. Birkelund. "Improved resolution and reduced clutter in ultra-wideband microwave imaging using cross-correlated back projection: Experimental and numerical results". *International Journal of Biomedical Imaging* 2010 (2010). DOI: 10.1155/2010/781095.

[62] Y. S. Yoon and M. G. Amin. "Spatial filtering for wall-clutter mitigation in through-the-wall radar imaging". *IEEE Transactions on Geoscience and Remote Sensing* 47.9 (2009), pp. 3192–3208. DOI: 10.1109/TGRS.2009.2019728.

[63] D. Garcia, L. L. Tarnec, S. Muth, E. Montagnon, J. Porée, and G. Cloutier. "Stolt ' s f - k Migration for Plane Wave Ultrasound Imaging". *IEEE Transactions on Ultrasonics, Ferroelectrics and Frequency Control* 60.9 (2013), pp. 1853–1867. DOI: 10.1109/TUFFC.2013.2771.

[64] A. Sayedelahl and R. P. Bording. "A Study of Seismic Inverse Methods for Radar Signal Processing". *34th Applied Imagery and Pattern Recognition Workshop (AIPR'05)* (2005), pp. 58–62. DOI: 10.1109/AIPR.2005.12.

[65] W. Lertniphonphun and J. H. Mcclellan. "Migration of Underground Targets in UWB-SAR Systems" (2000), pp. 713–716. DOI: 10.1109/ICIP.2000.901058.

[66] M. Aftanas, E. Zaikov, M. Drutarovský, and J. Sachs. "Through wall imaging of the objects scanned by m-sequence UWB radar system". *Proceedings of the 18th International Conference Radioelektronika 2008* (2008), pp. 2–5. DOI: 10.1109/RADIOELEK.2008.4542687.

[67] ILMsens. *ILMsens m:explore – datasheet*. URL: http://ilmsens.com/images/downloads/mexplore_datasheet_20160520.pdf.

[68] H. Stark and J. Woods. *Probability, Statistics and Random Processes for Engineers*. 2011. ISBN: 978-0-273-75228-8.

[69] P. Horowitz and W. Hill. *The Art of Electronics*. Cambridge, 2010, pp. 473–495. ISBN: 978-0-521-80926-9.

[70] J. Sachs, M. Kmec, H. Fritsch, M. C. Helbig, R. Herrmann, K. Schilling, and P. Rauschenbach. "Noise Radar Design" (2013).

[71] J. Sachs, R. Herrmann, M. Kmec, M. Helbig, and K. Schilling. "Recent Advances and Applications of M-Sequence based Ultra-Wideband Sensors" (2007). DOI: 10.1109/ICUWB.2007.4380914.

[72] J. Sachs, M. Gmbh, and T. U. Ilmenau. "M-Sequence Ultra-Wideband-Radar, State of Development and Applications" (2003). DOI: 10.1109/RADAR.2003.1278743.

[73] H. J. Ng, R. Feger, and A. Stelzer. "A fully-integrated 77-GHz UWB pseudo-random noise radar transceiver with a programmable sequence generator in SiGe technology". *IEEE Transactions on Circuits and Systems I: Regular Papers* 61.8 (2014), pp. 2444–2455. DOI: 10.1109/TCSI.2014.2309774.

[74] S. Jacobsen, H. O. Rolfsnes, and P. R. Stauffer. "Characteristics of microstrip muscle-loaded single-arm Archimedean spiral antennas as investigated by FDTD numerical computations". *IEEE Transactions on Biomedical Engineering* 52.2 (2005), pp. 321–330. DOI: 10.1109/TBME.2004.840502.

[75] J. S. Mosy. "Ultra wideband radar antenna design for snow measurement applications". *Master Thesis* (2009).

[76] R. C. Johnson. *Antenna engineering handbook*. 1993. ISBN: 0-07-032381-X.

[77] D. T. Wisland, S. Støa, N. Andersen, K. Granhaug, T. S. Lande, and H. A. Hjortland. "CMOS nanoscale impulse radar utilized in 2-dimensional ISAR imaging system". *IEEE National Radar Conference - Proceedings* (2012), pp. 0714–0719. DOI: 10.1109/RADAR.2012.6212231.

[78] H. A. Hjortland. "UWB impulse radar in 90 nm CMOS". *Master Thesis* (2006).

[79] M. Cavagnaro, S. Pisa, and E. Pittella. "Safety aspects of human exposure to ultra wideband radar fields". *International Symposium on Electromagnetic Compatibility - EMC EUROPE* (2012), pp. 1–5. DOI: 10.1109/EMCEurope.2012.6396885.

[80] M. Proksch, N. Rutter, C. Fierz, and M. Schneebeli. "Intercomparison of snow density measurements: Bias, precision, and vertical resolution". *Cryosphere* 10.1 (2016), pp. 371–384. DOI: 10.5194/tc-10-371-2016.

[81] A. Denoth, A. Foglar, P. Weiland, C. Maatzler, H. Aebischer, M. Tiuri, and A. Sihvola. "A comparative study of instruments for measuring the liquid water content of snow". *Journal of Applied Physics* 56.7 (1984), p. 2154. DOI: 10.1063/1.334215.

[82] A. Denoth and A. Foglar. "Recent developments of snow moisture dielectric devices". *International Snow Science Workshop* (1986), pp. 72–76.

[83] N. J. Kinar and J. W. Pomeroy. "Measurement of the physical properties of the snowpack". *Rev. Geophys* 53 (2015). DOI: 10.1002/2015RG000481.

[84] M. W. Williams. "Correlation Lengths of Meltwater Flowthrough Ripe Snowpacks". October 2001 (2016). DOI: 10.1002/(SICI)1099-1085(199909)13:12/13<1807::AID-HYP891>3.0.CO;2-U.

[85] F. Techel and C. Pielmeier. "Point observations of liquid water content in wet snow – Investigating methodical, spatial and temporal aspects". *Cryosphere* 5.2 (2011), pp. 405–418. DOI: 10.5194/tc-5-405-2011.

[86] F. Koch, M. Prasch, L. Schmid, J. Schweizer, and W. Mauser. "Measuring snow liquid water content with low-cost gps receivers". *Sensors (Switzerland)* 14.11 (2014), pp. 20975–20999. DOI: 10.3390/s141120975.

[87] A. Denoth. "An electronic device for long-term snow wetness recording". *Annals of Glaciology* 19 (1994), pp. 104–106. DOI: 10.3198/1994AoG19-1-104-106.

[88] E. R. Lutz and H.-P. Marshall. "Validation study of Avatech's rapid snow penetrometer, SP1". *International Snow Science Workshop* (2014), pp. 843–846.

[89] P. Hagenmuller, T. Pilloix, and Y. Lejeune. "Inter Comparison of Snow Penetrometers (RAMSONDE, AVATECH SP2 and SNOWMI-CROPEN) in the Framework of Avalanche Forecasting" (2016).

[90] Y. Kuga, F. T. Ulaby, T. F. Haddock, and R. D. DeRoo. "Millimeter wave radar scattering from snow: Part 1. Radiative transfer model". *Radio Science* 26.2 (1991), pp. 329–341. DOI: 10.1029/90RS02560.

[91] F. T. Ulaby, T. F. Haddock, R. T. Austin, and Y. Kuga. "Millimeter-wave radar scattering from snow: Part 2. Comparison of theory with experimental observations". *Radio Science* 26.2 (1991), pp. 343–351. DOI: 10.1029/90RS02559.

[92] L. M. H. Ulander, H. Hellsten, and G. Stenström. "Synthetic-Aperture Radar Processing using Fast Factorised Back-Projection". *IEEE Transactions on Aerospace and Electronic Systems* 39.3 (2000), pp. 1–32. DOI: 10.1109/TAES.2003.1238734.